이학박사 학위논문

Lateral and Vertical Electronic Transport Properties of Topological Insulator-Based van der Waals Heterostructures Grown by Molecular Beam Epitaxy

분자빔에피택시로 성장한 위상절연체 기반 반데르발스 이종구조에서의 수직 및 수평 방향 전자 수송 특성

2019년 8월

서울대학교 대학원

물리·천문학부

박 준 영

Ph.D. Dissertation

Lateral and Vertical Electronic Transport Properties of Topological Insulator-Based van der Waals Heterostructures Grown by Molecular Beam Epitaxy

by

Joon Young Park

August 2019

Graduate School of
Seoul National University
Department of Physics and Astronomy

Lateral and Vertical Electronic Transport Properties of Topological Insulator-Based van der Waals Heterostructures Grown by Molecular Beam Epitaxy

분자빔에피택시로 성장한 위상절연체 기반 반데르발스 이종구조에서의 수직 및 수평 방향 전자 수송 특성

지도교수 이 규 철

이 논문을 이학박사 학위논문으로 제출함

2019년 5월

서울대학교 대학원

물리·천문학부

박 준 영

박준영의 박사 학위논문을 인준함

2019년 5월

위 원 장 김 도 헌 (인)

부위원장 이 규 철 (인)

위 원 김 창 영 (인)

위 원 박 철 환 (인)

위 원 이 철 호 (인)

This work is entirely dedicated to my family and my wife Jaerang

for their unconditional love and support.

Abstract

Research on van der Waals (vdW) heterostructures has recently been boosted as a new class of material called topological insulator (TI) has joined the vdW material library. While there has been a huge amount of efforts to achieve novel topological heterostructures with low defect density and precise atomic controllability of the vdW interface, it is still necessary to develop a highly controlled and engineered materials growth approach and novel characterization and device fabrication techniques.

In this dissertation, I present the novel combination of molecular beam epitaxial (MBE) growth with vdW-layer manipulation technique, transmission electron microscopy (TEM) structural analysis, and nanodevice fabrication processes to prepare atomically engineered vdW heterostructures based on TIs of high-quality. With this approach, I particularly focus on lateral and vertical topological electronic transport across the high-quality vdW heteroepitaxial interfaces between TIs and hexagonal boron nitride (hBN).

First, I discuss MBE growth and structural/electrical properties of high-quality TI Bi_2Se_3 thin films on hBN. The TEM-compatibility enables the MBE to receive fast feedback on structural properties of the films, thus facilitating growth optimization. I demonstrate a growth method for enhancing the uniformity and crystallinity of the films on hBN. Through the

high-resolution TEM study, I show an atomically abrupt and epitaxial interface between Bi_2Se_3 and hBN. I investigate gate dependent magnetotransport properties of the heterostructure to demonstrate the formation of high mobility topological states at the Bi_2Se_3/hBN interface. In addition, I show that the growth and characterization scheme can be extended to various combinations of TI/vdW heterostructures.

The following part presents the fabrication and measurement of vertical vdW tunnel junctions where two epitaxially aligned TIs are separated by a-few-atom-thick hBN tunnel barriers. Here, the suspended, atomically thin hBN allows the materials growing on both sides to align heteroepitaxially and provides direct electrical access to the interfacial electronic states. Through magneto-tunneling spectroscopy on two kinds of vertical TI/hBN/TI epitaxial vdW heterostructures, I explore the properties of tunneling electrons in terms of energy, momentum, and spin helicity conservation.

Keywords: Molecular beam epitaxy, van der Waals heterostructure, Topological insulator, Hexagonal boron nitride, Electronic transport properties, Tunneling spectroscopy

Student Number: 2012-20363

Acknowledgements

여전히 부족한 점이 많지만 운이 좋게도 학위 과정 동안 정말 좋은 사람들의 도움을 받아 졸업을 할 수 있었습니다. 이에 이 장을 빌어서 약소하게나마 감사의 말씀을 전합니다.

가장 먼저, 저를 지도해주신 이규철 교수님께 깊은 감사의 말씀을 드립니다. 지식과 연구방법 뿐만 아니라 연구를 대하는 태도, 그리고 연구자로서의 근본적인 목표와 가치관까지 정말 많은 것을 배우고 스스로 생각해 볼 수 있는 기회를 주셨습니다. 또한 연구 교육에 대한 교수님의 끊임없는 고뇌와 실험과 노력을 보고 배우고 느낄 수 있어서 정말 많은 것을 얻고 간다고 생각합니다. 갓 신입생 티를 벗던 저에게 아낌없는 지원을 해주시고 우리 연구실의 새로운 분야에 도전하게끔 기회를 주신 은혜 또한 잊지 않겠습니다.

그리고 저의 연구를 본인 학생의 연구처럼 지도해주시고 함께 고민해주신 김필립 교수님께 감사드립니다. 연구에 대한 흥미를 잃지 않고 언제나 자극을 받을 수 있었습니다. 그리고 연구 결과들을 다시 한 번 돌아보고 깊이 고민할 기회를 주셨습니다. 또한 부족한 저에게 큰 기회와 앞으로 더욱 큰 도전을 할 기회를 주셔서 감사합니다.

MBE 사용법을 가르쳐 주시고 학위기간 내내 저의 입장에 서서 아낌없는 기술적 지원을 주신 조성래 교수님께도 감사드립니다. 새로운 연구를 하기 위한 본인만의 기술을 개발하는 것에 대한 중요성을 배웠습니다. 교수님과 함께 새로운 기술적 시도를 하고 피드백을 주고받을 수 있어서 행운이었습니다.

저의 급작스러운 공동연구 제안을 선뜻 받아 주시고, 같이 고민하시고, 연구 장비를 편하게 사용할 수 있도록 지원해주신 김도헌 교수님께 감사드립니다. 본격적인 연구를 시작하면서 많은 것을 배웠던 논문의 주인공과 함께 연구를 할 수 있어 영광이었습니다.

제가 논문을 쓸 수 있게 큰 도움을 주신 이길호 교수님께도

감사합니다. 먼 거리에서도 제 마음을 모두 알고 있는 듯이 실험을 함께 해 주셔서 감사드립니다. 실험도 배웠지만 협업 태도에 대해 많이 배우고 자극을 받았습니다.

지도교수님과 함께 훌륭한 연구실을 만들어온 연구실 선후배님들께도 감사의 말씀을 드립니다. 저의 처지에서 조언해주시고, 실험도 직접 가르쳐 주시고, 연구 장비도 지원해 주신 이철호 교수님께 감사한 마음을 전합니다. 아울러 박사학위 과정을 함께 한 건욱이형, 현준이형, 석인이형, 준범이형, 홍석이형, 영빈이형 덕분에 연구실 생활을 정말 즐겁게 할 수 있었고, 많은 장점들을 배울 수 있었습니다. 함께 나눈 추억이 두고두고 소중할 것 같습니다. 또한 근동이형과 민호형이 있어서 많은 어려움을 함께 극복할 수 있었습니다. 곧 학위를 잘 마무리하고 앞으로 함께 잘 되길 바랍니다. 그리고 희훈이, 동하, 종우, 지영이에게 모두 고맙고 또 더 잘 도와주지 못해 미안한 마음이 큽니다. 얼마 같이 있지 못했지만 동주, 혁건, 윤재, Asad, Mehdi에게도 같은 마음입니다. 앞으로 원하는 바를 성공적으로 이루기를 바랍니다. 그리고 제 샘플을 열심히 분석해주고 많은 실험을 도와준 장현이형에게도 감사한 마음을 전합니다. 아울러 우리 연구실에서 Post-doc.으로 함께한 Puspendu, Ramesh, Kumar, Hamidul, 현가담 교수님, 윤호상 박사님, Arpana, Dr. Zhou Gang Yi, Dr. Guohua Li, 강문성 교수님으로부터 많은 것을 배우고 도움을 받아 감사하다는 말씀을 전합니다. 그리고 실험을 도와준 혜진누나, 현주씨, 혜진씨, 희나, 지희, 동옥이형, 희수누나, 그리고 행정 업무를 도와주신 강혜영 선생님, 이윤아 선생님, 서경누나 덕분에 연구에 집중할 수 있었습니다.

Also, I extend my sincere gratitude to Young Jae, Hyobin, Austin, Frank, and Katie in Prof. Philip Kim's group for providing kind help and advices. 특히 영재형, 조급한 저의 투정을 들어주면서도 항상 좋은 샘플을 만들어 주셔서 감사합니다. 효빈이형, 서울에서도 미국에서도 실험을 많이 도와주셔서 감사드리고, 또 앞으로 미국에서 많은 도움을 받을 텐데 미리 감사드립니다.

김도헌 교수님 연구실의 제현씨, 제철씨, 재언씨, 지원씨, 원진씨 모두 따뜻하게 대해줘서 감사하고, 제 실험에 직접적 도움이 된 것뿐만 아니라 다른 분야에 대해 현장에서 보고 들을 수 있어서 큰 배움이 되었습니다.

이 모든 과정은 가족의 응원과 지원 없이는 불가능했습니다. 가족에게 감사의 말씀을 드리며 감사의 글을 끝맺고자 합니다. 언제나 제가 하는 일을 지켜보시고, 제 말을 들어주시고, 저를 기다리고 믿어주신 엄마, 이 자리를 빌어서 정말로 고맙고 사랑한다는 말을 전합니다. 안 그래도 힘드셨을 텐데, 박사 학위를 하면서 오랜 시간 동안 바쁘다는 핑계로, 또 그 와중에 결혼을 하며 옆에서 더 같이 얘기하고 시간을 보내지 못해서 죄송합니다. 그리고 제가 여기까지 온 건 다 제가 어렸을 적 아빠가 주신 호기심과 가치관 덕분이에요. 언제나 그랬듯이, 제 연구실 책상에서 이 과정을 함께 해왔다고 생각해요. 그리고 장모님, 장인어른께 두 분의 도움이 없었다면 이렇게 대학원 생활을 할 수 없었을 거예요. 저에게 엄마 아빠처럼 가족이 되어 주셔서, 제 편에서 응원해주셔서 정말 감사드립니다. 그리고 나에게 위로를 주고 머리 식힐 기회를 만들어주는 정은이에게도 고맙고, 자기 일만 생각하여 친근하고 좋은 오빠가 되어주지 못해 미안하다. 그리고 준하도 나에게 형제가 되어줘서 고맙고, 대학원 생활 동안 즐거움을 줘서 고맙다. 마지막으로 20살에 저를 만나서 지금까지 이 모든 과정을 함께한 내 사랑, 재랑이에게 가장 깊은 고마움을 전합니다. 내게 최고의 연인이고, 최고의 친구이고, 이 모든 것을 버티고 이겨내게 한 가장 큰 버팀목이었어. 함께여서 올해부터 우리 둘에게 펼쳐질 새로운 일들이 기대가 되고 즐겁게 다가오는 것 같아. 고맙고 사랑해.

Table of Contents

List of Figures

List of Tables

1 Introduction

1.1 Motivation

One of the most exciting scientific discoveries of the past two decades is the emergence of a new class of low dimensional materials. In particular, the ultimate two-dimensional (2D) limit of a number of layered systems has been realized by tremendous research activities [1,2]. In these systems, weak van der Waals (vdW) forces hold the layers together. This new class of materials, termed vdW materials, includes graphene, hexagonal boron nitride (hBN), transition metal dichalcogenides (TMDs) and some of group V_2–VI_3 compounds. Together these materials represent various electronic systems, including metals, insulators, semiconductors, superconductors, and topological insulators (TIs) [3-5]. Built upon the success of graphene research, the idea of engineering 2D atomic layers of vdW materials and their heterostructures has become compelling [6,7]. The availability of atomic layers with various electronic properties enables one to assemble these layers and produce new vdW heterostructures with unexplored properties. The emergence of new physical phenomena at the heterogeneous interfaces and the new technologies providing the ability to quantum engineer the heterostructures are expected to result in integration of new functionalities and novel device concepts. Especially, the recent prediction and discovery of

the topological electronic states occurring at the interface between electrically dissimilar atomic layers brought a surge of research interest in topological vdW heterostructures [5,8,9], which provide material platforms for novel quantum electronic and optoelectronic device applications. While significant progress has been made in the preparation of such materials and heterostructures by mechanical exfoliation/stacking [10] and chemical vapor deposition (CVD) [11], it has been challenging to obtain ultra-high purity materials and to construct vdW heterostructures with atomic precision due to their limited controllability. In order to acquire high-quality materials with low defect concentrations and precise atomic controllability of the vdW interface, a more controlled and engineered materials growth approach such ultra-high vacuum molecular beam epitaxy (UHV-MBE) and the development of novel device fabrication and characterization techniques are necessary.

1.2 Objective and Approach

The goal in this dissertation is to design and engineer topological heterointerfaces based on 2D vdW layered materials toward the realization of novel quantum electronic devices. I developed a new approach combining micromanipulation of vdW materials, MBE growth, and transmission microscopy (TEM) techniques in order to achieve high-quality vdW

heterostructures with (i) atomically sharp and clean interfaces; (ii) uniform and well-defined structural properties formed through the heteroepitaxy; and (iii) accessibility to both surfaces of the vdW substrate material. It is also compatible with nanodevice fabrication techniques (Figure 1.1). The ability to design and build such functional mesoscopic templates provides ample opportunities to investigate quantum phenomena at the heterointerfaces between high-quality vdW atomic layers and can be utilized for novel nanoscale engineered device applications. Here, I have in particular focused on the topological electronic transport across the vdW heteroepitaxial interfaces between TIs and hBN: (1) lateral transport *via* high-quality vdW interfacial topological surface states (TSSs) in TI/hBN heterostructures and (2) vertical tunneling across atomically sharp interfaces of TI/hBN/TI heterostructures.

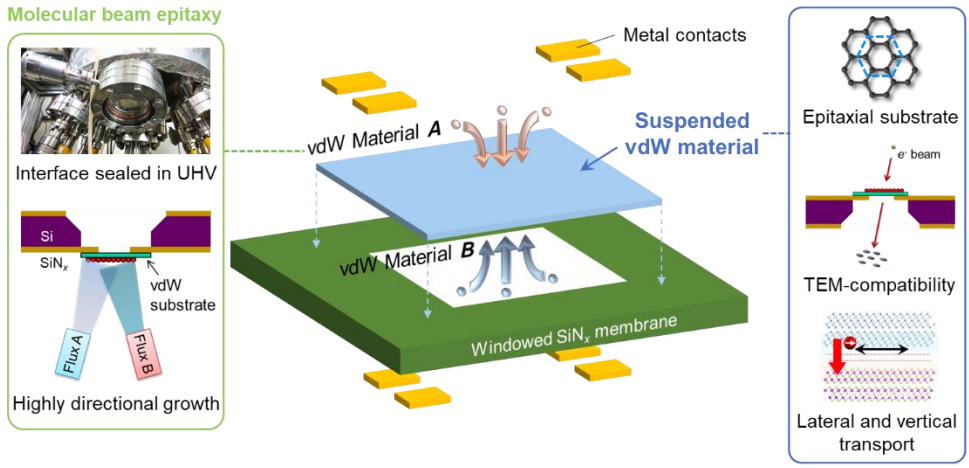

Figure 1.1 Approach developed in this dissertation: Micromanipulation, MBE, TEM, and nanofabrication combined technique for atomically engineered vdW quantum heterostructures for novel device applications.

1.3 Outline of the Thesis

The dissertation is composed of six chapters including this introductory chapter. In the following Chapter 2, I briefly introduce recent research activities on MBE-grown topological insulator-based vdW heterostructures and electronic transport in lateral and vertical vdW heterostructures. The experimental techniques, including construction and operation of the molecular beam epitaxy system, novel methods for combining MBE with micromanipulation of vdW materials, device fabrication processes, and structural and electrical characterizations that have been used in this dissertation are described in detail in Chapter 3. Chapter 4 presents the comprehensive study on the MBE growth of high-quality topological insulator Bi_2Se_3 thin films on hBN layers and their structural and electronic transport properties. Uniform films with atomically smooth terraces over a large area have been prepared *via* so-called van der Waals heteroepitaxy, and they exhibited dominant conduction through high mobility TSSs at the Bi_2Se_3/hBN interface. The expandability of the growth scheme to various TI/vdW material combinations is also discussed. In Chapter 5, vertical tunnel junctions based on TI/hBN/TI vdW heterostructures prepared by heteroepitaxial growth of TI layers on and under the suspended a few atomic layers thick hBN layers are demonstrated. Tunneling spectroscopy of the Sb_2Te_3/hBN/Bi_2Se_3 and Bi_2Se_3/hBN/Bi_2Se_3 devices under in-plane and out-of-plane magnetic fields for the investigation of the energy, momentum,

and spin selection rules of the electrons tunneling between TSSs are discussed. Finally, Chapter 6 summarizes this dissertation and gives the outlook for future works.

2 Background and Literature Survey

This chapter reviews research activities on topological insulator-based van der Waals heterostructures and novel interfacial electronic transport properties in lateral and vertical van der Waals heterostructures. After a general review of topological insulators in terms of material quality and preparation methods, MBE growth approaches of topological insulator-based van der Waals heterostructures for achieving high-quality TI materials are discussed more in details. Next, some examples of lateral and vertical van der Waals heterostructures and electronic transport properties of novel quantum electronic states realized in the systems are reviewed, focusing on the heterostructures consisting of graphene — an analogue to TI — and hBN.

2.1 MBE Growth of Topological Insulator-Based van der Waals Heterostructures

Three-dimensional (3D) topological insulators, a new state of quantum matter, have become one of the most compelling materials in the field of condensed matter physics and material science due to their exotic electronic properties; they are bulk insulators possessing topologically protected gapless Dirac surface states with helical spin nature, possessing

potential applications in spintronics topological quantum computing (Figure 2.1) [12-14]. Among several 3D TI materials proposed so far, while the 3D TI was first experimentally realized in Bi_xSb_{1-x} compounds, Bi_2Se_3, Bi_2Te_3, Sb_2Te_3, and their alloys have been intensively studied due to their TSSs located in the relatively large bulk bandgap energies (~0.3 eV for Bi_2Se_3) [15] and their van der Waals layered crystal structures [16], significantly benefiting from the rapidly growing technologies for vdW materials as exemplified in this dissertation.

While significant progress has been made to date, obtaining high-quality TI crystals with low enough concentrations of structural defects has been challenging. Besides the fact that the defects frequently result in reduced carrier mobility and doping of TIs which moves the Fermi level away from the Dirac point of TSSs, recent microstructural and electronic transport investigations have revealed that some defects hinder the formation of TSSs. Y. Liu *et al*. demonstrated, by scanning tunneling microscopy/spectroscopy (STM/STS) experiments and first-principles calculations, that the TSS of Bi_2Se_3 can be destroyed by the compressive strain arising from the grain boundaries in the film (see Figures 2.2(a)–(c)) [17]. In Ref. [18], M. Brahlek *et al*. reported that extended bulk states make crosstalk between the top and bottom TSSs of TI films even though the film is far thicker than the limit of direct surface wave function overlap as displayed in Figure 2.2(d). After the suppression of the parasitic bulk states by compensation doping, the two TSSs

became fully decoupled and exhibited enhanced transport properties. Therefore, for the demonstration of controlled device fabrication fully utilizing TI transport characteristics, it is crucial to obtain high-quality TI materials with a reduced concentration of defects.

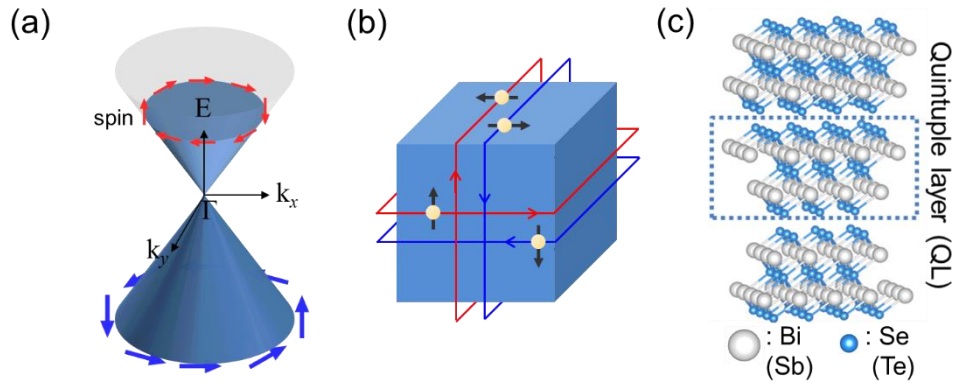

Figure 2.1 Illustrations schematically showing topological surface states of 3D TIs in the (a) *k*-space and in the (b) real space. Red and blue arrows represent the helical spin texture of TSSs. (c) Van der Waals layered crystal structure of 3D topological insulator Bi_2Se_3, Bi_2Te_3, Sb_2Te_3, and their alloys.

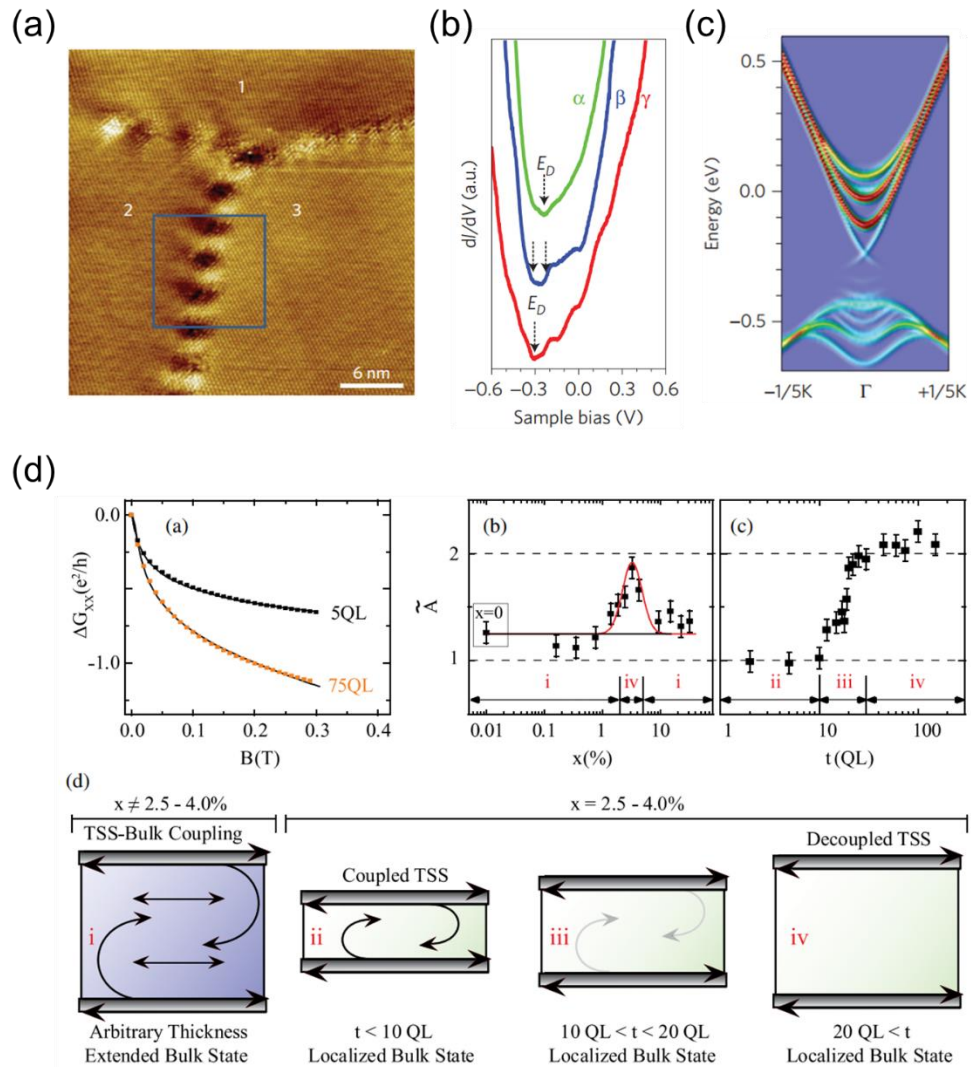

Figure 2.2 (a)–(c): Effects of grain boundaries on the electronic properties of the Bi_2Se_3 films grown on SiC(0001). (a) STM image of grain boundaries in the film. (b) STS dI/dV spectra taken at different position of the film. α: away from the grain boundary, β: on the bright region and γ: on the dark region of the grain boundary. In spectrum β, a gap of 60 meV is observed. In γ, the Dirac point is shifted by –90 meV with respect to α. (c) Calculation of Bi_2Se_3 surface states under an in-plan compressive strain (c/a ratio +6% of the bulk value). (d) Weak anti-localization effect measurements on Cu-doped Bi_2Se_3 thin films grown on Al_2O_3(0001). The dependence of the effective number of conduction channels on the Cu doping and the thickness are displayed, describing the coupling and decoupling conditions of the top and bottom TSSs. Panels (a)–(c) are adapted from Ref. [17]. Panel (d) is reproduced from Ref. [18].

One of the promising methods for the synthesis of high-quality, single crystalline TI materials is the heteroepitaxial growth on a single crystal substrate with a compatible lattice structure. Given that the heterointerface between TI and substrate greatly affects the formation of TSS [19], the growth of vdW-layered $(Bi_xSb_{1-x})_2(Se_yTe_{1-y})_3$ on another vdW-layered single crystal substrate through the so-called "*van der Waals epitaxy*" can be a particularly promising approach. According to the pioneering works on the vdW epitaxy by A. Koma *et al*., the lattice matching condition can be dramatically relaxed owing to the weak vdW interactions at the interface between the substrate and the growing material [20]. It is in sharp contrast to the conventional heteroepitaxy where a strong covalent bonding is present at the interface; thus the lattice mismatch between the substrate and the growing material usually results in the formation of defects at the interface as depicted in Figure 2.3(a). In the vdW heterointerface, on the other hand, the absence of dangling bonds at the interface can greatly reduce the concentration of substrate-induced extended defects (Figure 2.3(b)). Moreover, the atomically flat vdW interface can provide an ideally noninvasive environment for the TSS. Meanwhile, through the energy minimization scheme, the vdW interaction still can provide the epitaxial alignment to the growing material, which can lead to uniform and well-defined structural properties of the film.

Indeed, high mobility TSS has been obtained in Bi_2Te_2Se nanoplatelets on hBN, a topologically trivial wide bandgap vdW-layered

insulator, grown by the vdW epitaxy using a vapor-solid method in a CVD tube furnace system (Figure 2.4) [21]. While the mobility of TSSs at the Bi_2Te_2Se/hBN interface was high enough for the observation of Shubnikov-de Hass oscillations, the carrier density of the bulk was 1 or 2 orders of magnitude higher than that of surface states. Also, the thickness and the domain sizes of nanoplatelets were not uniform over the hBN substrate. Accordingly, it is desirable to employ a growth approach that provides a cleaner growth environment and more control over growth parameters.

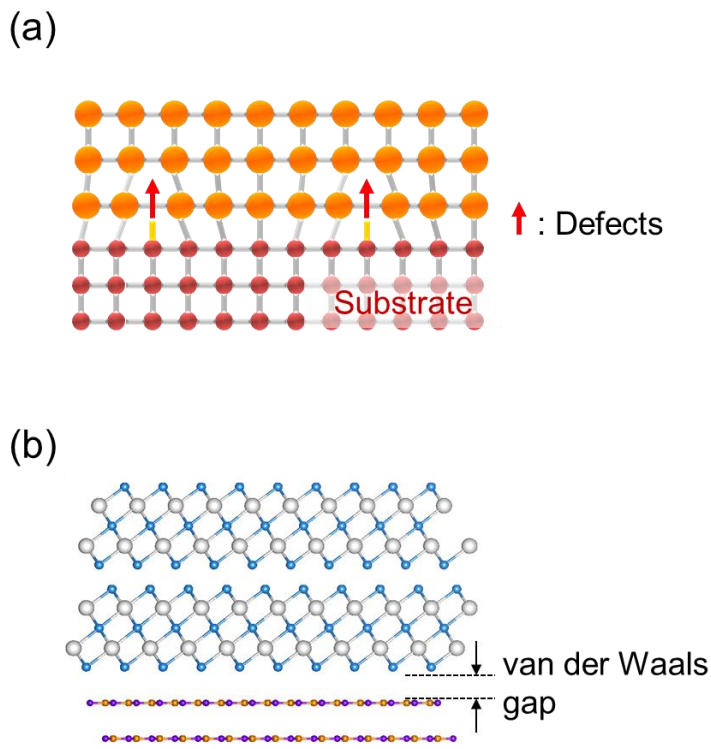

Figure 2.3 Schematic diagrams showing (a) conventional heteroepitaxy and (b) van der Waals epitaxy.

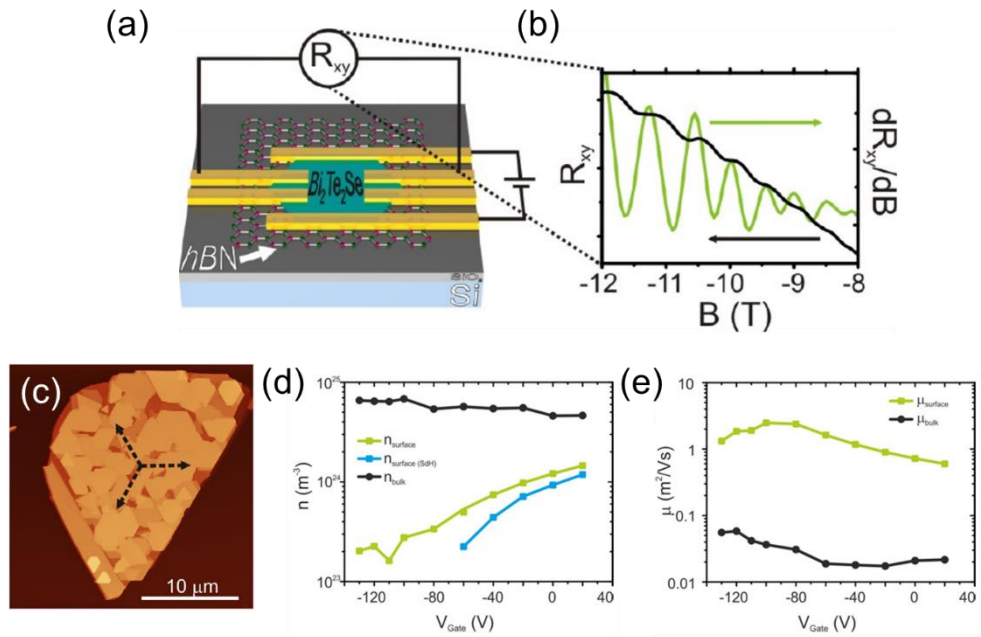

Figure 2.4 High-mobility TI nanoplatelets grown on hBN by vdW epitaxy (adapted from Ref. [21]). (a) Schematic diagram of the Bi_2Te_2Se nanoplatelet/hBN device. (b) Hall resistance at high magnetic fields and its first derivative as a function of the magnetic field exhibiting Shubnikov-de Haas oscillations. (c) Atomic force microscopy (AFM) image of the Bi_2Te_2Se nanoplatelets grown on hBN by the CVD method, showing steps and domains with different heights. Comparison of bulk and surface carrier (d) densities and (e) mobilities at different gate voltages, obtained by the fitting of Hall resistivity data with the two-conduction channel model.

Molecular beam epitaxy, in particular, has played an important role in achieving a truly bulk-insulating TIs with enhanced and controlled electronic properties [22]. This technique uses ultra-high purity reactant sources and utilizes an extremely clean (UHV) environment during the growth that can yield high-quality materials that have extremely low defect concentrations. Moreover, the ability to precisely control the growth parameters including molecular fluxes and real-time, *in-situ* monitoring of the growth by reflection high-energy electron diffraction (RHEED) provide an atomic scale control on thickness, composition, and growth mode of the growing materials and thereby can yield atomically sharp interfaces between heterogeneous layers.

The concept of the vdW epitaxy has also been employed in the MBE growth of TI films. The first example is MBE growth of Bi_2Se_3 thin films on epitaxial graphene (EG), which is prepared by thermal decomposition of SiC substrates. This system served as a high-quality, versatile platform for the investigation of the electronic structures of TIs using STM/STS and angle-resolved photoemission spectroscopy (ARPES) [23-25]. However, probing of its electrical transport properties, especially for the bottom TSS, is inhibited by the presence of conducting graphene layer at the interface. In addition, the existence of periodic terrace steps on the surface of EG/SiC, whose lateral size is typically less than a few micrometers [26], may be deleterious to the interfacial TSS [25,27]. Recently, the MBE group at Rutgers University has

made significant progress in achieving high-quality TI thin films with an ultra-low carrier density and enhanced carrier mobility *via* interface engineering scheme (Figure 2.5) [19,28]. They utilized insulting vdW-type buffer layers which relax the large lattice mismatch between the TI thin films and the substrate (Al_2O_3(0001)) and reduce the interfacial and bulk defects. Thanks to the high film quality, they were able to observe the quantum Hall effect (QHE) for the first time in Bi_2Se_3 and, in Sb_2Te_3, they observed the QHE at a much lower magnetic field than the previously required field. Nonetheless, there still exists room for further improvement in the performance as the unintentional interlayer diffusion of indium in the buffer layer and its incorporation into the TI film is inevitable. In addition, the buffer layer exhibits sub-micrometer step edges, forming stepped interfaces with the TI film.

There have been attempts to grow TI thin films, using MBE, on the cleaved surfaces of insulating vdW layered materials such as muscovite mica ($KAl_2(AlSi_3O_{10})(OH)_2$) [29,30]. The enhancement in the performance, however, was rather limited, presumably because of the relatively high physical roughness and chemical inertness of mica [31]. In principle, composed of atomically planar layers with chemically inert surfaces, hBN is one of the most suitable candidates for the ideal vdW epitaxy and the high-quality electronic transports through the interfacial TSSs [32-35]. Very recently, after the publication of the work presented in Chapter 4 of this

dissertation [32], microstructural properties of the $(Bi_xSb_{1-x})_2Te_3$ thin films grown on hBN substrates by MBE have been investigated by D. R. Hickey *et al.* [36]. It suggests that the 2D nature of the substrates has influenced the formation and behavior of the microstructural defects in the films in an unconventional manner, and those defects could have impacts on the devices based on these TI films (Figure 2.6). Therefore, it is crucial to develop a new growth scheme that yields high-quality TI thin films overcoming the challenge posed by the weak vdW nature of the substrate–film interaction and to develop novel material characterization techniques.

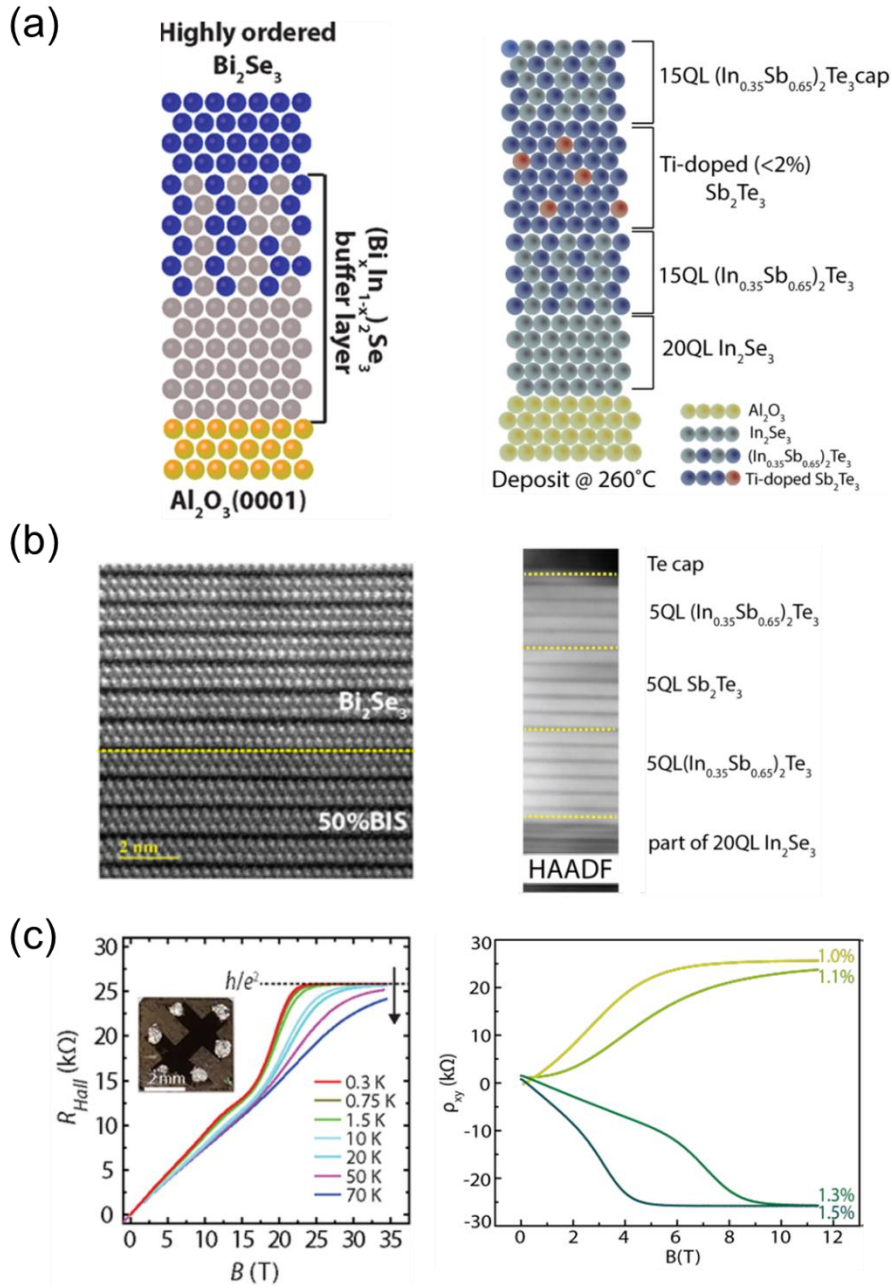

Figure 2.5 Ultra-low carrier density and high-mobility TI thin films realized by vdW-type interface engineering using MBE. Left column: Bi_2Se_3 grown on $(Bi_{0.5}In_{0.5})_2Se_3/In_2Se_3$ buffer layer. Right column: Ti-doped Sb_2Te_3 grown on $(In_{0.35}Sb_{0.65})_2Te_3/In_2Se_3$ buffer layer. (a) Schematic diagrams of the heterostructures. (b) Cross-sectional high-angle annular dark-field scanning transmission electron microscopy (HAADF-STEM) images showing the atomically sharp interfaces between the TI layers and the buffer layers. (c) QHE observed in the systems. Panels on the left column are adapted from Ref. [19]. Panels on the right column are adapted from Ref. [28].

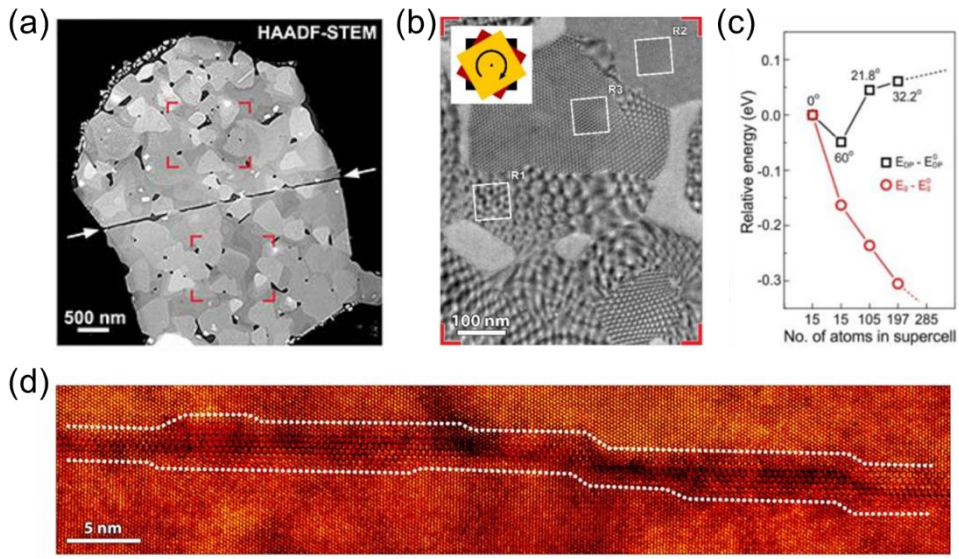

Figure 2.6 (a) Plan-view HAADF-STEM image of MBE-grown $(Bi_xSb_{1-x})_2Te_3$ films on an hBN flake. (b) Magnified TEM image showing Moiré patterns originated from relative layer rotations within the $(Bi_xSb_{1-x})_2Te_3$ film. (c) DFT-calculation of the intra-layer rotation dependent band structure of TI. (d) HAADF-STEM image showing the coexistence of a second phase (tellurium phase) along the grain boundary in the film. Panels are adapted from Ref. [36].

2.2 Novel Lateral and Vertical Electronic Transports in Atomically Engineered van der Waals Heterostructures

The ability to engineer the vdW interfaces with atomic precision has opened up a wealth of opportunities to construct a new type of 2D quantum heterostructures. As a member of the vdW materials family, a 3D TI material such as Bi_2Se_3, Bi_2Te_3, and Sb_2Te_3 can be involved in the heterostructures for discovery and engineering of the novel topological electronic states. Here, some pioneer works on the lateral and vertical electronic transport properties of the vdW heterostructures composed of graphene and hBN are discussed, while the schemes can be applied to TIs considering the similarity that graphene and TIs both exhibit gapless Dirac states; the Dirac states of TIs can be roughly regarded as 1/4 — spin and valley degeneracies each account for 2 — of graphene's Dirac states [13,14].

hBN is an attractive material that has great advantages as a dielectric substrate in vdW heterostructures thanks to its (i) wide bandgap of 5.97 eV, (ii) atomically flat surfaces, and (iii) high chemical inertness — free of dangling bonds and charge traps at the surface due to the strong in-plane ionic bonding [37,38]. By transferring graphene on hBN layers, the carrier mobility of graphene was enhanced by one order of magnitude when compared to that measured in graphene-on-SiO_2 (Figures 2.7(a) and (b)) [33]. Graphene on hBN also showed reduced carrier inhomogeneities and intrinsic doping. The quality of graphene-based devices has been further improved by the

encapsulation of graphene between the top and bottom hBN layers using the dry, polymer-free vdW assembly technique and the introduction of the one-dimensional (1D) atomic edge contact scheme (Figures 2.7(c)–(f)) [39]. This technique has brought the carrier mobility of graphene near to its phonon-limit of 140,000 $cm^2 V^{-1} s^{-1}$ at room temperature and realized the ballistic transport over length scales exceeding device sizes at low temperature. Based on the successful demonstration of enhanced electronic properties of graphene on hBN substrates, together with the suitability of hBN as a substrate for the vdW epitaxy of high-quality TI films discussed in the previous section, one can expect the enhancement in electronic properties of TSSs at the heterointerface of the TI/hBN vdW epitaxial heterostructures.

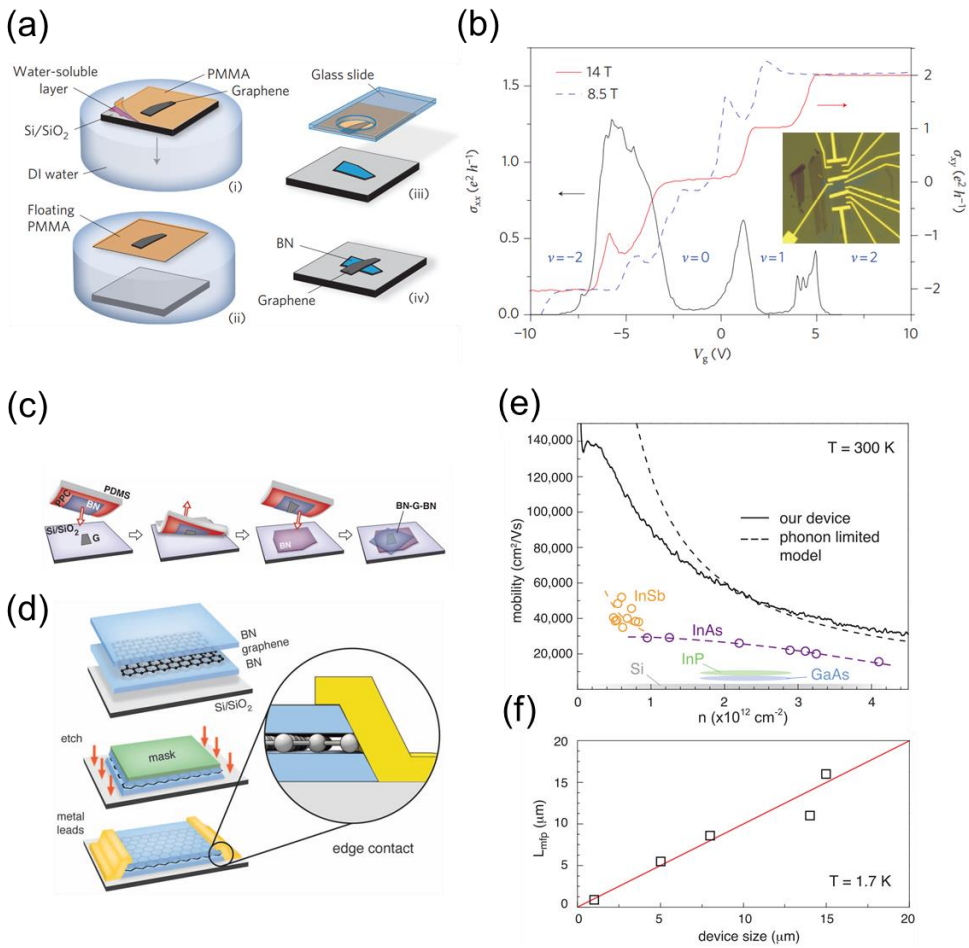

Figure 2.7 (a) Polymer-assisted wet transfer of graphene layer on hBN substrates. (b) Graphene-on-hBN showing well-resolved quantum Hall effects due to enhanced electronic properties compared to graphene-on-SiO_2. (c) Polymer-free dry vdW assembly of hBN/graphene/hBN. (d) Schematics of 1D edge contact of hBN-encapsulated graphene. (e) Room temperature mobility as a function of the carrier density of the hBN/graphene/hBN device reaching the theoretical phonon limited values. (f) Mean free path of the devices limited by the device sizes at $T = 1.7$ K. Panels (a) and (b) are adapted from Ref. [33]. Panels (c)–(f) are adapted from Ref. [39].

When the thickness of hBN is reduced to the atomic levels, electrons can quantum mechanically tunnel through the hBN barrier [40,41]. As a single crystalline and atomically planar insulator, hBN offers an ideal tunnel barrier for tunneling devices made of vdW materials. For example, in the graphite/hBN/graphene vdW tunnel junctions where the hBN serves as a tunnel barrier and the graphite is for a probe, the electronic structures of graphene could be probed with unprecedented high signal-to-noise ratios by tunneling spectroscopy (Figure 2.8) [42]. Meanwhile, by sandwiching a thin hBN layer between two graphene layers, resonant tunneling transistors have been demonstrated [43,44]. Furthermore, the precise alignment of two graphene layers in the graphene/hBN/graphene vertical vdW heterostructures and the use of strong in-plane and out-of-plane magnetic fields made it possible to discover and control the energy, momentum, and chiral properties of the tunneling Dirac fermions (Figure 2.9) [45-47]. Likewise, it is highly attractive to make TI/hBN/TI heterointerfaces and to investigate the momentum-space selection rules of the tunneling helical Dirac fermions in the two high-quality TI/hBN interfacial TSSs.

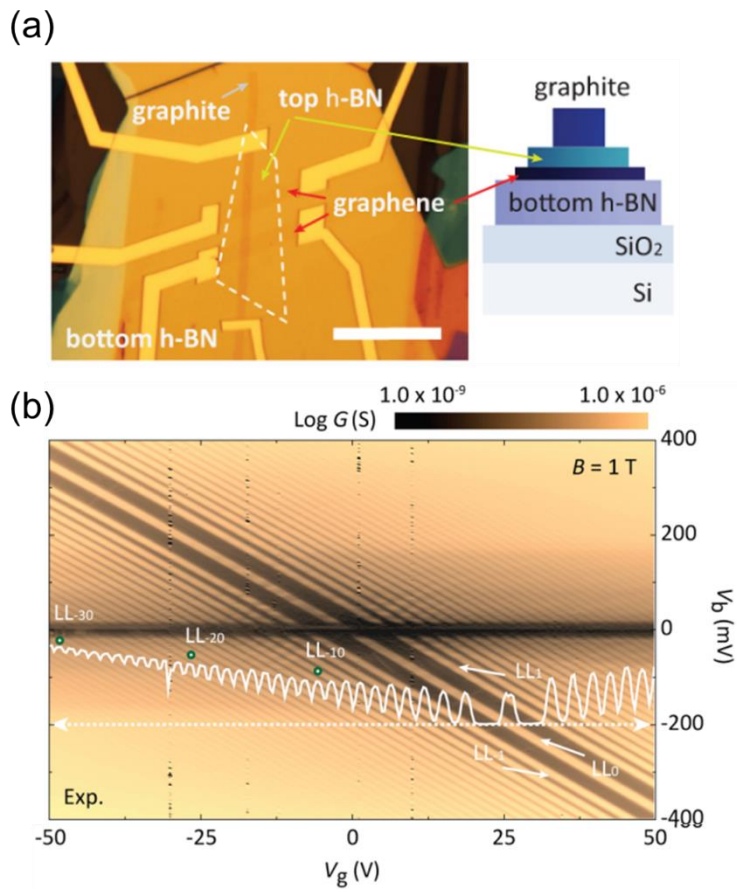

Figure 2.8 (a) Optical image and schematic diagram of the graphite/hBN/graphene tunneling device on a SiO_2/Si substrate. Scale bar: 20 μm. (b) High-resolution differential tunneling conductance dI/dV_b map at various bias V_b and gate V_g voltages of the device at $T = 5$ K and $B = 1$ T. The white plot is the line cut at $V_b = 200$ mV, displaying over well-separated 30 Landu levels. Panels adapted from Ref. [42].

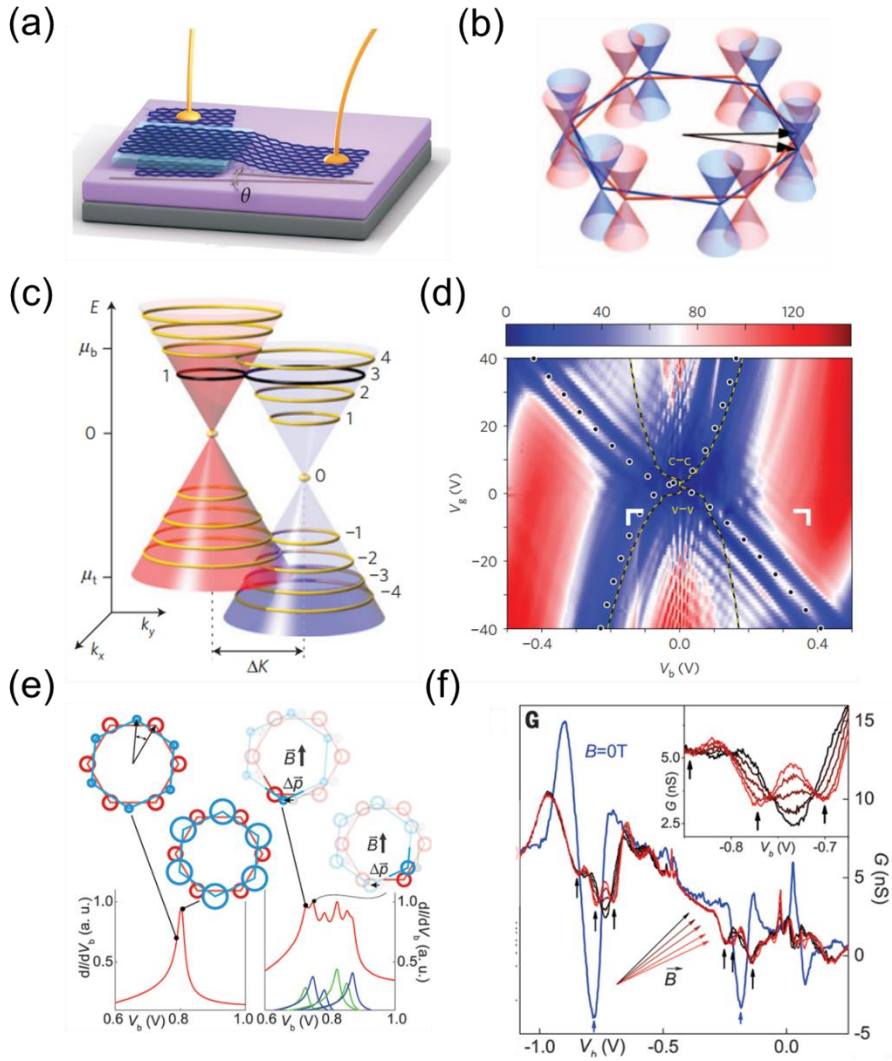

Figure 2.9 (a) Schematic of graphene/hBN/graphene tunneling device. (b) Small misalignment angle θ between the two graphene electrodes leading to a momentum mismatch between the two Dirac bands in the reciprocal space. (c) Resonant tunneling conditions between the two Landau levels developed in the graphene layers by out-of-plane magnetic field $B_\perp$. (d) dI/dV_b (V_b, V_g) at $T = 4$ K and $B_\perp = 2$ T. Color scale is in μS. Tunneling between equivalent bands is enhanced compared to tunneling between different bands. (e) Schematic representations of resonant tunneling conditions under in-plane magnetic fields $B_\parallel$. The tunneling electrons gain an additional in-plane momentum by the act of the Lorentz force. (f) dI/dV_b at $B_\parallel = 0$ and 30 T with various angles, manipulating the chiral properties of the resonant tunneling conditions. Panel (a) is adapted from Ref. [45]. Panels (b), (e), and (f) are adapted from Ref. [47]. Panels (c) and (d) are adapted from Ref. [46].

3 Experimental Techniques

3.1 Molecular Beam Epitaxial Growth of Topological Insulator Thin Films on van der Waals Layered Materials

3.1.1 The molecular beam epitaxy system used in this work

The MBE system used in this work, a home-built compact machine, was originally designed as a laser-MBE for oxide film growth, and then modified into a gas source MBE. However, due to technical issues, the system has been out of operation for a while. In 2012–2013, I and Dr. Hongseok Oh rebuilt the system as a full solid-source MBE for TI material growth, after a thorough — mechanical, chemical, and thermal — cleaning of vacuum chambers and complete replacement of major components such as heating, pumping, and source parts.

The MBE system is composed of two vacuum chambers: the main (growth) chamber and the load-lock chamber. All vacuum chambers are constructed of type 304 stainless steel with electropolished surfaces and sealed by ConFlat (CF) flanges and oxygen free high conductivity (OFHC) copper gaskets (Accu-Glass Products).

The load-lock chamber is for loading and unloading samples without breaking the UHV of the main chamber. It is equipped with a quick access

door (QD-450-CH, MDC Vacuum Products) for sample loading/unloading and a diaphragm-sealed valve (SS-DSV51, Swagelok) which is connected to a high-purity nitrogen cylinder for venting. The gate valve (Series 108 UHV, VAT) between the load-lock and the main chamber was opened at a pressure of ~10^{-7} Torr. The load-lock chamber is made of a 4.5" outside diameter (O.D.) CF flange 6-way cross (No. 407004, MDC Vacuum Products), which is pumped by a 60 *l*/s turbomolecular pump (TMU 071 P; Pfeiffer Vacuum) backed by a 3.3 m^3/h diaphragm pump (MD-4T, Vacuubrand). The pressure of the chamber is monitored by the Compact FullRange gauge (PKR 251, Pfeiffer Vacuum), which consists of the Pirani and the cold cathode system. The chamber's small vacuum volume compared to the pumping speed of the turbomolecular pump greatly reduces the pumping time. A magnetically coupled transporter (MT-24, MDC Vacuum Products) attached to the load-lock chamber is used to transfer samples between the load-lock chamber and the main chamber, and it is capable of loading two substrate holders so that one can unload a sample from the main chamber and load the next one into it at the same time. In addition, the load-lock chamber is equipped with a linear motion feedthrough (VF-173-4, Huntington Mechanical Labs) for *in-situ* cleaving of vdW materials.

The main chamber, a custom-designed chamber manufactured by Korea Vacuum Tech having inside diameter (I.D.) of 340 mm and flange O.D of 16.5", is pumped by two turbomolecular pumps connected in series — a

primary 900 *l*/s pump (ATP 900C, Adixen which is now Pfeiffer Vacuum) and a secondary 67 *l*/s pump (HiPace 80, Pfeiffer Vacuum) — backed by a 23.3 cfm (~11 *l*/s) rotary vane pump (RVP2033SD, Adixen). The secondary turbomolecular pump increases the compression ratio and prevents saturated oil vapors from backstreaming. A pneumatic angle valve (KAV-150-P, MDC Vacuum Products) with a return spring is installed in the foreline, automatically closing in case of electricity failure. Note, however, that it is highly recommended to use an oil-free backing pump such as scroll pump or multistage roots pump for maintaining high-purity chamber conditions. The chamber pressure is measured by a cold cathode gauge (Series 943 digital controller with a Series 421 sensor, MKS Instruments). The base pressure of the main chamber can reach the low 10^{-10} Torr range at room temperature after a careful bakeout procedure. During a growth procedure, the cryoshroud (I.D. 276 mm and O.D. 336 mm) in the main chamber is filled with liquid nitrogen to trap the residual gases, and the chamber pressure during the growth can be maintained in the range of low 10^{-10} Torr in spite of radiations coming from heating elements such as the substrate heater and effusion cells.

The bakeout is performed using heating tapes attached on the outer surface of the chambers. They are further wrapped by multiple layers of aluminum foils to preserve and distribute the heat uniformly. Since the chamber contains Se which has a very high vapor pressure, the bakeout should be carried out at low temperatures (typically 80–120^{o}C).

The system has four effusion cells (Knudsen cells) for Bi, Sb, Te, and Se, and an electron beam (e-beam) evaporation source for Nb, and there are two more 4.5” O.D. CF flanges for additional effusion cells. The chamber is of vertical type with a source flux incident angle of 18^{o}, and the nominal distance between the mouth of the effusion cell and the substrate is 290 mm. The source cells have in-vacuum length of 260 mm and are mounted on 4.5" O.D. CF flanges. The main base for mounting source cells, the bottom half of the main chamber, and the e-beam gun are cooled by water. All effusion cells and the corresponding electrical and pneumatic controlling parts, and the main base were designed by Prof. Sunglae Cho at the University of Ulsan and purchased from his company, Effucell. The main base and mounting flanges of the effusion cells were manufactured by Mtech. Each effusion cell has an independent pneumatic rotary motion shutter (material of shutter blade: molybdenum, pneumatic rotary motion feedthrough: Motech Vacuum, solenoid valve and controller: Series VQ2000, SMC Pneumatics), a 600 W (40 V, 15 A) DC power supply (EF4015, Effucell), and a PID temperature controller (DB1000B, Chino). The source flux is controlled by the cell temperature; the cell is radiatively heated by tantalum wires, and the temperature is measured by a K-type thermocouple. The low-temperature design optimized for 200–700^{o}C is employed for Bi and Sb cells while the very low-temperature hot-lip type heater design is employed for Se and Te cells to prevent clogging of the outlet of the effusion cells. For these two cells, the thermocouple is located near the Ta heater, which is wound only at the

mouth of the effusion cell, for stable temperature control, so the nominal temperature read by the thermocouple is much higher than the actual temperature of the source material.

High-purity elemental sources (Bi: 99.999%, low oxide, No. 38619; Sb: 99.9999%, No. 11071; Te: 99.9999%, No. 42213; Se: 99.999+%, No. 00290; Alfa Aesar which is now Thermo Fischer Scientific) are loaded in 35 cc quartz crucibles (GE-214 grade, Hanjin Quartz). The quartz crucible is of cylindrical shape with I.D. × O.D. × length of 19 × 22 × 141 mm^3 with an endplate which as O.D. and thickness of 35 mm and 1.5 mm, respectively, and R = 2 mm joint with the cylinder.

As bismuth is in the liquid phase during the growth, and the volume of bismuth increases when it solidifies, the temperature of the bismuth cell is always kept well above the melting temperature of Bi (stand-by temperature: 360^{o}C, melting temperature: 271.5^{o}C). The Bi cell should be slowly cooled down (–2 or –3^{o}C/min.) when bringing it down to room temperature crossing the melting temperature. In addition, the crucible for bismuth is designed in a dual-walled structure, having a cylindrical quartz liner of 16 × 18 × 135 mm^3, which prevents the liquid phase bismuth from flowing down in case that the inner crucible is broken. The other elements are sublimating from solid phases.

Before the loading of the materials, the effusion cells and the crucibles were degassed at high temperatures in a high vacuum to minimize

the chance of contamination of the source materials. The crucibles are then filled with the source materials less than half the crucible length. After source loading, vacuum pumping, and bake-out, a careful degassing of each source was performed before the sample growth.

The e-beam gun (Model 508-99 EB Source, Telemark), operating at –5.00 kV, contains Nb slugs (99.95%, No. 42845, Alfa Aesar) loaded in a 1.5 cc graphite crucible (No. CGCRYJ0030, iTasco). It has a manual rotary shutter whose blade is made of molybdenum and further covered by a thin niobium foil. It is connected to a water chiller since it demands substantial cooling capacity and constant cooling power is necessary for a stable flux. The flux of the material is controlled by the e-beam emission current. The high voltage power supply (e-vap CVS-3, MDC Vacuum Products) and the chiller are shared with an e-beam evaporator machine.

A water-cooled quartz crystal microbalance (QCM; Inficon), placed near the substrate manipulator and equipped with a custom-made shutter made from a molybdenum foil and tantalum wires, is used for the measurement of source fluxes. The actual growth rate is calibrated after the sample growth by measuring the thickness of the film using atomic force microscopy and cross-sectional transmission electron microscopy.

The sample holders, purchased from HITC, are made of molybdenum blocks with a diameter of 30.8 mm. The substrates are either glued onto the

holder plates using liquid phase gallium (99.999%, No. 263273, Sigma-Aldrich which is now Merck) or placed (hung) on the holders with small stepped windows. The holders were cleaned in hot baths of TCE, acetone, methanol, and isopropyl alcohol (IPA). Before the first use of a new holder, additional cleaning in aqua regia followed by thermal degassing were carried out.

The sample is radiatively heated by a UHV heater, purchased from Effucell, located in the bottom of the substrate manipulator. The substrate heater is made of Ta wires, Mo frames, and alumina insulating parts. Its power is controlled by a PID controller (Model 2404, Eurotherm) and a thyristor (as known as silicon controlled rectifier; SCR) power controller (TE10A series, Eurotherm) a transformer. The substrate temperature is monitored by a K-type thermocouple (Omega) which lies ~ 1 cm above the sample holder. Since the thermocouple is not in contact with the sample holder, there is a temperature difference between the substrate surface and the thermocouple. While the growth temperatures described in this dissertation is given in the nominal thermocouple temperatures as the temperature control was reproducible and stable, the surface temperature of the substrate can be calculated (calibrated) by measuring the melting temperatures of various materials. Materials having very low vapor pressure up to their melting points are particularly useful: Ga (29.76^{o}C), In (156.6^{o}C), Sn (231.9^{o}C), and (Bi 271.5^{o}C). The substrate temperature can also be monitored by an infrared

pyrometer (Raynger 3i, Raytek) through a view port at the bottom of the chamber.

The substrate manipulator has mechanical functions of azimuthal rotation (by a motor), linear z-motion (by a manual single axis Z stage, LMT-252, MDC Vacuum Products), and tilting (by a bellows port aligner). Below the substrate manipulator, there is a custom-made substrate shutter composed of three layers of molybdenum foils in a radiation shielding structure connected by tantalum wires to a manual rotary motion feedthrough (HTBRM-133, MDC Vacuum Products).

The system is equipped with a RHEED (RHD307, Pascal) gun and a 90 mm dia. phosphor screen (VSI), and a CMOS camera for *in-situ* monitoring of the growing surface. I note, however, that RHEED is ineffective for monitoring the growth on exfoliated vdW crystallites due to their small sizes in the order of 10^1 μm × 10^1 μm, considering that a typical sampling size of RHEED is 10^2 μm × 10^3 μm. Instead, I utilized specially designed mesoscopic vdW templates for MBE growth and subsequent TEM structural analysis, whose preparation details will be described in the Section 3.2.

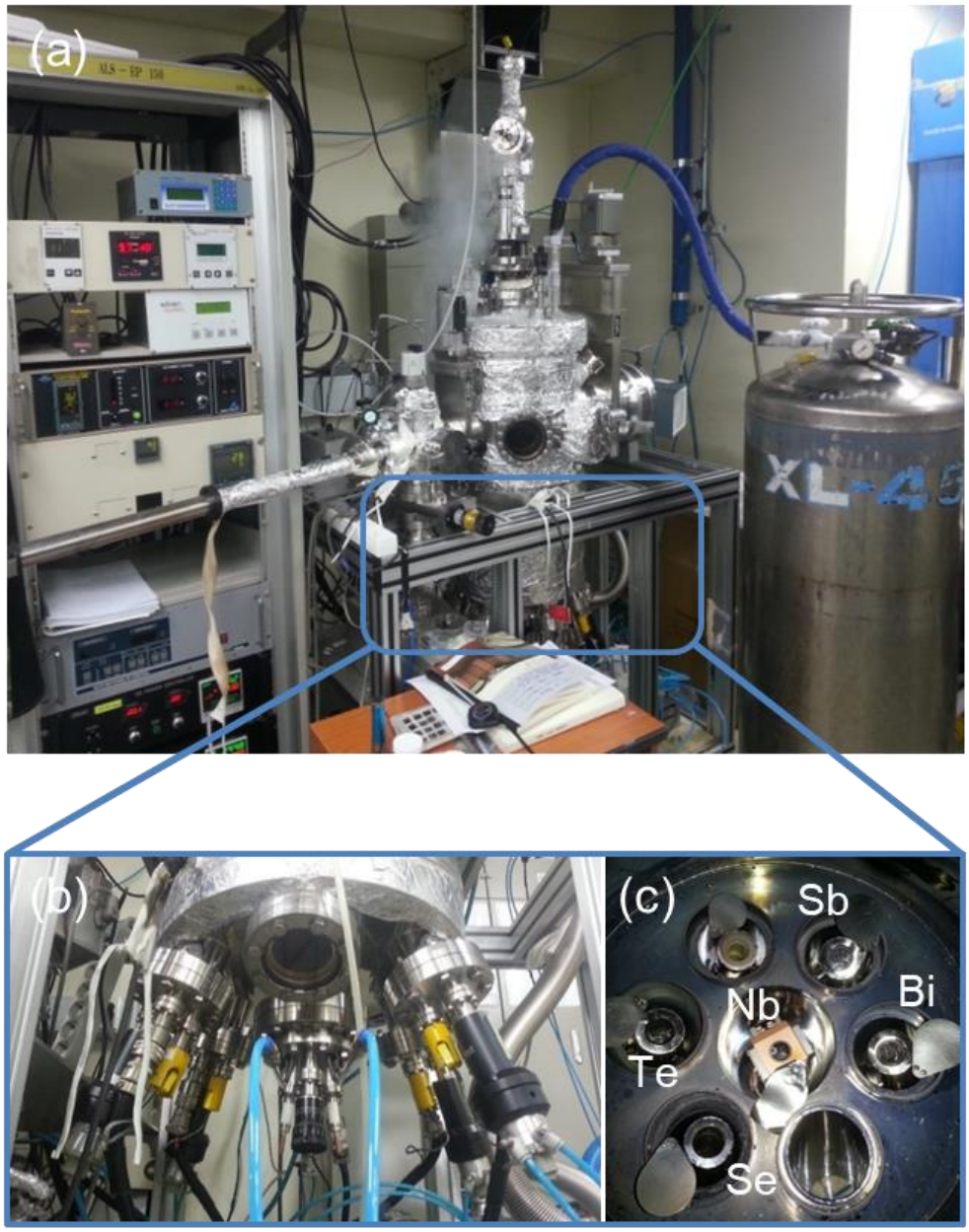

Figure 3.1 (a) MBE used in this research and (b) its main base to which the source cells are attached. (c) Inside view of the main chamber.

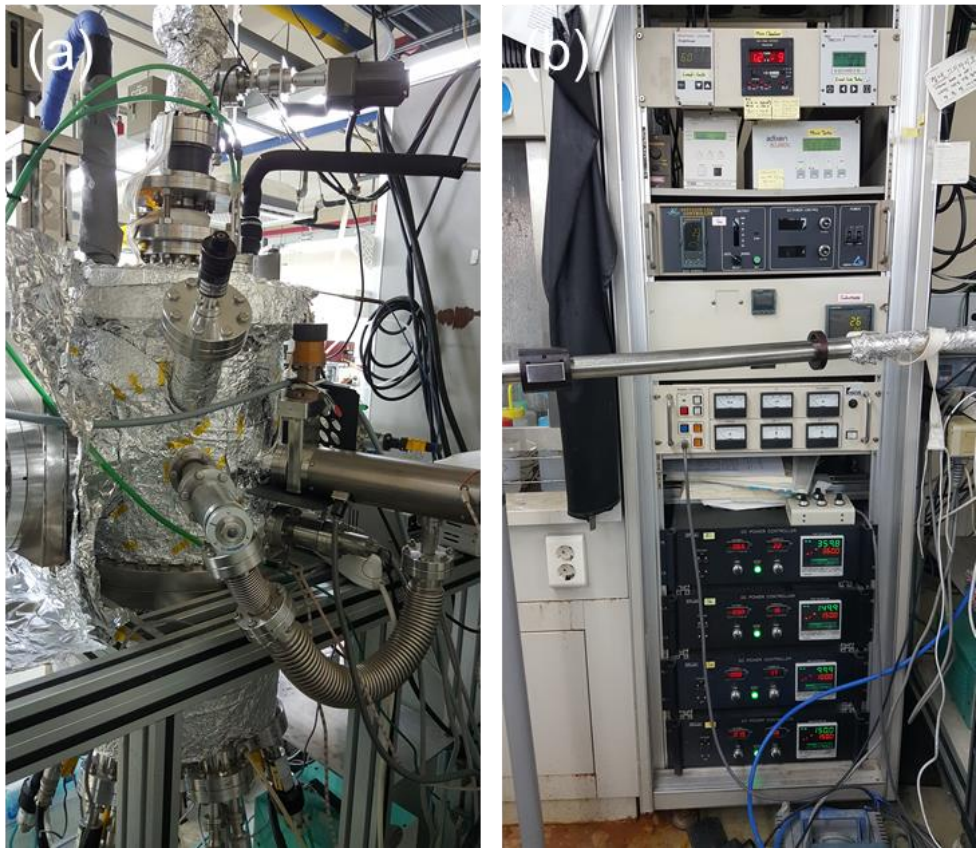

Figure 3.2 (a) Rear view of the MBE system. RHEED gun is on the right side. (b) Control deck of the MBE.

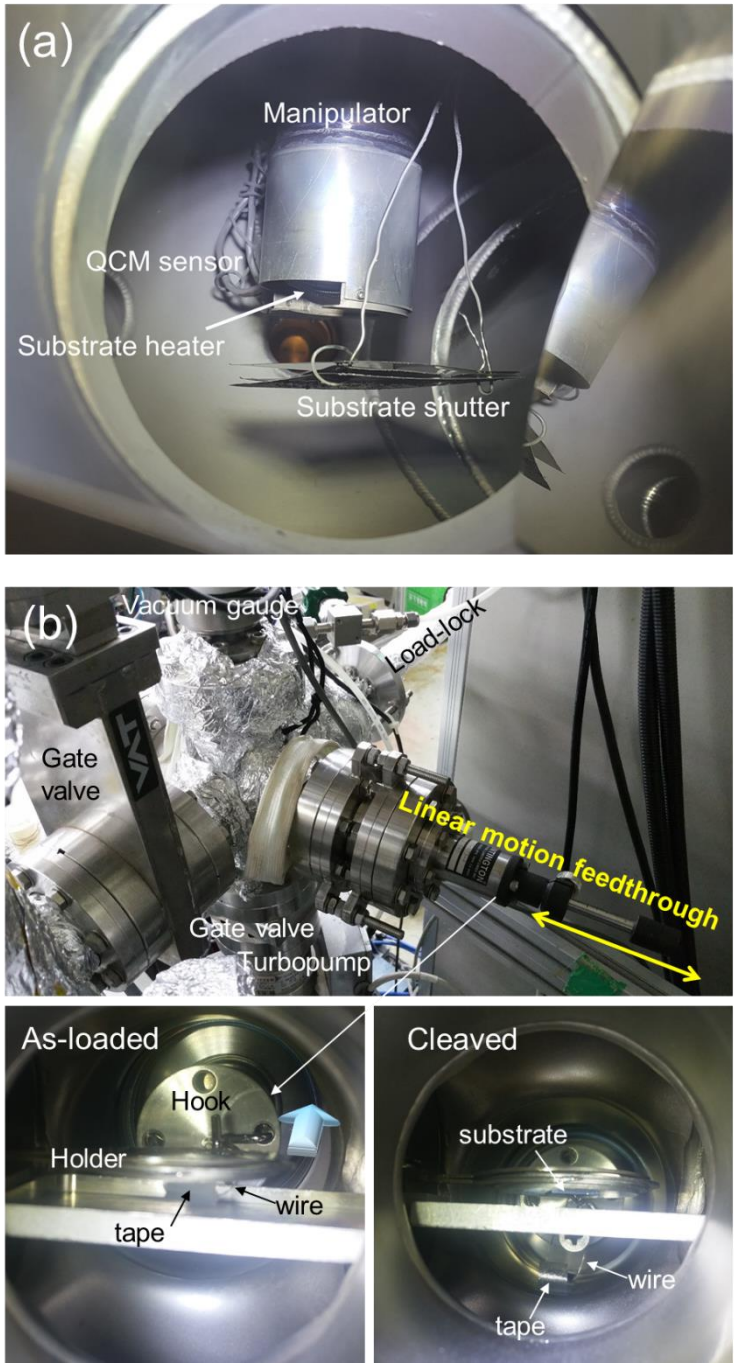

Figure 3.3 (a) Photograph of the substrate manipulator/heater/shutter, and QCM. (b) Photography of load-lock chamber. *In-situ* cleaving mechanism is shown on the bottom panels.

3.1.2 Practice: MBE growth of Bi_2Se_3 thin films on hBN layers

Single crystal flakes of hBN were prepared either on a Si wafer covered with a 285 nm or 300 nm SiO_2 layer by the mechanical exfoliation or on TEM compatible chips by micromanipulation technique (See the next section for detailed process of the latter). Typical lateral size and thickness of hBN crystallites were ~10–50 μm and 10–100 nm, respectively. The substrates were rinsed with acetone and IPA followed by N_2 blow to reduce the tape/polymer residues. Note that ultrasonic cleaning, in acetone and IPA, was carried out only for bare SiO_2/Si substrates before the exfoliation, and sonication after this may result in the flake detachment from the substrate. Subsequently, thermal cleaning of the substrates was carried out at 450^{o}C for 30 min in an UHV prior to the growth. The growth was carried out by supplying Bi and Se fluxes simultaneously. The typical Se/Bi beam flux ratio during the growth was 15–20, measured by the QCM. The growth rate was maintained at 0.2–0.4 QL/min, solely determined by the Bi flux.

To obtain high-quality films with a uniform and smooth surface, we developed a two-step growth method that increases the nucleation sites while preventing texturing of the film. At the first step, 1–2 QLs of Bi_2Se_3 were deposited at a low temperature where the films grow with a high surface coverage ≈100% but with poor crystalline quality. The 1st step growth was terminated by closing the Bi shutter. The samples were then annealed under Se flux while the substrate was slowly heated up (5^{o}C/min) to higher growth

temperature. After the substrate reached the desired temperature, the sample was further annealed for 30 min. Then additional layers were grown on top of them until the desired thickness was achieved. The growth was terminated by closing the Bi shutter, and the sample was naturally cooled under Se flux, which was supplied till the substrate temperature arrived at 200^{o}C (See Figure 3.3 for detailed growth sequences).

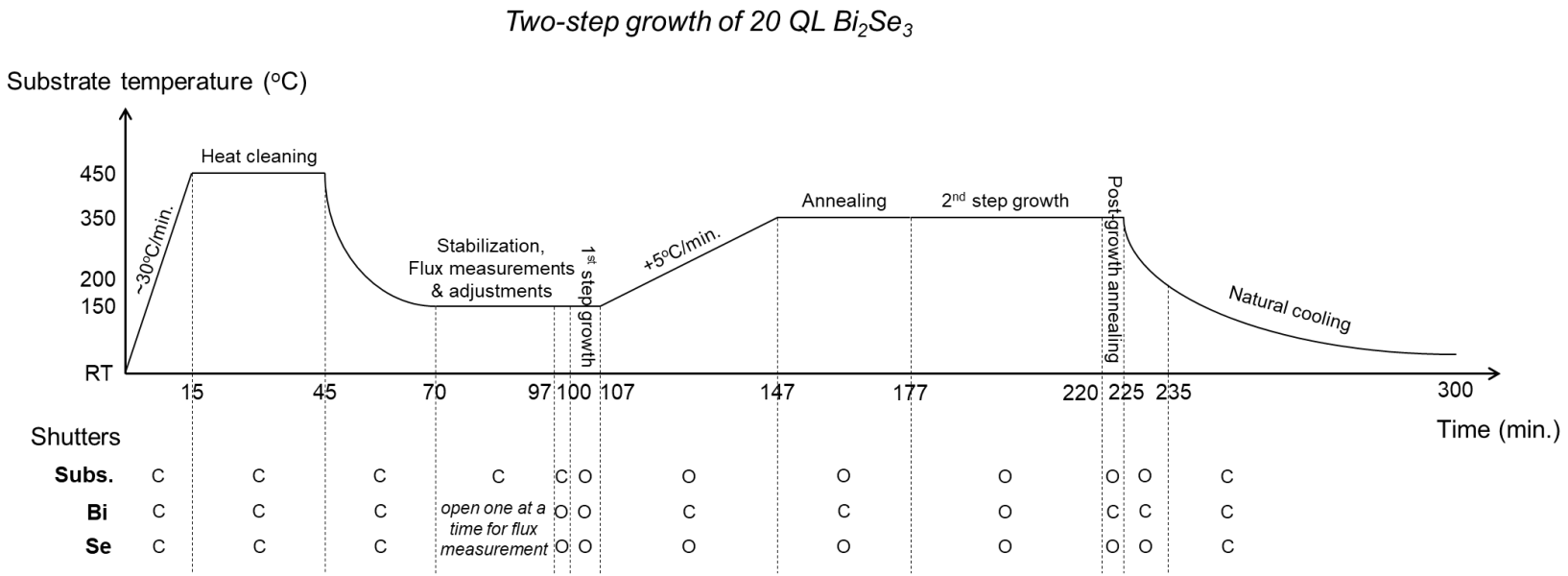

Figure 3.4 Typical growth profile and shutter sequence of two-step growth of 20 QL Bi_2Se_3.

3.2 Preparation of MBE-, TEM-, and Nanofabrication-Compatible Mesoscopic vdW Templates

3.2.1 Fabrication of sub-micrometer hole array patterns in SiN_x membrane window TEM grids

For the preparation of the templates, 4 × 4 arrays of TEM-compatible SiN_x membrane windows were used. The window consists of a 2.1 × 2.1 mm^2, 200 μm thick Si frame which contains a single 0.2 × 0.2 mm^2, 50 nm thick SiN_x membrane (custom-made at Silson, product code: SiRN-14.0-2.1(4x4)-200HR-0.2-50). This particular SiN_x membrane has exceptionally high mechanical strength which can resist against mechanical and O_2 plasma damage during the vdW-transfer process and the subsequent device fabrication processes. The base substrate is a high-resistivity Si(100) wafer which becomes highly insulating at $T < 100$ K and prevents a short circuit in case of dielectric failure that can happen during wire bonding process for transport measurement given the thin SiN_x layer.

Hole arrays and alignment markers for subsequent device fabrications were designed using a computer-aided design program (CAD; I used DraftSight by Dassault Systems). E-beam lithography and subsequent reactive ion etching (RIE) were employed to make an array of holes in the membrane. First, a poly(methyl methacrylate) (PMMA) e-beam resist (PMMA 950k A5, MicroChem) was spun-coated at 1000/4000 rpm for 10/50

s and baked on a hot plate at a temperature of 180^{o}C for 90 s. Then, the e-beam lithography was performed using a field-emission scanning electron microscope (FE-SEM; MIRA3, TESCAN) operating at an acceleration voltage of 30 kV with Nanometer Pattern Generation System (NPGS) software by JC Nabity Lithography Systems. The e-beam exposed resist was then developed in the developer (methyl isobutyl ketone (MIBK)/IPA 1:3, Microchem) for 90 s at 6^{o}C, using a refrigerated water bath, followed by rinsing with IPA and N_2 blow. The cold development resulted in higher e-beam lithography resolution. The SiN_x on the array of hole patterns was etched by RIE process (P80+, Oxford Instruments). Lastly, the PMMA layer was removed by etching with O_2 plasma treatment (Plasma-Prep II, SPI Supplies) and subsequent acetone bath, IPA rinsing, and N_2 blow. Care should be needed in the blowing since the 50-nm-thick SiN_x is fragile. An additional O_2 plasma helped removing PMMA residue on the surface of the membrane and enhanced the adhesion of the vdW layer to the membrane on which the layer will be transferred, as described in the following section. In this way, holes as small as 60 nm in diameter could be prepared, although the regularly reproducible size was ~100 nm. The detailed recipes are described in Table 3.1.

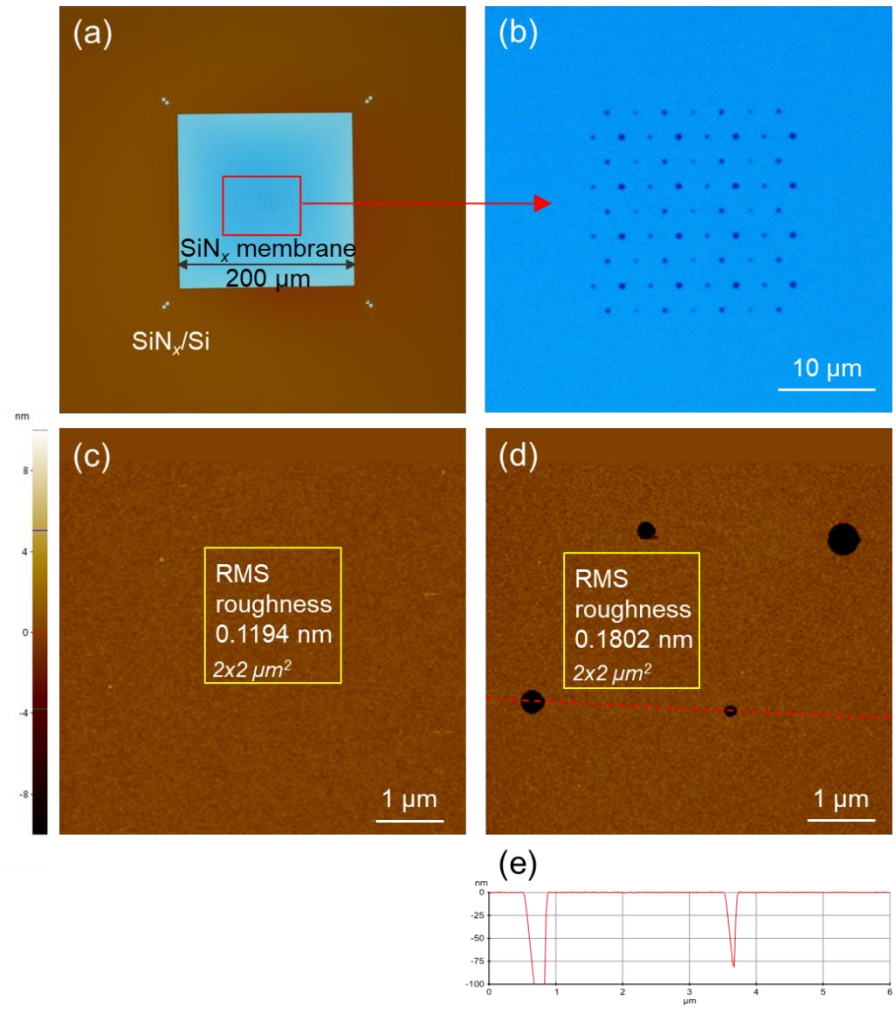

Figure 3.5 (a) Optical microscope image of the hole patterned SiN_x membrane chip. Outside the membrane window, alignment markers are engraved in the four corners for subsequent device fabrication processes. (b) High magnification optical image of the array of holes whose pitch is 3 μm. AFM images of (c) pristine SiN_x membrane and (d) SiN_x membrane after the hole patterning. Root mean square roughness measured on the areas marked by yellow boxes are displayed. (e) AFM Line profile along the red dotted line in (d).

Table 3.1 Typical process conditions for hole patterning of SiN_x membranes

Fabrication steps	Process conditions
1.1 Spin coating of e-beam resist	Top layer: PMMA 950k A5 Spin: 1000/4000 rpm 10/50 s, Baked at 180°C for 90 s
1.2 e-beam lithography of alignment markers	H.V: 30kV, Current: 15–30 pA Magnification: ×800–900, Step size: 3.39–3.81 nm Dose: 700–800 μC/cm^2 (variable)
1.3 Development	MIBK/IPA 1:3 for 90 s, at 6°C
2.1 Reactive ion etching	Oxford P80+ RIE: CF4/Ar 45/5 sccm, 150 W, 50 mtorr 90 s (variable), at room temperature
2.2 PMMA removal	Plasma-Prep II: O_2, 50 W, 100 mtorr, 60 s at room temperature acetone bath at room temperature (optional) Plasma-Prep II: O_2, 50 W, 100 mtorr, 60 s at room temperature

3.2.2 Suspension of few-layer vdW materials on the hole-patterned SiN_x membranes

The process of pick-up and transfer of thin hBN onto the hole patterned SiN_x membrane is shown in Figure 3.6. In this research, transfer of hBN, graphene, and WSe_2 was tried. First, vdW materials in a form of bulk crystals were mechanically exfoliated on a SiO_2/Si substrate. Strong O_2 plasma treatment right before the exfoliation enhances adhesion of vdW layers to the substrate, thereby yielding larger and thinner flakes. Optical microscopy was used to find flakes with desired thickness by the optical contrast. The oxide layer enhances the optical contrast of the vdW materials lying on it due to the interference of visible light transmitting through the thin vdW layers. Few-layer hBN was exfoliated and identified on a Si substrate with 90 nm SiO_2, which offers the greater optical contrast for the thin hBN layers. Their size and surface were also examined together to find a large, clean, and homogeneous flake utilizing both bright field and dark field mode optical microscopy. The thickness and surface morphology of the identified layers was further characterized by AFM. The target layer was then picked up and transferred onto the premade hole in the SiN_x membrane using polycarbonate (PC), polypropylene carbonate (PPC), or polycaprolactone (PCL) on polydimethylsiloxane (PDMS) stamp using a transfer stage consists of an optical microscope, micropositioner, and temperature-controlled sample stage [10]. Here, one of my collaborators, Dr. Young Jae Shin, developed a

novel polymer (PCL) which provides very strong adhesion to the vdW layer and lower working temperatures less than 60^{o}C. Therefore, PCL was particularly useful for the transfer of ultrathin hBN layers and temperature-sensitive vdW materials. Oxygen plasma treatment to SiN_x membrane right before the drop-down enhanced the adhesion between the vdW layer and the membrane, reducing the risk of wash-way of the flake during the subsequent wet process. After the transfer, sticky polymer was removed by organic solvents: anisole or acetone for PCL, chloroform for PC, and Tetrahydrofuran (THF) for PCL. Lastly, the sample was annealed (typically at 350^{o}C) under high vacuum to reduce the polymer residues.

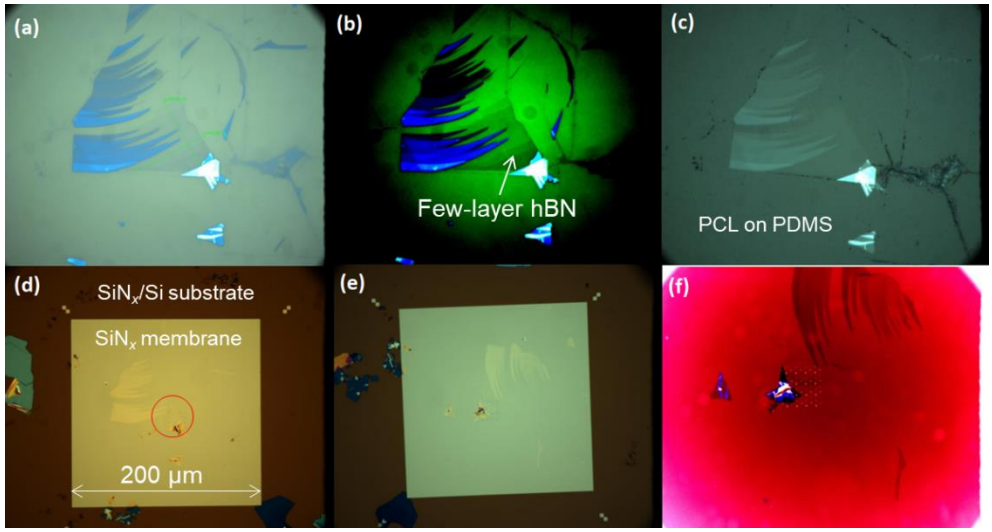

Figure 3.6 (a) Optical image of thin hBN on 90 nm SiO_2/Si. (b) Enhanced optical contrast image of (a). (c) The thin hBN on PCL/PDMS stamp after picking up. (d) The thin hBN transferred on holes in SiN_x (e) After annealing of (d). (f) Enhanced optical contrast image of (e). Pictures courtesy of Dr. Young Jae Shin.

3.3 Morphological and Microstructural Characterizations

The morphological and microstructural characteristics of TI thin films grown on vdW crystallites were investigated using SEM, AFM, and high-resolution TEM (HR-TEM). For SEM observations, low acceleration voltage (2 kV) FE-SEM (AURIGA and SUPRA, Carl Zeiss) was particularly useful for the surface characterizations of the thin van der Waals heterostructures. Non-contact mode topography was typically used for AFM characterizations (NX10, Park Systems, Probe #PPP-NCHR). Field-emission TEMs with the acceleration voltage of 200 kV (JEOL JEM-2100F and FEI Tecnai F20) were used for selected area electron diffraction (SAED), bright field (BF) imaging, and high-resolution (HR) imaging. Elemental mapping was performed with a silicon drift detector-based energy dispersive X-ray spectroscopy (EDS) system, equipped in JEM-2100F operating in the STEM mode, together with AZTEC software (Oxford Instruments, UK). Ball-and-stick model of crystal structures was visualized using VESTA software [48].

Samples for cross-sectional TEM imaging were prepared by a focused ion beam milling (FIB; Helios 650, FEI) and low-energy focused Ar ion milling (NanoMill 1040, Fischione) installed at the National Center for Inter-university Research Facilities (NCRIF) at Seoul National University. For plan-view TEM observations, TI films were directly grown on vdW layers which were transferred on a SiN_x membrane window TEM grid or a holey carbon TEM grid. Then, TEM observation was performed without any

further time-consuming and destructive TEM sample preparation such as thinning, thanks to high mechanical strength and electron beam transparency of the vdW materials. The preparation of the vdW layer on SiN_x membrane windows is described in Section 3.2 while polymer-assisted transfer using PMMA and poly(vinyl alcohol) (PVA) was employed to prepare vdW layers on holey carbon TEM grids [49,50]. On the other hand, post-growth transfer of the vdW heterostructures from a SiO_2/Si substrate to the TEM grid could also be readily carried out by wet chemical etching of the SiO_2 sacrificial layer with the aid of a PMMA support layer, which is very similar to the well-established PMMA-assisted wet transfer method of CVD graphene grown on Cu foils except that here the underlying SiO_2 was etched by buffered oxide etch (BOE). In this case, however, the sample undergoes heating and is exposed to reactive chemicals and to air for a long time. Also, the PMMA residues on the sample surface may hinder high-resolution observations.

3.4 Device Fabrications for Electrical Characterizations

3.4.1 Hall bar and van der Pauw geometry devices

TI thin films grown on vdW single crystals were fabricated into either Hall bar or van der Pauw devices for lateral electrical transport measurements. The detailed recipes are described in Table 3.2, and optical images of in-line products are displayed in Figure 3.7. The films grown on mechanically

exfoliated vdW layers on Si chips with 285 nm or 300 nm thick SiO_2 layer were normally used where the heavily doped bulk Si can be used as a global back gate. In addition, the oxide layer enhances the optical contrast of the vdW materials lying on it because of the interference of visible light transmitting through the thin vdW layers, providing good tool for examining the surface of the exfoliated flakes and the TI films grown on top of them.

It should be noted that after the MBE growth, the whole area of SiO_2/Si substrates are covered by TI thin films, which are weakly adhered on the substrate by van der Waals interaction. It is found that large metal pads deposited on them indeed easily peels off from the substrate during the wire bonding process. Therefore, the sample should be etched into Hall bar or van der Pauw geometries before the deposition of bonding pads, removing TI films on the unwanted area of the substrate. One the other hand, it is desirable to minimize polymer coating processes before the deposition of metal contacts to achieve lower contact resistances. Therefore, the device fabrication process is composed of 4 rounds of e-beam lithography, 3 rounds of metal deposition, and one round of etching as follows.

The device fabrication process starts from putting down alignment markers for the identification of the target TI/vdW heterostructure flakes and calculation of their positions on the substrate. After TI film growth and unloading the samples from the MBE chamber, PMMA/copolymer bilayer e-beam resists (PMMA 950k A5 on MMA(8.5)MAA EL9, MicroChem) were

spun-coated at 1000/4000 rpm for 10/50 s, for each layer. Here, the copolymer forms undercut for easier lift-off of metal films. The spin-coating process was performed as soon as possible to minimize the surface oxidation of TI thin films, and each resist was baked at a relatively low temperature of 90^{o}C for a short time (60 s) to prevent possible degradation of the TI material. From here, the PMMA/copolymer layer protects the TI surfaces from the air. Arrays of alignment marker patterns were written by standard e-beam lithography, and the e-beam exposed resist was developed in MIBK/IPA 1:3 developer for 90 s at room temperature, followed by IPA rinsing and N_2 blow. Then, 10/30 nm of Cr/Au was deposited by e-beam evaporation. The thin layer of Cr (or Ti) under Au enhances the adhesion of metals. After the metal deposition, the sample was dipped in acetone at room temperature for the lift-off of metal films covering the non-exposed e-beam resist. Covering wafer edges with metal foils before the evaporation or cutting off edge beads after the evaporation, together with a gentle shaking of the sample in acetone, helped easier and faster lift-off. Flowing acetone over the sample using a squeeze bottle also assists this process, but ultrasonic treatment may result in the flake detachment from the substrate.

After the lift-off, IPA rinsing, and N_2 blow, the sample was spun-coated again with the PMMA/copolymer in the same manner. Then it was examined under an optical microscope. TI/vdW heterostructure flakes with clean and homogeneous surfaces could be identified by optical contrast in

bright field images. It was also found that the e-beam resist layer enhances the optical contrast. Tape residues and bubbles could be avoided as they are clearly visible under the dark field mode. The position of the target flake on the chip was calculated relative to alignment markers or features such as corners of adjacent flakes.

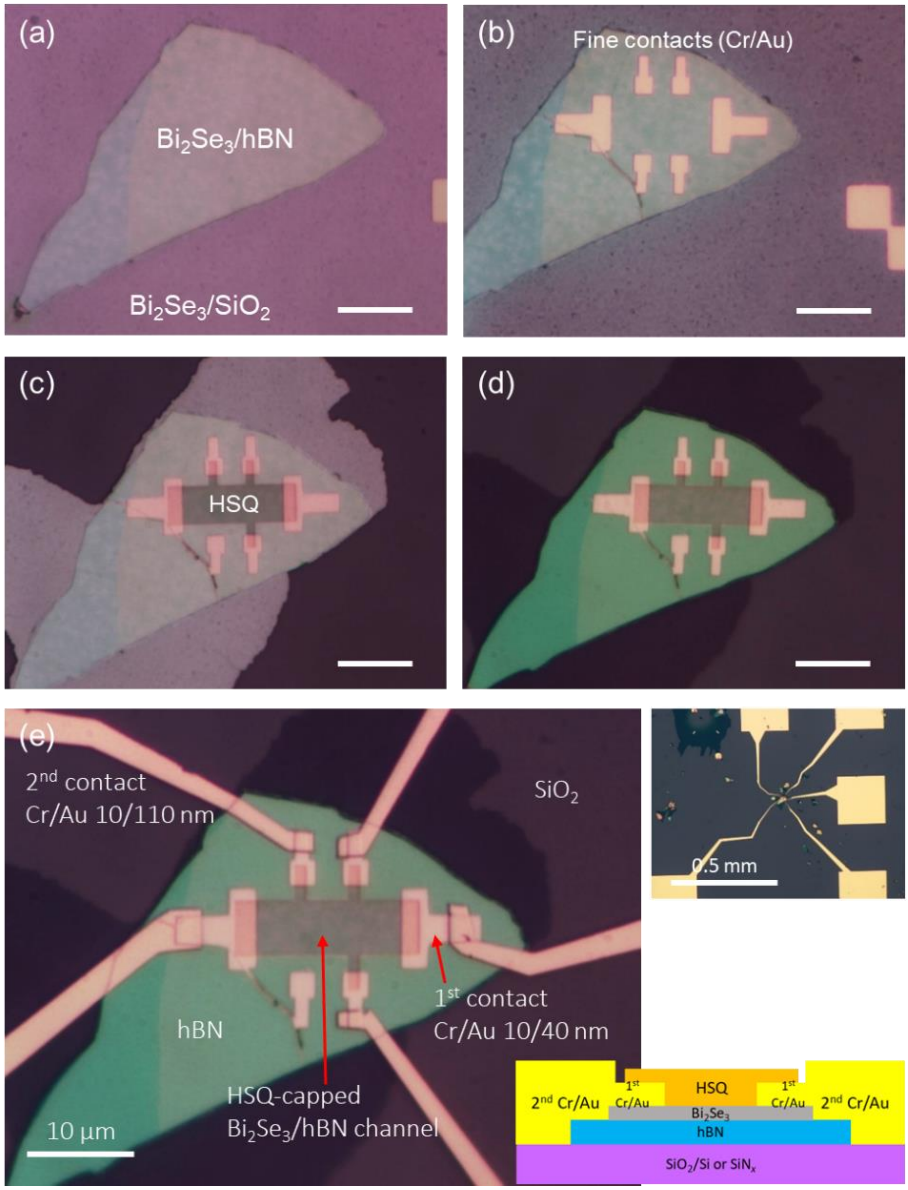

Figure 3.7 Optical images of 10 QL Bi_2Se_3/hBN on a SiO_2/Si substrate taken after each step of the Hall bar device fabrication: (a) Putting down small contacts, (b) Putting down fine contacts, (c) Writing Hall bar etch mask, (d) Ar plasma etch, (e) Putting down bonding pads and connecting with the 1st contacts.

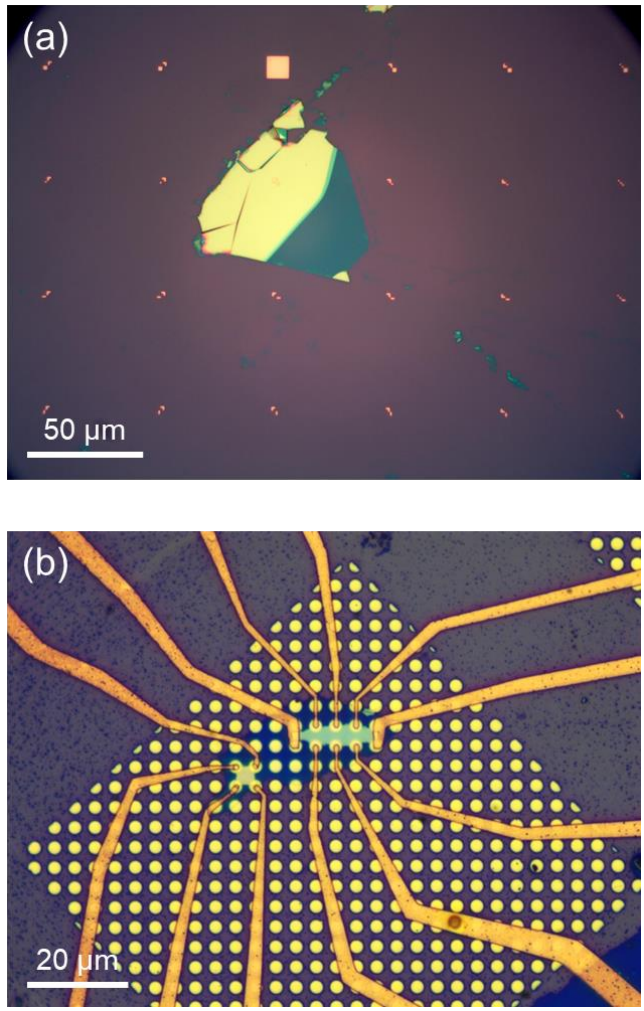

Figure 3.8 (a) Optical image of exfoliated hBN flake on pre-made alignment marker arrays on a 285 nm SiO_2/Si substrate. (b) Optical image of the Hall bar and the van der Pau geometry devices which utilize the metal microdot arrays deposited by the polymer-free stencil mask method as ohmic contacts as well as alignment markers.

The deposition of alignment markers on the substrate could be carried out before the exfoliation of vdW crystals (Figure 3.8(a)). It could even be omitted if the density of the exfoliated crystallites is dense enough so that the coordinates of the target flake relative to the corners of adjacent flakes can be precisely measured. In both cases, we can expect a cleaner TI–metal contact interface as we can avoid one round of polymer coating before the contact deposition, reducing the amount of e-beam resist residues on the contact area. Alternatively, an array of Cr/Au microdots can be deposited through stencil masks such as Quantifoil holey carbon grids for the resist-free formation of alignment markers. In this case, the deposited metal microdots can also be used for ohmic contacts to the TI films (Figure 3.8(b)).

The next step is defining device geometries and deposition of metal contacts. First, a set of micro-scale ohmic contacts were formed by similar e-beam lithography and e-beam evaporation processes described above. Here, I shook the sample vigorously in the developer to minimize possible residue of the e-beam resist on the TI surface. The sample was loaded in the evaporator right after the development to minimize the time exposed to air. Metal contacts composed of Cr/Au 5–10/40–50 nm were typically deposited with a deposition rate of 0.5–1.0 Å/s under high vacuum environment of low 10^{-8} torr, forming good ohmic contacts with TIs down to cryogenic temperatures. After lift-off of the 1st contacts, hydrogen silsesquioxane (HSQ; XR-1541, Dow) was spun coated at 5000 rpm for 60 s. The HSQ layer served

as both a negative tone e-beam resist and an etch mask, and the third e-beam lithography was followed to pattern the HSQ layer into a Hall bar or van der Pauw geometry. As HSQ has a relatively short shelf life and is sensitive to storage conditions, e-beam dose tests and development time tests were normally performed on a dummy substrate before writing the patterns on the sample. After e-beam lithography, the HSQ layer was developed in AZ 300 MIF (metal ion free) developer (2.38 wt % tetramethylammonium hydroxide (TMAH) in water) for 6 min, followed by rinsing in deionized (DI) and drying by N_2 blow. During this development process, some parts of Bi_2Se_3 grown on SiO_2 area peeled off as displayed in Figure 3.8 (c). Then the films were etched by Ar plasma (using either P80+ RIE system or Plasma-Prep II system). The e-beam exposed HSQ was intentionally remained after here, serving as a capping layer. If necessary, a sacrificial PMMA layer can be spun coated beneath the HSQ, which can be removed together by acetone after etching. The final round of e-beam lithography and a subsequent e-beam evaporation of Cr/Au 10/110 nm or Cr/Pd/Au 5/20/125 nm were used to put down contact pads and to connect them with the 1^{st} contacts.

A back gate was formed by scratching the bottom SiO_2 layer of the sample with a diamond scriber and attaching the sample using a cryogenic conductive epoxy (H20E, Epo-Tek) to a chip carrier with a bottom metal pad.

Table 3.2 Typical process conditions for the fabrication of Hall bar and van der Pauw geometry devices

Fabrication steps	Process conditions
1.1 Spin coating of e-beam resist	Bottom layer: MMA(8.5)MAA EL9 Spin: 1000/4000 rpm 10/50 s, Baked at 90°C for 60 s Top layer: PMMA 950k A5 Spin: 1000/4000 rpm 10/50 s, Baked at 90°C for 60 s
1.2 e-beam lithography of alignment markers	H.V: 30kV, Current: 600 pA Magnification: ×150, Step size: 20.35 nm Dose: 425 μC/cm^2
1.3 Development	MIBK/IPA 1:3 for 90 s, at room temperature
2.1 Alignment marker metallization	e-beam evaporator Cr/Au 10/30 nm
2.2 Lift-off	in acetone bath at room temperature
3.1 Spin coating of e-beam resist	Bottom layer: MMA(8.5)MAA EL9 Spin: 1000/4000 rpm 10/50 s, Baked at 90°C for 60 s Top layer: PMMA 950k A5 Spin: 1000/4000 rpm 10/50 s, Baked at 90°C for 60 s
3.2 e-beam lithography of 1st contacts	H.V: 30kV, Current: 20 pA Magnification: ×800, Step size: 3.81 nm Dose: 425 μC/cm^2
3.3 Development	MIBK/IPA 1:3 for 90 s, at room temperature
4.1 1st contact metallization	e-beam evaporator Cr/Au 10/40 nm
4.2 Lift-off	in acetone bath at room temperature
5.1 Spin coating of e-beam resist	HSQ (XR-1541-006) Spin: 1000/5000 rpm 10/50 s, No baking
5.2 Negative-tone e-beam lithography of Hall bar etch masks	H.V: 30kV, Current: 20 pA Magnification: ×800–900, Step size: 3.81 nm Dose: 225 μC/cm^2 (variable. Need to do dose test every time)
5.3 Development	AZ 300 MIF for 6 m (variable), at room temperature * Rinse with DI water for negative tone development
6 Plasma etching	Oxford P80+ RIE: Ar 50 sccm, 80 W, 100 mtorr 90 s at room temperature, (or Plasma-Prep II) : Ar, 80 W, 100 mtorr, 120 s at room temperature

7.1 Spin coating of e-beam resist	Bottom layer: MMA(8.5)MAA EL9 Spin: 1000/4000 rpm 10/50 s, Baked at 90°C for 60 s Top layer: PMMA 950k A5 Spin: 1000/4000 rpm 10/50 s, Baked at 90°C for 60 s
7.2 e-beam lithography of 2nd contacts	Interconnection lines: H.V: 30kV, Current: 20–50 pA Magnification: ×800, Step size: 3–15 nm Dose: 425 μC/cm^2 Bonding pads: H.V: 30kV, Current: 1.5–2.5 nA Magnification: ×150, Step size: 40.69 or 61.04 nm Dose: 425 μC/cm^2
7.3 Development	MIBK/IPA 1:3 for 90 s, at room temperature
8.1 2nd top contact metallization	e-beam evaporator Cr/Au 10/120 nm or Ti/Pd/Au 5/20/125 nm
8.2 Lift-off	in acetone bath & squeezing at room temperature

3.4.2 Tunneling devices based on suspended double-side vdW heterostructures

Electrical contacts on both sides of suspended TI/hBN/TI heterostructures, prepared on SiN_x membrane chips, were fabricated by following steps for tunneling measurements. First, Ti/Au 5/200 nm was deposited on the whole area of the bottom side of the sample by e-beam evaporation. This thick metal layer not only overcomes the step height of holes made in the SiN_x membrane but also provides mechanical strength to the membrane for the following fabrication steps. Top contacts were fabricated by the processes similar to those for lateral devices. Etched holes and trenches formed during the hole-patterning of the SiN_x membrane were used as alignment markers. Fine contacts to the individual junctions were deposited by e-beam lithography followed by e-beam evaporation of Ti/Au 5/55 nm. Using the metal contact as a etch mask, Ar plasma etching was carried out to remove the TI films on the uncovered area. Finally, bonding pads and interconnection lines to the 1^{st} contacts were deposited by another round of e-beam lithography and e-beam evaporation of Ti/Pd/Au 5/20/125 nm. The fabricated devices are in two-probe geometry composed of individually contacted top probes and a common bottom probe. The detailed recipes are described in Table 3.3, and optical images of in-line products are displayed in Figure 3.9. Note that sonication should never be used in any case during the fabrication since it will immediately break the SiN_x membrane.

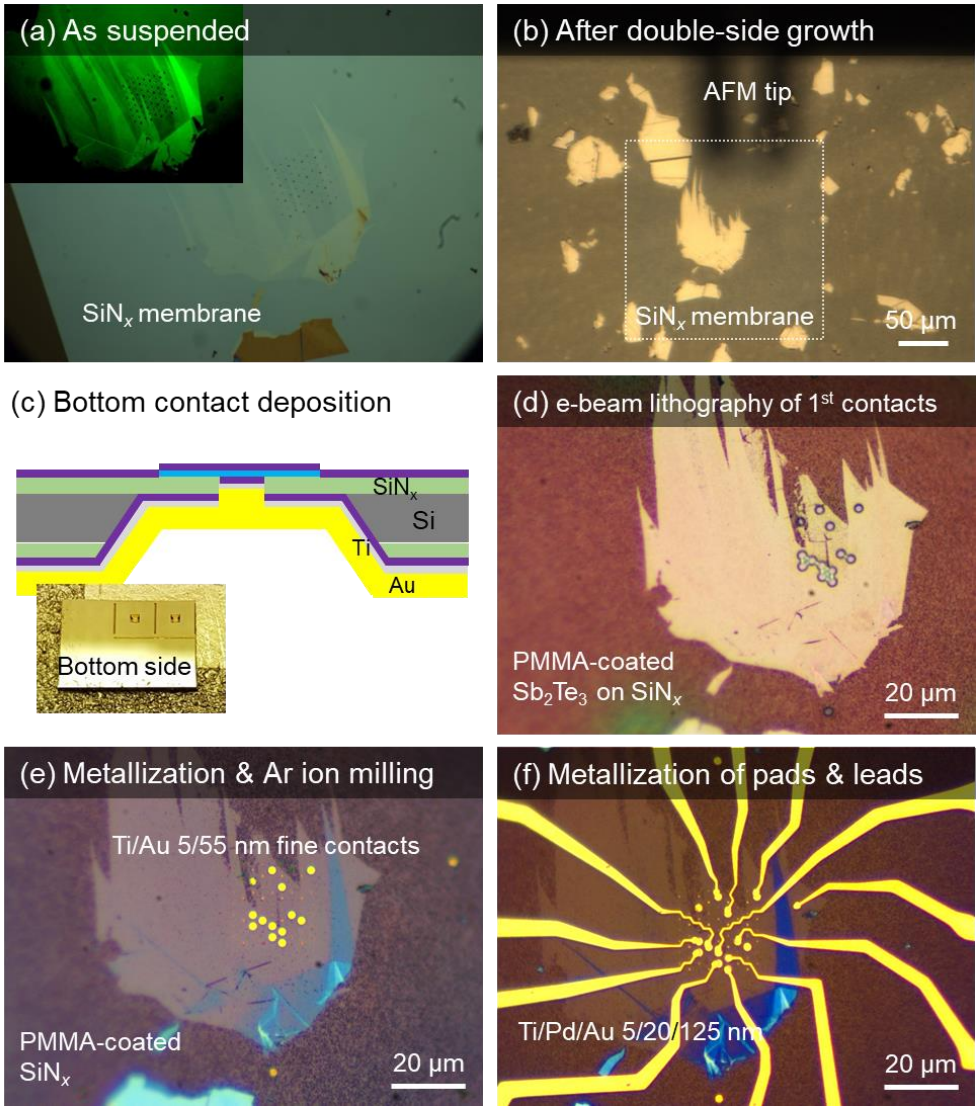

Figure 3.9 Optical images of Sb_2Te_3/hBN/Bi_2Se_3 on a SiN_x membrane chip taken after each step of tunneling device fabrication.

Table 3.3 Typical process conditions for fabrication of tunneling devices

Fabrication steps	Process conditions
1 Bottom contact metallization	e-beam evaporator Ti/Au 5/200 nm
2.1 Spin coating of e-beam resist	Bottom layer: MMA(8.5)MAA EL9 Spin: 1000/4000 rpm 10/50 s, Baked at 90°C for 60 s Top layer: PMMA 950k A5 Spin: 1000/4000 rpm 10/50 s, Baked at 90°C for 60 s
2.2 e-beam lithography of 1st top contacts	H.V: 30kV, Current: 20–40 pA Magnification: ×800, Step size: 3.81 nm Dose: 425 μC/cm^2
2.3 Development	MIBK/IPA 1:3 for 90 s, at room temperature
3.1 1st top contact metallization	e-beam evaporator Ti/Au 5/55 nm
3.2 Lift-off	in acetone bath at room temperature
4 Plasma etching	Oxford P80+ RIE Ar 50 sccm, 80 W, 100 mtorr 90 s at room temperature
5.1 Spin coating of e-beam resist	Bottom layer: MMA(8.5)MAA EL9 Spin: 1000/4000 rpm 10/50 s, Baked at 90°C for 60 s Top layer: PMMA 950k A5 Spin: 1000/4000 rpm 10/50 s, Baked at 90°C for 60 s
5.2 e-beam lithography of 2nd top contacts	Interconnection lines: H.V: 30kV, Current: 20–40 pA Magnification: ×800, Step size: 3.81 nm Dose: 425 μC/cm^2 Bonding pads: H.V: 30kV, Current: 1.5–2.5 nA Magnification: ×150, Step size: 40.69 or 61.04 nm Dose: 425 μC/cm^2
5.3 Development	MIBK/IPA 1:3 for 90 s, at room temperature
6.1 2nd top contact metallization	e-beam evaporator Ti/Pd/Au 5/20/125 nm
6.2 Lift-off	in acetone bath & squeezing at room temperature

3.5 Electronic Transport Measurements

3.5.1 Lateral magnetotransport measurements

The magnetotransport measurements were carried out in a Physical Property Measurement System (PPMS; 1.8K 14T spec, Quantum Design) with low-frequency AC lock-in technique with an excitation current of 100 or 500 nA. Two lock-in amplifiers (SR830, Stanford Research Systems) were used for the 4-probe longitudinal and Hall resistivity measurements. A 10 MΩ resistor was connected in series between the output channel of one of the amplifiers and the source contact of the Hall bar. It provides a good approximation of current-driving mode, i.e. I = 500 nA when the output voltage is 5 V, since typical two-probe source-drain resistance was a few kΩ for the devices investigated in this dissertation. The voltage differences of voltage probes were measured through the lock-in differential inputs, and the measuring frequencies were locked to the excitation frequency, which was ~13–47 Hz. Th integration time was 300 ms or 1 s. A gate voltage was applied using a DC voltage source (Model 2400 SourceMeter, Keithley Instruments). The measurement was controlled by a MATLAB program. Longitudinal (Hall) resistances were symmetrized (anti-symmetrized) for the data analysis. The temperature and magnetic field were controlled by the PPMS. Typical field sweep rate was 100 G/s. Field angle dependent measurements were performed using a horizontal rotator probe which can control the angle between the sample and the magnetic field using an external motor.

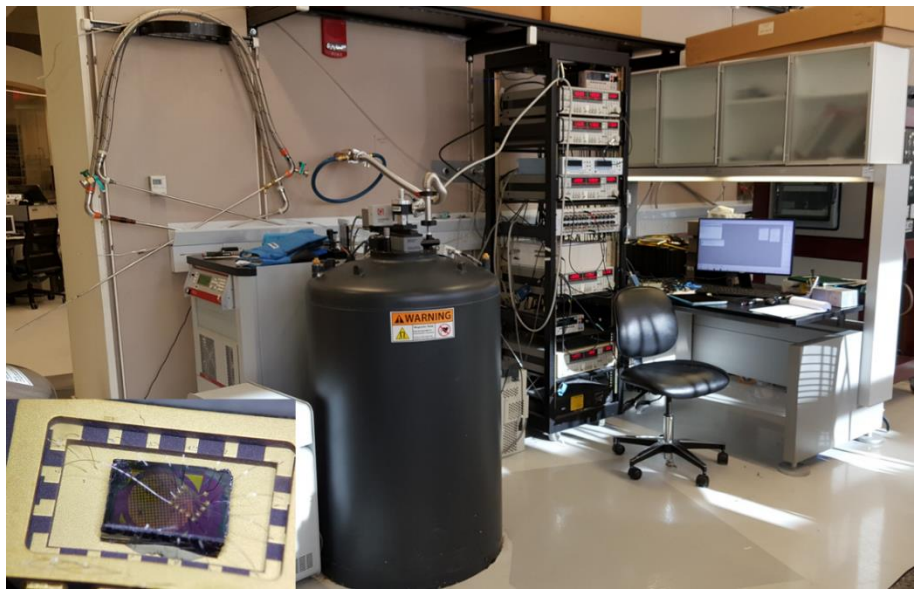

Figure 3.10 Quantum design PPMS and measurement system in Prof. Philip Kim's lab at Harvard University used for lateral magnetotransport measurements. Left bottom: A Hall bar device wire-bonded on a chip carrier.

3.5.2 Magneto-tunneling measurements

The current–voltage characteristics of the tunneling devices were measured using a voltage source (Model 2400 SourceMeter, Keithley Instruments) for applying DC bias voltage and a current amplifier (Model 1211, DL Instruments) connected with another Keithley 2400 operated in a voltage sensing mode for measuring current. The differential conductance was either obtained by numerical differentiation of the current–voltage curve or measured by mixing small AC excitation voltage of 2 mV with the DC bias voltage using a lock-in amplifier (Model 7265, Signal Recovery), transformer and voltage divider. The temperature and magnetic field were controlled by a ^{4}He cryostat with variable temperature insert and superconducting magnet (Teslatron PT, Oxford Instruments). The sample was cooled down to 1.5 K and the maximum magnetic field was 8 T. The magnetic field could be applied either parallel or perpendicular to the sample by changing the orientation of sample *ex-situ*.

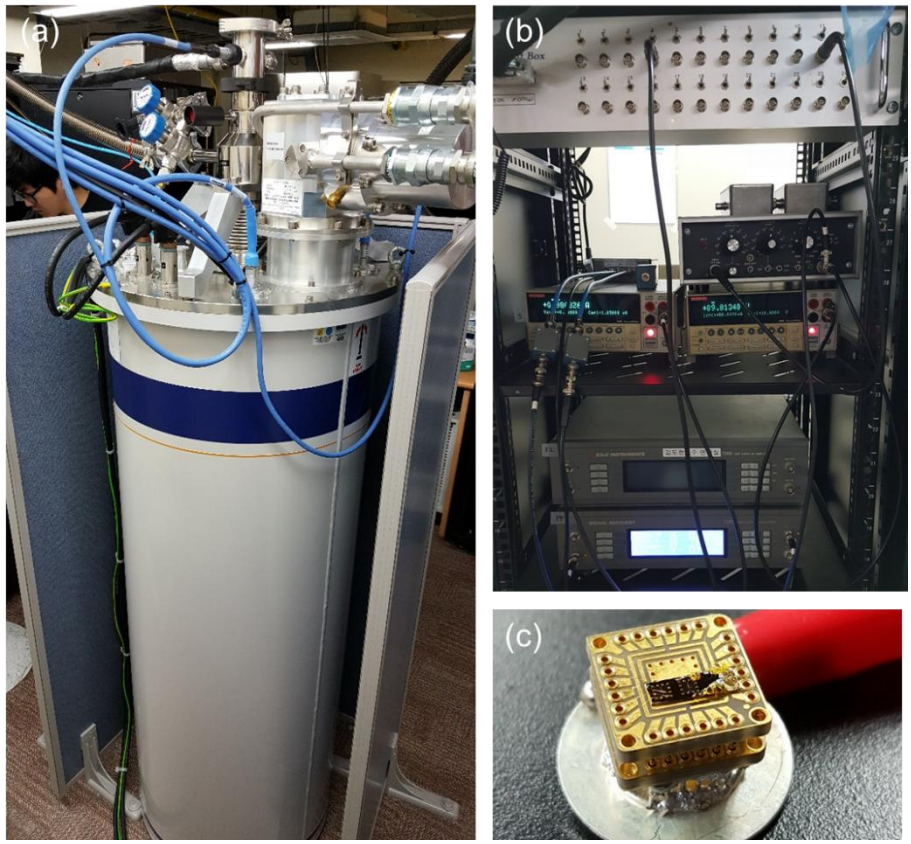

Figure 3.11 (a) Oxford Teslatron PT and (b) measurement system in Prof. Dohun Kim's lab at Seoul National University used for magneto-tunneling measurements of TI/hBN/TI heterostructures. (c) Photograph of the sample in the out-of-plane field configuration.

4 MBE Growth of Bi_2Se_3 Thin Films on hBN and Their Structural and Electronic Transport Properties

4.1 Introduction

Topological insulators are bulk-insulating materials with topologically protected Dirac surface states in the bandgap [13]. Bi_2Se_3 is one of the most popular 3D TIs, attracting an intense attention owing to the TSSs, located deep in a relatively large bulk bandgap energy (~0.3 eV), thus well-separated from the bulk conducting states [15,23,51]. However, while there have been experimental reports to produce high-quality bulk single crystals of Bi_2Se_3, where the TSS transport has been observed [52,53], it has been technically challenging to synthesize a highly crystalline Bi_2Se_3 thin film. For the demonstration of controlled device fabrication utilizing TI transport characteristics, it is necessary to obtain high mobility TI thin films with a reduced concentration of defects [17]. For the synthesis of high-quality, large domain single crystalline thin films, it is highly desirable that the TI films grows epitaxially on a single crystal substrate with a compatible lattice structure [54]. However, a weak vdW nature of the interlayer interaction of Bi_2Se_3 poses challenge for the choice of the substrate that can be compatible with the vdW epitaxy between the grown film and the substrate. A

particularly promising choice of the substrate for the epitaxial growth of Bi_2Se_3 thin films is hBN, which has the same 2D vdW layered structure and hexagonal lattice symmetry as Bi_2Se_3 [16,55]. Ideally, the absence of dangling bonds in the vdW interface can reduce the defect concentrations in the TSS formed on Bi_2Se_3 thin films. Moreover, being a dielectric insulator with chemically inert surfaces, hBN is well suited for electronic transport studies of vdW thin films grown on the top [33-35]. Here we report the molecular beam epitaxial growth of high-quality Bi_2Se_3 thin films on an hBN substrate and their atomic structural and electrical transport properties. The grown films exhibited the Dirac nature of the high mobility TSS at the Bi_2Se_3/hBN interface as proved by observation of Shubnikov-de Haas (SdH) oscillations.

4.2 MBE Growth of Bi_2Se_3 Thin Films on hBN Layers

High-quality, atomically smooth, and uniform Bi_2Se_3 thin films with low defect concentrations were grown on hBN layers using an UHV-MBE system. The hBN substrates were prepared on SiO_2/Si chips by mechanical exfoliation of hBN single crystals. High purity Bi (99.999%) and Se (99.9999%) sources were used for the film growth while the background pressure of the growth chamber was maintained at middle 10^{-10} to low 10^{-9} Torr. The MBE also enabled us to control and monitor the growth temperature and beam fluxes precisely, allowing for a comprehensive control of growth

modes, thicknesses, and compositions of the growing film. Growth temperatures of 410–675 K, measured by a thermocouple behind the substrate holder, were studied. The film growth was carried out under Se-rich conditions, and the typical film thickness was 6–10 quintuple layers (QLs; 0.95 nm) (see Section 3.1.2 for details).

After the initial growth by the MBE, we investigated the surface morphology of the films to study the growth behaviour of Bi_2Se_3 on hBN layers. Figures 1(a)–(c) show SEM images of Bi_2Se_3 thin films grown at various growth temperatures of 490, 550, and 610 K, respectively. The contrast change in the SEM images reveals domains and terrace structures. With increasing growth temperature, domain sizes were increased from several hundreds of nanometres (Figure 4.1(a)) to larger than 1 μm (Figure 4.1(c)). In addition, the image contrast of a single domain gets weaker, and the density of island structures appeared in white spots decreases drastically. These results strongly suggest that the film grown at a higher temperature has larger terraces and a smoother surface. However, increasing the temperature above 550 K resulted in a dramatic decrease in the surface coverage, exposing bare hBN surfaces seen as brighter areas in Figures 1(b) and (c), which makes it difficult to obtain uniform thin films.

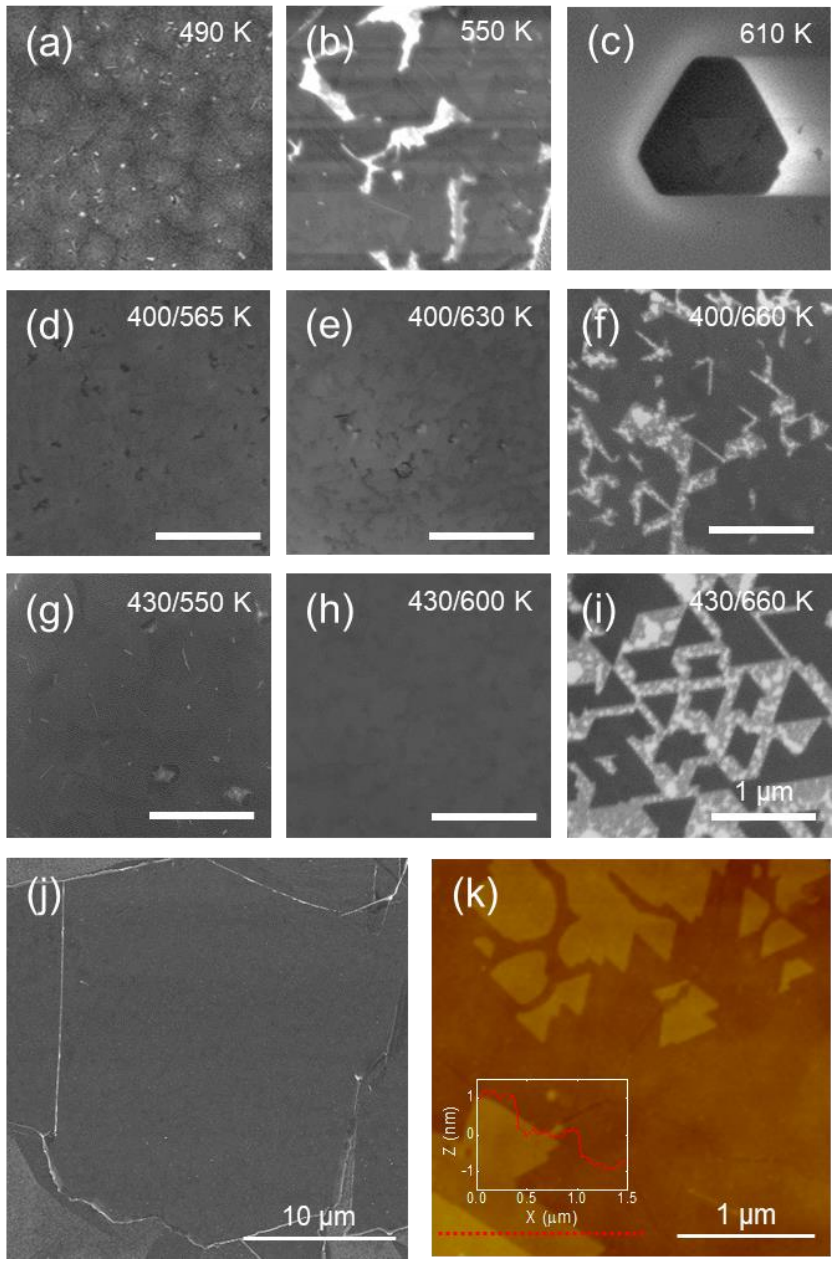

Figure 4.1 Surface morphology of MBE-grown Bi_2Se_3 thin films on hBN layers. (a)–(c) SEM images of single-step grown films at different growth temperatures of 490, 550, and 610 K, respectively. (d)–(i) SEM images of two-step grown films with 1st 2 QL deposition at a lower temperature followed by annealing and 2nd step growth at a higher temperature. (g) SEM and (h) AFM image of an 8 QL Bi_2Se_3 thin film grown by the optimized two-step method. The inset in (h) shows the AFM line profile obtained across the red dotted line in the main figure.

To obtain high-quality films with a uniform and smooth surface, we developed a two-step growth method that increases the nucleation sites while preventing texturing of the film. At the first step, 1–2 QLs of Bi_2Se_3 were deposited at a low temperature where the films grow with a high surface coverage ≈100% but with a poor crystalline quality. The samples were then annealed under Se flux for 1 hour while the substrate was slowly heated up to a higher growth temperature. Additional layers were grown on top of them at the higher temperature until the desired thickness was achieved. Figures 1(d)–(i) show the surface morphologies of the films grown at different 1st and 2nd step growth temperatures. The 1st step growth temperature was chosen to be 430 K since the films nucleated at temperatures lower than 430 K had island structures remaining even after the high temperature annealing while a 1st step temperature of 430 K resulted in 100% coverage without residual island structures after a sufficient annealing. Meanwhile, higher temperatures (up to 630 K) in the 2nd step process yielded a uniform and flat surface morphology of the films as shown in Figures 1(h) and (j). At even higher temperatures above 630 K, however, the surface coverage decreased regardless of the 1st step temperature, presumably due to the re-evaporation of the Bi_2Se_3 films (Figures 1(f) and (i)). Based on these results, the optimal 1st and the 2nd step temperatures are 430 K and 600–630 K, respectively.

The surface morphologies of the two-step grown high-quality films were further investigated using AFM, providing atomic scale information of

the film surface. Figure 4.1(k) shows a representative AFM image of 8 QL Bi_2Se_3 thin films grown on hBN layers using the two-step method. The AFM image revealed that the films are composed of smooth terraces over a large area (> 1 μm) with reduced island structures, and the step height of ~1 nm consistent with the thickness of 1 QL of Bi_2Se_3. Accordingly, the two-step grown films exhibited a desirable growth behaviour that can provide an atomically smooth film. The AFM image in Figure 1(k) also shows that the as-grown crystal faces in each domain are preferentially aligned with each other, suggesting the existence of an epitaxial relationship [56-60] on the single crystalline hBN substrate as we will discuss below.

4.3 Structural Properties of Bi_2Se_3 Thin Films on hBN Layers

In order to characterize the crystal structure and the epitaxial relationship between the film and the substrate, we investigated the microstructures of the films using TEM. For plan-view TEM observations, the films were grown directly on hBN which was prepared on a suspended SiN_x membrane with a micrometre-size (5 × 5 μm^2) using polymer stamps (Figure 4.2; see Section 3.2 for details). The TEM was performed without any further TEM sample preparation such as thinning, thanks to high mechanical strength and electron beam transparency of Bi_2Se_3/hBN. This method enabled

us to investigate microstructures of the films without time-consuming and destructive post-growth TEM sample preparation procedure [49].

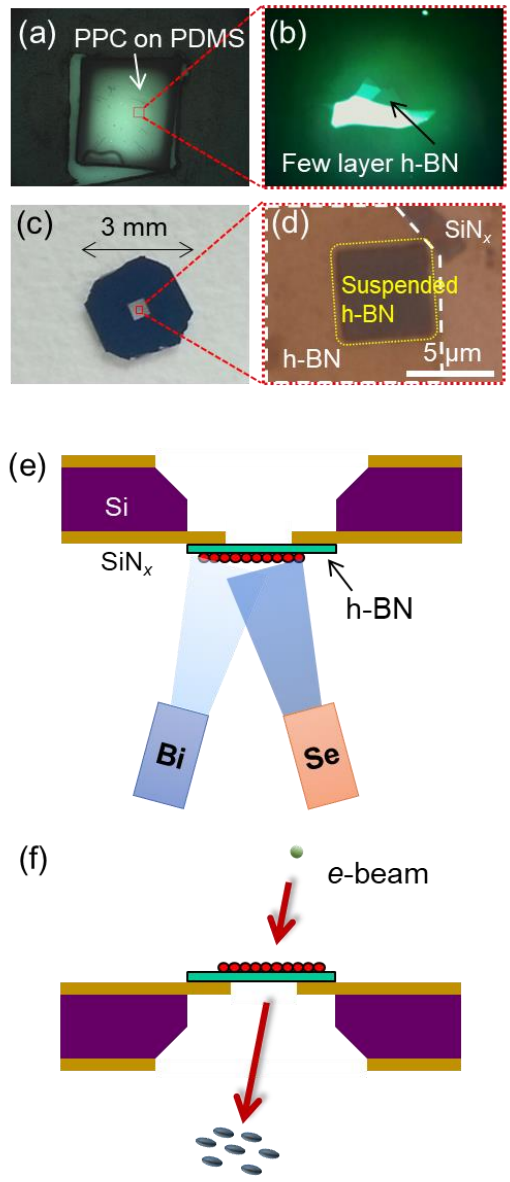

Figure 4.2 Preparation of TEM compatible chips for MBE growth on hBN. (a) and (b) Optical microscope images of hBN picked up by PPC on PDMS which was originally exfoliated onto 90 nm SiO_2. (c) and (d) Optical images of the hBN transferred onto the etched hole in a SiN_x/Si membrane chip. Schematic diagrams of (e) MBE growth of Bi_2Se_3 on the TEM compatible chip with hBN on it and (f) the direct TEM observation without any additional sampling process.

The crystalline quality of the Bi_2Se_3 films was examined by plan-view TEM. Figure 4.3(a) shows selected-area electron diffraction (SAED) patterns obtained from the area highlighted in the BF image (the inset of Figure 4.3(a)) with an aperture size of ~1.3 μm. The SAED pattern exhibits the hexagonal symmetry, representing a highly aligned crystal structure of the film in the selected region. The statistical distribution of the in-plane alignment of Bi_2Se_3 thin films was estimated as a standard deviation width narrower than ±1° in the SAED intensity profile of $Bi_2Se_3\{10\bar{1}0\}$. Figure 4.3(b) shows an overlapped HR-TEM image of Bi_2Se_3 and hBN lattices. In order to highlight the contribution of Bi_2Se_3 only, the image was reconstructed using Bi_2Se_3 $\{11\bar{2}0\}$ spots in its fast Fourier transformed (FFT) pattern (upper inset). The resulting image, shown in the lower inset, reveals a lattice spacing of 0.21 nm, agreeing well with the spacing of the $\{11\bar{2}0\}$ planes of Bi_2Se_3 [16].

In addition to the plan-view characterization, the interface of the Bi_2Se_3/hBN heterostructure was examined in detail using cross-sectional HR-TEM. It is known that the heterointerface between TI and substrate greatly affects the formation of TSS [19,61]. Atomically flat vdW surface of hBN substrates can provide a noninvasive interface to the TSS on the Bi_2Se_3 interfaced with the hBN. The cross-sectional TEM image of Figure 4.3(c) shows layered structures of Bi_2Se_3 and hBN unambiguously. From the image, the lattice spacings between adjacent planes were measured to be 0.96 and

0.33 nm in the Bi_2Se_3 thin film and hBN layer, corresponding to the *d*-spacings of Bi_2Se_3(0003) [16] and hBN(0002) [55], respectively. The cross-sectional TEM image also exhibits that the film is of high crystallinity without a presence of amorphous layer or other unwanted interfacial layers down to the first QL, displaying an atomically sharp interface with the underlying hBN layers. FFT patterns (bottom insets) show well-aligned out-of-plane directions of the two heterogeneous vdW layers, and further support the absence of crystalline phases other than Bi_2Se_3 and hBN at the interface. Moreover, no extended crystal defects such as threading dislocations were observed at the interface. All the microstructural features described above indicate that Bi_2Se_3 thin films grown on hBN layers are of high structural quality.

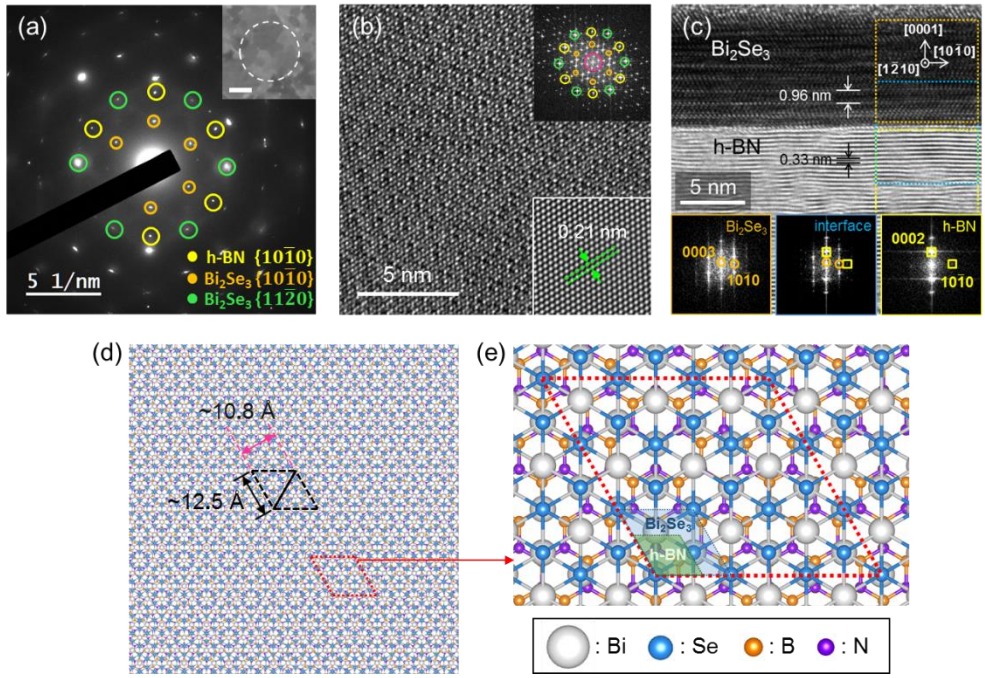

Figure 4.3 Structural characterization of Bi_2Se_3 thin films grown on hBN layers. (a) SAED patterns obtained from the area shown in the inset (scale bar, 500 nm). (b) Plan-view HR-TEM image. Upper inset shows corresponding FFT pattern. Lower inset shows Fourier-filtered image reconstructed from Bi_2Se_3 {11$\bar{2}$0} set of the FFT pattern. (c) Cross-sectional HR-TEM image of the Bi_2Se_3/hBN heterointerface. The bottom insets are FFT patterns obtained from marked areas. (d) Low- and (e) high-magnification ball-and-stick model of epitaxial Bi_2Se_3/hBN heterostructure viewed along [000 $\bar{1}$]. Periodic triangular Moiré fringes are clearly seen in (d). The (3 × 3)–Bi_2Se_3/(5 × 5)–hBN supercell (red dotted line) and primitive unit cells of Bi_2Se_3 (blue shaded area) and hBN (green shaded area) are indicated in (e).

The TEM characterization also revealed the heteroepitaxial relationship and microstructural properties of Bi_2Se_3/hBN. Figures 4.3(a)–(c) show the crystallographic directions of Bi_2Se_3 and hBN aligned each other with a well-defined epitaxial relationship of $(10\bar{1}0)[0001]_{Bi_2Se_3} \| (10\bar{1}0)[0001]_{hBN}$. This is rather surprising since the vdW interaction between two surfaces is expected to be weak and their lattice mismatch is as large as +65.6% in this configuration. It is also in contrast to the heteroepitaxial relationship of $(11\bar{2}0)[0001]_{overlayer} \| (10\bar{1}0)[0001]_{substrate}$ predicted in many theoretical [62-64] and experimental [21,65] works on $(Bi_xSb_{1-x})_2(Se_yTe_{1-y})_3$/hBN (or graphene) systems, whose in-plane crystallographic directions are expected to be rotated by 30° with respect to each other to minimize the lattice misfit (–4.4% for $(11\bar{2}0)[0001]_{Bi_2Se_3} \| (10\bar{1}0)[0001]_{hBN}$. This result is also notably different from the heteroepitaxy of non-layered hexagonal lattices such as GaN (or AlN) on Al_2O_3(0001), where the 30°-rotated in-plane alignment is preferred. These heteroepitaxial growths between non-vdW hexagonal lattices suffer from large lattice misfits, since dangling bonds are minimized in this configuration [66,67]. The observation of near-zero rotation angle of heteroepitaxial lattices in spite of a large lattice mismatch thus strongly suggests that the interaction at the vdW heterointerface between the Bi_2S e_3 film and hBN is weak.

To gain further insights into this heteroepitaxial alignment, we represent a ball-and-stick lattice model in Figures 4.3(d) and (e), constructed based on our TEM observations. The large difference in lattice parameters between Bi_2Se_3 and hBN provides a larger scale periodic modulation of the lattices, called Moiré pattern. The low-magnification view in Figure 4.3(d) shows distinct triangular Moiré fringes with a periodicity of ~12.5 Å. The in-plane lattice constants of Bi_2Se_3 and hBN are 4.14 Å [16] and 2.50 Å [55], respectively. With a small misfit, only –0.64%, these two lattices can be fit to the Moiré periodicity, which is ~3 and ~5 times larger than the original lattices, respectively. This simple model thus predicts the possible formation of a (3 × 3)–Bi_2Se_3/(5 × 5)–hBN epitaxial supercell. The magnified lattice model in Figure 4.3(e) clearly displays this supercell structure. This atomic model is in good agreement with the FFT of the plan-view HR-TEM image (upper inset in Figure 4.3(b)): the innermost six spots, marked by the pink circle, correspond to the triangular Moiré pattern with a periodicity of ~1.1 nm in the Bi_2Se_3/hBN heterostructure, in accordance with the calculated $d_{10\bar{1}0}$ value of 10.8 Å of the (3 × 3)–Bi_2Se_3/(5 × 5)–hBN supercell.

4.4 Electronic Transport Properties of Bi_2Se_3 thin films on hBN Layers

4.4.1 Gate dependencies of the longitudinal and the Hall resistances

Magnetotransport measurements were performed to investigate the electronic properties of the Bi_2Se_3 thin films grown on hBN. Using a standard e-beam lithography followed by depositing metal electrodes and lift-off procedure, we fabricated electrical contacts on the Bi_2Se_3 thin films. Further plasma etching procedure protected by patterned resist resulted in a Hall bar shaped device where magnetotransport can be measured (inset of Figure 4.4(a)). Highly doped silicon substrate supporting hBN substrate serves as a back gate, tuning the carrier density in the film. Figure 4.4(a) shows the longitudinal resistance (R_{xx}) as a function of back gate voltage (V_g) at the zero applied magnetic field ($B = 0$). R_{xx} decreases as V_g increases within the range of gate voltage we applied (–120 to 80 V), suggesting that the film is overall *n*-type. Correspondingly, the Hall resistance (R_{xy}) measured as a function of magnetic field B (Figure 4.4(b)) exhibits negative slope ($dR_{xy}/dB < 0$) at various fixed gate voltages, also suggesting the *n*-type conduction in the film. However, we also observed that $R_{xy}(B)$ exhibits nonlinearity in B, especially at the negative V_g values. Nonlinear $R_{xy}(B)$ is often attributed to the presence of multiple conduction channels by carriers with different natures [68].

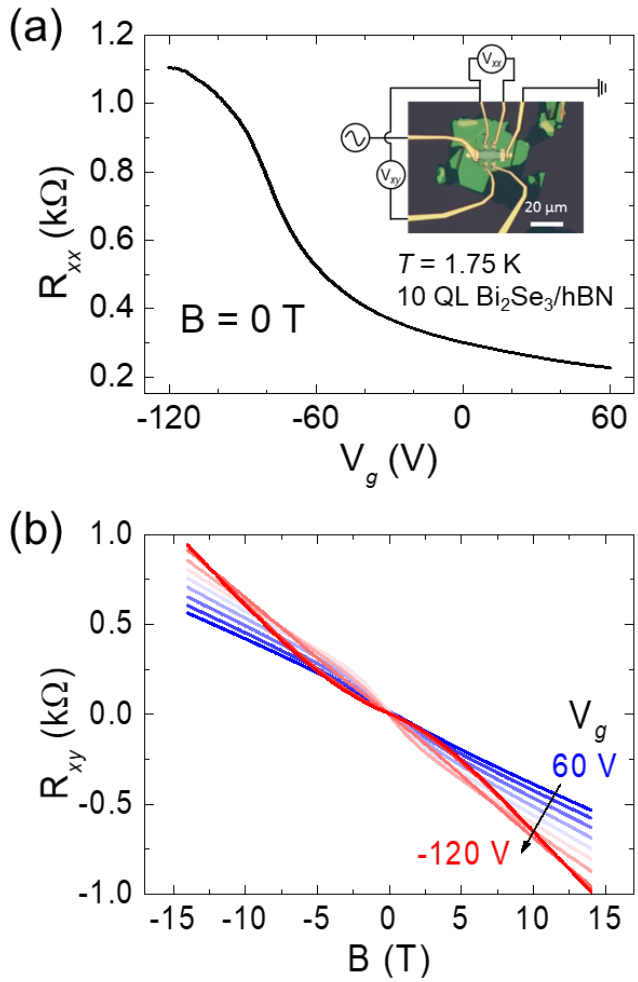

Figure 4.4 (a) Gate voltage dependence of $R_{xx}(B = 0)$. The inset shows an optical microscope image of the Hall bar sample based on 10 QL Bi_2Se_3/hBN and the measurement configuration. (b) R_{xy} *vs*. B taken at different gate voltages. All graphs are taken at $T = 1.75$ K.

Since a TI thin film with a gapped out bulk has two conducting surfaces, the observed multiple conduction channels can be naturally associated with the two surface states in the thin film: top surface state and bottom surface state interfaced with hBN. In principle, the bulk can contribute yet another conduction channel if it is heavily doped. However, as we discuss below, we rule out this possibility in the high-quality MBE-grown samples. Considering the short screening length [69] due to the high dielectric constant of $\varepsilon_{\perp}$ ~113 [70] of the Bi_2Se_3, the electric field from the back gate is almost perfectly screened by the bottom TSS, and hence, there is virtually no gate dependence in the top TSS. In the gate dependent data shown in Figure 4.4(a), a close inspection indicates dR_{xx}/dV_g approaches zero as V_g becomes large negative voltages. Near V_g = –120 V, dR_{xx}/dV_g reaches almost zero, suggesting that the charge neutral Dirac point of the bottom TSS is near the Fermi energy at this large negative gate voltage. We also note that $R_{xy}(B)$ deviates more from a linear curve as V_g approaches the negative limiting value (–120 V) as shown in Figure 4.4(b). Such a deviation from linear $R_{xy}(B)$ strongly suggests that the transport occurs through multiple channels with different mobilities and densities [68,71]. Similar behaviour has been observed in the mechanically exfoliated TIs, on which the widely changing $R_{xx}(V_g)$ and the nonlinear $R_{xy}(B)$ tuned by the back gate voltage were attributed to the conduction through two different TSSs on the top and bottom of the samples [72,73].

4.4.2 Analysis of multiple conduction channels in Bi_2Se_3/hBN

We analyzed our measured $R_{xx}(B)$ and $R_{xy}(B)$ at various fixed gate voltages using a multiple conduction model with carrier mobilities and densities as fitting parameters [72,74,75]. We used the Hall conductance

$$G_{xy} \equiv \frac{R_{xy}}{R_{xx}^2 + R_{xy}^2} = \sum_i G_{xy,i} \,,$$

where R_{xy} and R_{xx} are the Hall resistance and the sheet resistance, respectively, for the multiple channel conduction analysis since it provides simple fitting process and reliable results. Here, the Hall conductance of each parallel channel is given by

$$G_{xy,i} = eB\left(\frac{n_i \mu_i^2}{1 + \mu_i^2 B^2}\right),$$

where e is the elementary charge, B is the applied magnetic field, and n_i and μ_i are the sheet carrier density and the mobility of this channel.

2-channel 4-parameter (n_1, n_2, μ_1, μ_2) fitting to G_{xy} data gave the most reliable results for all V_g values except for V_g = –100 V where single channel best fits the experimental data; consistently, the two channel fitting also gives n_1=0 at V_g = –100 V. Figures 4.5(a)–(c) show that the fitting curves are in good agreement with experimental data.

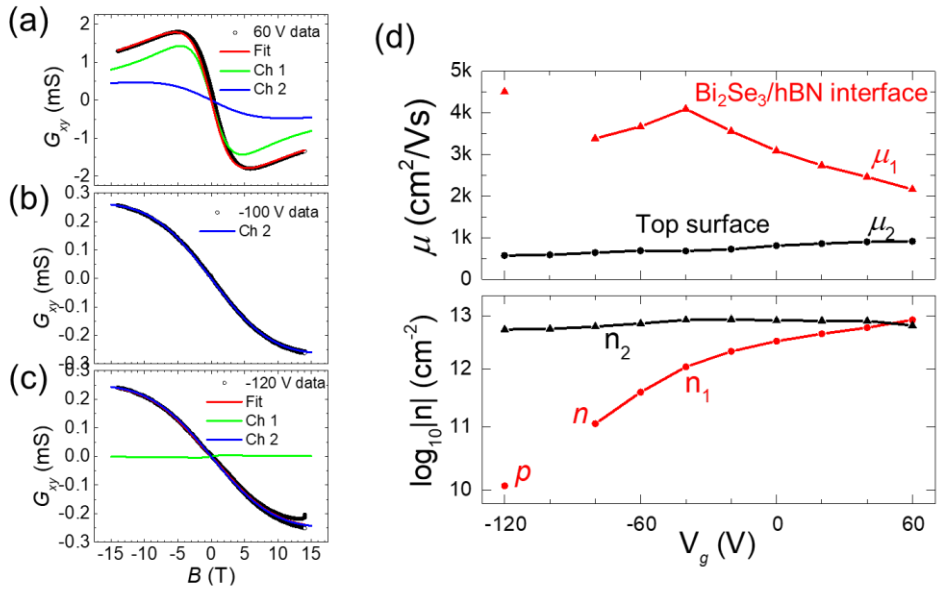

Figure 4.5 Hall conductance data *vs*. fitting curves at back gate voltages of (a) 60 V, (b) –100 V, and (c) –120 V. The open black circles are experimental data and the red solid line is the fitted curve. The green and blue solid lines represent Hall conductances of bottom and top surface channel, respectively. There is a slight field hysteresis in the experimental data in (c). (d) Carrier mobilities μ and carrier densities n *vs*. V_g, obtained by the multiple channel conduction model while the single channel model ($n_1 = 0$) gives the best fit for $V_g = -100$ V. The sign of n_1 changes at $V_g = -120$ V.

The best fit values of carrier mobilities (μ_1 and μ_2) and corresponding carrier densities (n_1 and n_2) are shown in Figure 4.5(d). One channel with a lower mobility and higher density (μ_2, n_2) remains relatively constant over the whole V_g range. However, the other channel, which exhibits a higher mobility and lower density (μ_1, n_1), shows a sensitive gate voltage dependence. Considering the physical proximity of the bottom TSS to the back gate in our device geometry, we therefore assign this high mobility low density channel is the TSS at the bottom interface. For this hBN protected channel, the mobility reaches as high as μ_1 = 4500 $cm^2\ V^{-1}\ s^{-1}$. n_1 also exhibits a strong gate dependence, where we estimated $dn_1/dV_g = 6 \times 10^{10}\ cm^{-2}\ V^{-1}$, in an excellent agreement with the back gate capacitance 0.09 fF μm^{-2} of our devices. Since the highly crystalline Bi_2Se_3/hBN interface is sealed in an UHV environment and protected by hBN from external contamination, it was able to preserve the TSS as the dominant conduction channel with a high carrier mobility and low carrier density, even after lithography and device fabrication in ambient environments.

The channel with the lower mobility and the higher carrier density exhibiting no appreciable gate dependence in aforementioned analysis can be attributed to the bulk conduction, the top TSS, and/or topologically trivial 2D electron gas (2DEG) states developed by the top surface band bending due to environmental effects [76]. Among the various potential scenarios, we rule out the bulk conduction based on tilted magnetic field angle dependent R_{xx}

measurements and observations of weak anti-localization (WAL) effects from two decoupled 2D natured conduction channels, as described in the next section. It is difficult to differentiate the effects of top TSS and 2DEG in our experiment, but it is likely that the top surface conduction is dominated by the 2DEG state, considering its high carrier density and low mobility [72].

4.4.3 Two-dimensional, two decoupled conduction channels: ruling out bulk contribution to electrical transports

A commonly used method to confirm that a magnetotransport phenomenon is of two-dimensional (2D) nature and devoid of bulk contribution is to perform field-angle dependent measurements [72,77]. If the conduction is purely from 2D states, it should depend only on the normal component of the magnetic field ($B_\perp = B\cos\theta$; θ = tilt angle from the surface normal), while a three-dimensional (3D) bulk conduction is expected to deviate from this tendency. Figure 4.6 shows the magnetic field-angle dependent measurement of the longitudinal resistance R_{xx}. At each back gate voltage (V_g), all of the R_{xx} curves taken at different filed angles nicely fit into a single universal curve when plotted as a function of $B_\perp = B\cos\theta$, for the entire gate voltage range ($-120 \leq V_g \leq 60$ V) and field range ($-14 \leq B\cos\theta \leq 14$ T) of our measurements. This strongly suggests that the conduction in our Bi_2Se_3/hBN had a 2D nature throughout the measurements.

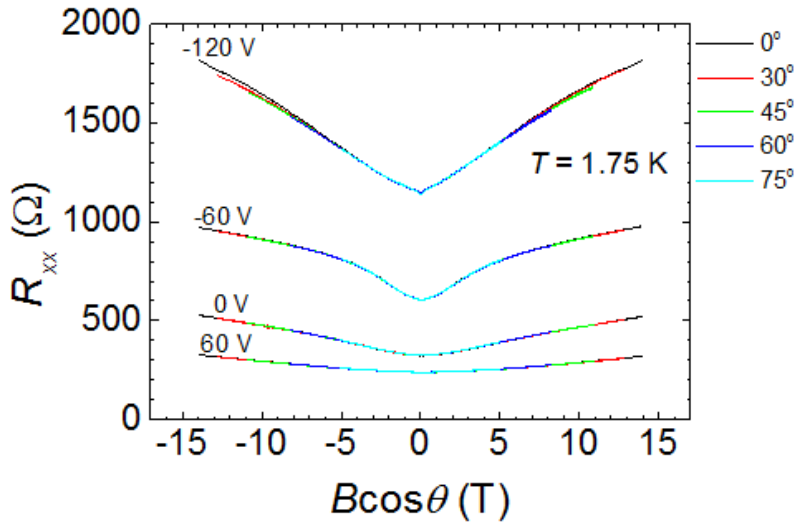

Figure 4.6 $R_{xx}(B)$ *vs.* $B\cos\theta$ for different field angles and gate voltages, measured at T = 1.75 K.

The 2D-natured conduction was further evidenced by temperature (T) dependent measurements of WAL effects, which appears as a cusp in magnetoconductance at low magnetic fields. Figure 4.7(a) shows the WAL effects observed at different temperatures and the corresponding best fitting lines based on Hikami-Larkin-Nagaoka (HLN) formula, which gives a quantitative analysis on the WAL effects:

$$\Delta G_{xx}(B) = \alpha \frac{e^2}{\pi h}\left[\ln\left(\frac{\hbar}{4el_\phi^2 B}\right) - \psi\left(\frac{1}{2}+\frac{\hbar}{4el_\phi^2 B}\right)\right],$$

where $\Delta G_{xx}(B)$ is the magnetoconductance correction, l_ϕ is the phase coherence length, α is a parameter related to the number of conducting 2D channels in the limit of strong spin-orbit coupling (SOC) (α = 0.5 for each channel), e is the elementary charge, h ($\hbar$) is the Planck's constant (h deviced by 2π), and $\psi(x)$ is the digamma function [78]. The l_ϕ extracted at different temperatures exhibited a power dependence of $l_\phi \propto T^{-0.46}$ (Figure 4.7(b)), agreeing well with the characteristic power law of $l_\phi \propto T^{-1/2}$ for 2D electron-electron interaction dephasing mechanism (for the 3D case, l_ϕ should scale as $T^{-3/4}$), supporting the 2D nature of the conduction.

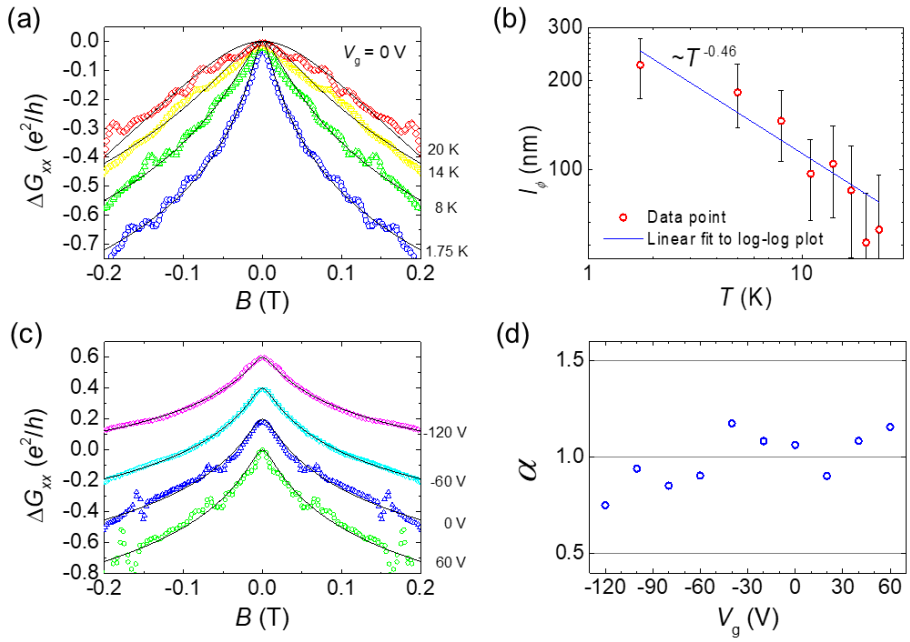

Figure 4.7 Weak anti-localization effects. (a) Temperature dependence of $\Delta G_{xx}(B) = G_{xx}(B) - G_{xx}(B = 0)$ at $V_g = 0$ V. The solid lines are best fits to the HLN formula. (b) Phase coherence length l_ϕ *vs.* temperature obtained from the fittings shown in (a). (c) Gate voltage dependence of $\Delta G_{xx}(B)$ measured at 1.75 K. The solid lines are best fit to the HLN formula. Each curve is shifted vertically by 0.2 e^2/h for clarity. (d) V_g *vs.* parameter α obtained from the fittings shown in (c)

Another important parameter in WAL analysis is the channel number, α; each independent channel contributes 0.5 to α. Figures 4.7(c) and (d) show the V_g dependence of WAL effects and the obtained effective channel numbers *vs.* V_g, respectively. It is notable that $\alpha \approx 1.0$ was almost independent to V_g, indicating the presence of two decoupled conduction channels for the whole V_g range in our measurements. It is also in good agreement with the multiple channel Hall analysis described in the main text. The α values in previously reported undoped Bi_2Se_3 thin films grown on covalently bonded substrates, such as Al_2O_3(0001), Si(111) and amorphous SiO_2, were close to 0.5, deviated far from 1.0 [69]. Those films presumably hosted an extended bulk state, where a strong bulk conduction forms an effective single conduction channel by coupling with the surface states on the top and bottom sides. It was also demonstrated that the bulk state of Bi_2Se_3 could be depleted by compensation doping, increasing α from 0.5 to 1.0 [18]. Meanwhile, in our undoped Bi_2Se_3/hBN case, we rule out the extended bulk state scenario as both the field-angle dependent measurements and the temperature dependent WAL effects consistently indicate conduction of 2D nature. Hence, the observation of two decoupled WAL channels in undoped Bi_2Se_3, together with the 2D nature, strongly suggest the negligible bulk conduction (or localized bulk states) and the high-quality of our Bi_2Se_3/hBN samples.

Moreover, WAL analysis further indicates that the two 2D conduction channels are in the strong SOC limit. However, in addition to the topological surface state, the topologically trivial Rashba-split 2D 2DEG states that may form at the surface accumulation layers of 3D topological insulators also exhibit WAL effects, and α does not distinguish WAL effects arising from the two topologically distinct states. Therefore, while one of the two channels was found to be indeed from the bottom TSS by observing the Berry phase of π from the gate-dependent SdH oscillation measurements described in the next section (Figure 4.8), it remains inconclusive whether the other conduction channel was the top TSS or a topologically trivial 2DEG state.

4.4.4 Shubnikov-de Haas oscillations observed in Bi_2Se_3/hBN

The Dirac nature of the high mobility TSS at the Bi_2Se_3/hBN interface was proved by pronounced SdH oscillations observed at high magnetic fields. Figure 4.8(a) shows SdH oscillations in background-subtracted $\Delta R_{xx}(1/B)$ at V_g = 60 V, where the contribution of the TSS at the Bi_2Se_3/hBN interface to the total conduction is the strongest. Clear observation of oscillatory features in $1/B$ suggests well-quantized Landau orbits in the bottom TSS. In Figure 4.8(b), the Landau level (LL) index n is plotted as a function of the position $1/B$ of the most prominent SdH maxima and minima at each gate voltage. Linear fits provided the n-axis intercepts of 0.5 as seen in the inset, a prominent result due to the π–Berry phase carried by Dirac fermions in the TSS [79-81]. Figure 4.8(c) shows SdH oscillations in $R_{xx}(B)$ measured at different temperatures at zero gate bias, mainly originating from the high-mobility TSS at the Bi_2Se_3/hBN interface. Using a Lifshitz-Kosevich analysis [82], the cyclotron mass was calculated to be m_{cyc} = 0.08 m_e, where m_e is the free electron mass (Figure 4.8(d)).

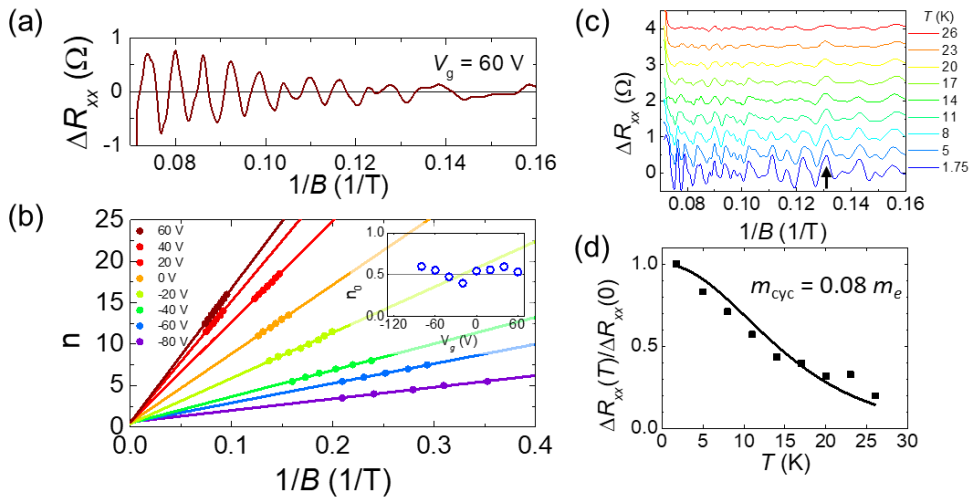

Figure 4.8 Shubniknov-de Haas oscillations observed in Bi_2Se_3/hBN. (a) Amplitude of SdH oscillations *vs*. 1/*B* at V_g = 60 V. (e) Landau fan diagram of the peaks from TSS at the Bi_2Se_3/hBN interface. The inset shows the intercept *vs*. gate voltages. All graphs are taken at 1.75 K. (c) SdH oscillations in R_{xx} *vs*. 1/*B* for different temperatures at V_g = 0 V. Each curve is shifted vertically by 0.5 Ω for clarity. (d) Normalized SdH amplitude of the n = 11.5 LL peak at B = 7.64 T indicated by the arrow in (c) *vs.* temperature. The solid line is the best fit to the Lifshitz-Kosevich theory, yielding a cyclotron mass of 0.08 m_e.

4.4.5 Comparison of transport properties of Bi_2Se_3 thin films grown on various substrates by MBE

Table 4.1 Electronic transport properties of MBE-grown Bi_2Se_3 thin films on various substrates.

Substrate	t	T (K)	n_{Hall} (10^{12} cm^{-2})	μ_{Hall} (cm^2/Vs)	WAL α	SdH γ	Note	Ref.
Si(111)	10	1.5	~15	200	0.6	-	t -dependent	[83]
GaAs(111)	16	0.5	20	630	0.4	-		[84]
CdS(0001)	10	1.9	13 (impurity) 4 (TSS)	380 (impurity) 5000 (TSS)	-	0.35		[75]
c-Al_2O_3	20	2	62	807	0.3	-	*in-situ* Se capping	[85]
c-Al_2O_3	10	1.6	38 (bulk) 2.6 (TSS)	540 (bulk) 1600 (TSS)	0.5	0.4		[86]
c-Al_2O_3	8 to 256	1.5	30 (bulk) 8 (2DEG)	500 (bulk) 3000 (2DEG)	0.6	-		[74]
c-Al_2O_3	20	1.5	5.0	~2000	1	0.25	Cu doping	[18]
$BiInSe_3$ buffer on c-Al_2O_3	15	1.5	1.3	11400	-	-	uncapped	[19]
	16		1.1 (TSS)	3300 (TSS)	-	- (QH)	MoO_3-capped	
$SrTiO_3$(111)	10	0.1 (Hall) 1.6 (WAL)	–3 to +30	~1000	0.5–1	-	bottom gating	[59]
hBN(0001)	10	1.75	5.4–8.5 (top 2DEG) –0.011 to +8.3 (bottom TSS)	570–910 (top 2DEG) 2200–4500 (bottom TSS)	1	0.5	bottom gating	This work

Table 4.1 summarizes and compares electronic transport properties of MBE-grown Bi_2Se_3 thin films. n_{Hall} and μ_{Hall} are the carrier density and the mobility measured by the Hall effect. WAL α represents the number of independent conduction channel (0.5 per channel), and SdH γ = 0.5 (0) corresponds the Berry phase of π (0). QH denotes that the quantum Hall effect was observed (at T = 0.3 K and B = 29 T). For a suitable comparison, we listed transport properties of Bi_2Se_3 under similar conditions; MBE-grown thin films with a similar thickness t (in QL) and at a similar measurement temperature T.

4.5 Summary

High-quality topological insulator was obtained from Bi_2Se_3 thin films grown on hBN layers using MBE. To obtain fast microstructural feedback on MBE growth of the films on hBN, we employed the TEM-compatible MBE technique. Bi_2Se_3 thin films with atomically smooth terraces over a large area have been obtained by employing the two-step growth method. The optimized samples exhibited high crystallinity, epitaxially oriented Bi_2Se_3 film on an hBN substrate with atomically sharp interfaces, as confirmed by TEM studies. Furthermore, magnetotransport experiments revealed that the dominant channel of transport was *via* the TSS at the Bi_2Se_3/hBN interface with an enhanced carrier mobility. More generally, we believe that the experimental scheme demonstrated in this report can serve as a promising method for the preparation of high-quality TI thin films as well as many other heterostructures based on 2D vdW layered materials.

4.6 [Supplementary] Heteroepitaxial Growth of Topological Insulator Thin Films on Various van der Waals Materials

The two-step growth scheme developed for the preparation of high-quality topological insulator Bi_2Se_3 thin films on hBN layers can be expanded for various TI/vdW material combinations. Here, some representative examples are presented.

4.6.1 Telluride TIs and graphene substrates

Ternary telluride TI materials of $(Bi_xSb_{1-x})Te_3$ have played a crucial role in the field of topological insulators as bulk-insulating TIs have been achieved by alloying *p*-type Sb_2Te_3 and *n*-type Bi_2Te_3 [87,88]. Moreover, quantum anomalous Hall effect has been experimentally realized in magnetically doped $(Bi_xSb_{1-x})Te_3$ systems [89].

By adopting the two-step growth method with a slight change in growth temperatures, uniform thin films of Sb_2Te_3 and Bi_2Te_3 could be heteroepitaxially grown on hBN and graphene layers, as shown in Figure 4.9. The growth temperature for Sb_2Te_3 (Bi_2Te_3) was lower (higher) than that of Bi_2Se_3, while the flux of group V material and the VI/V flux ratio kept the same as Bi_2Se_3's case. The $1^{st}/2^{nd}$ step growth temperatures were 150/300–330ºC for Sb_2Te_3 and 230–260/305–325ºC for Bi_2Te_3.

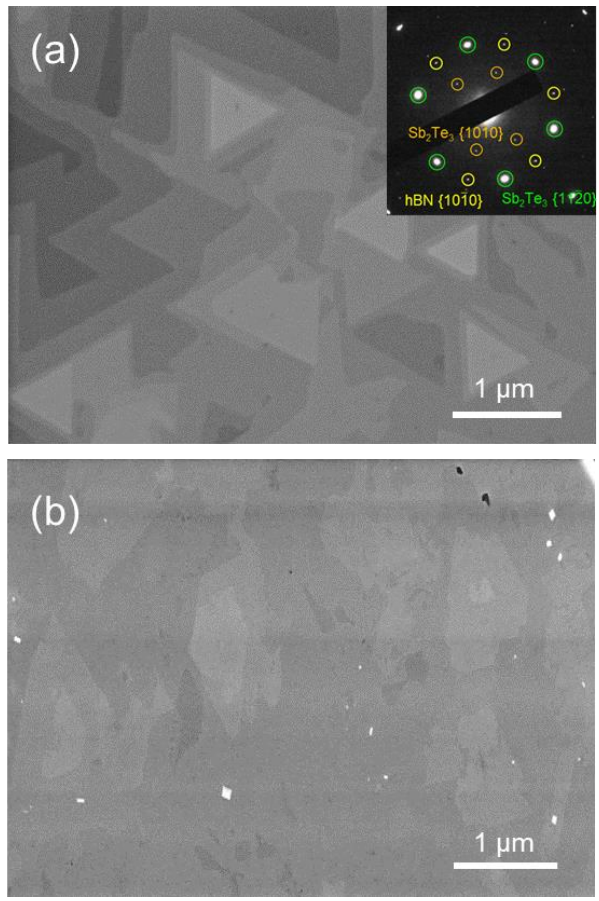

Figure 4.9 (a) SEM image of 20 QL Sb_2Te_3 thin film grown on hBN layers. Inset: SAED pattern of the Sb_2Te_3/hBN heterostructure obtained by plan-view TEM. (b) SEM image of 6 QL Bi_2Te_3 thin films grown on few-layer graphene.

4.6.2 Bi_2Se_3/WSe_2 for TI/TMD heterostructures

Extended further from the vdW substrates with honeycomb lattices such as hBN and graphene, the growth scheme developed in this dissertation could be applied to the TMD substrates as exemplified by WSe_2. Bi_2Se_3 thin films have been grown on exfoliated single crystals of WSe_2 using the two-step growth method with the growth conditions same as on hBN. Most importantly, monolayer WSe_2 served as a substrate for an ordered growth of Bi_2Se_3 as displayed in Figures 4.10(a) and (b). Unlike irregular Bi_2Se_3 nanograins grown on amorphous SiO_2 area, Bi_2Se_3 grown on the monolayer WSe_2 exhibited micrometer-scale triangular domains. Moreover, the crystal facets of Bi_2Se_3 were aligned by multiple of 60^o and also aligned parallel to the long straight edges of WSe_2 monolayer (Figure 4.10(b)), suggesting the existence of an epitaxial relationship. The heteroepitaxial growth of TI Bi_2Se_3 films on monolayer WSe_2 can provide an important step for the opto-spintronic applications since semiconducting TMDs including WSe_2 exhibit direct to indirect bandgap transition when the thickness is thicker than monolayer [90,91].

Plan view TEM investigation unambiguously revealed the heteroepitaxial relationship of $(10\bar{1}0)[0001]_{Bi_2Se_3} \parallel (10\bar{1}0)\,[0001]_{WSe_2}$, which was uniform over the entire area of the WSe_2 flake (Figure 4.10(c)). High-resolution plan-view observation of the heterostructure exhibited uniformly distributed Moiré patterns, suggesting that the two lattices form supercells

through the heteroepitaxial alignment (Figure 4.10(d)). It is supported by the ball-and-stick simulation of the lattices, as shown in Figures 4.10(f) and (g). The parallelly aligned 4 unit cells of Bi_2Se_3 and 5 unit cells of WSe_2 formed a super periodicity of ~1.65 nm with a small misfit of ~0.4%, which is in good agreement with the HR-TEM results. The cross-sectional HR-TEM lattice image in Figure 4.10(e) shows the clean and sharp interface of the Bi_2Se_3/WSe_2 heterostructures together with the layered structures of each lattice. The formation of well-defined epitaxial supercells over a large area despite the large lattice mismatch of 25.5% in the unit cell scale can be attributed to the weak interaction at the clean vdW interface. The microstructural investigations described above indicate that Bi_2Se_3 thin films grown on WSe_2 layers are of high structural quality.

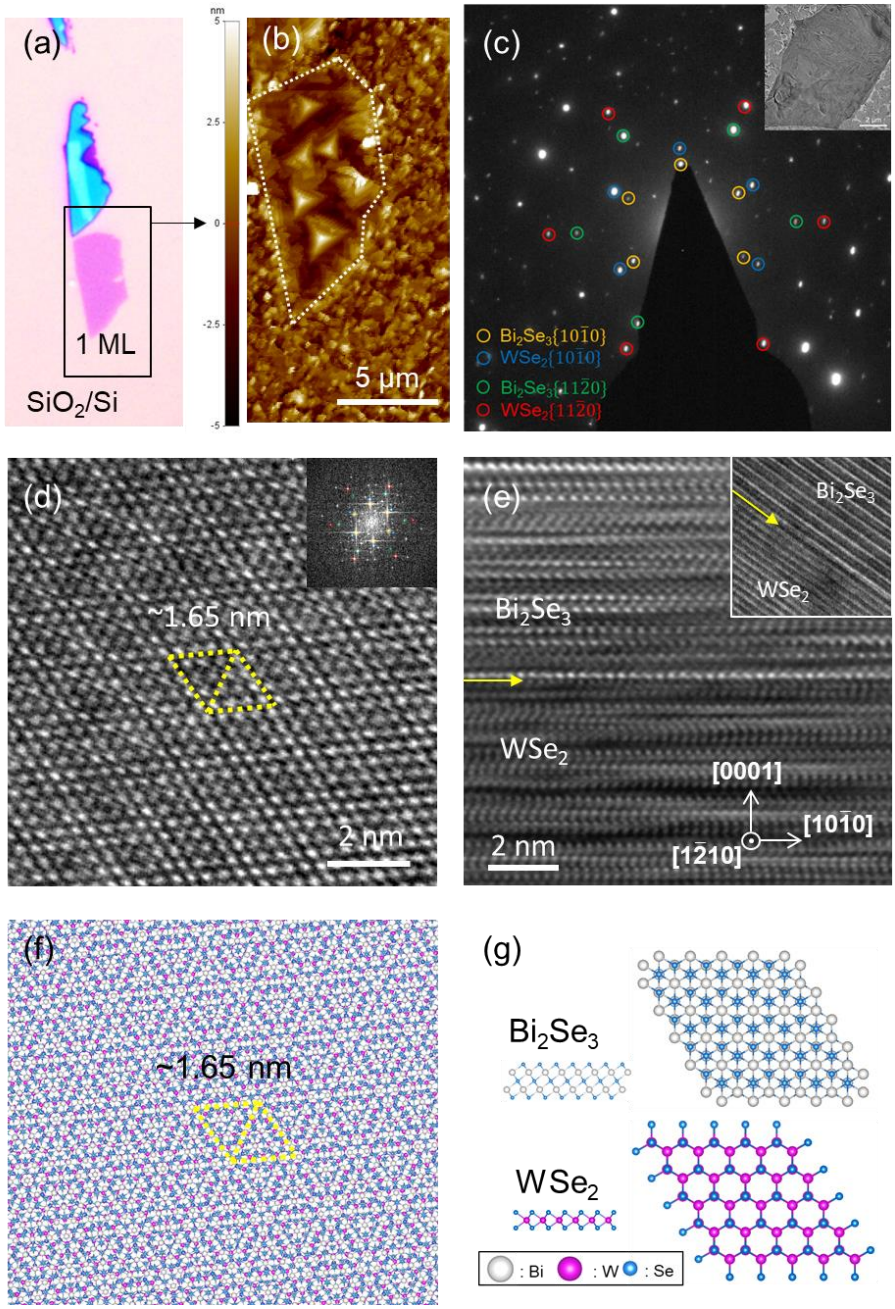

Figure 4.10 (a) Optical image of monolayer WSe_2 on a 300 nm SiO_2/Si substrate. (b) AFM topography of 20 QL Bi_2Se_3 grown on the monolayer WSe_2 displayed in (a). (c) Plan-view SAED, (d) plan-view HR-TEM image, (e) cross-sectional HR-TEM image, and (f) ball-and-stick lattice model of the Bi_2Se_3/WSe_2 heterostructure. (g) Bi_2Se_3 and WSe_2 lattices comprising the unit cell of the 4:5 epitaxial supercell. Thick (t = a few tens of nanometers) WSe_2 flakes were used for the TEM observations.

4.6.3 Bi_2Se_3/α-$RuCl_3$ for TI/quantum spin liquid candidate heterostructures

Heteroepitaxial growth of Bi_2Se_3 TI thin films on α-$RuCl_3$ — a more structurally, chemically, and electronically different vdW substrate — for the preparation of TI/quantum spin liquid heterostructures is described in detail in Appendix.

5 TI/hBN/TI Epitaxial van der Waals Heterostructures for Tunneling Spectroscopy Between Topological Surface States

5.1 Introduction

Van der Waals heterostructures composed of various two-dimensional materials serve as novel platforms to explore a wide variety of interesting physical properties and device applications [1,6,7]. One of the most intriguing systems is a highly crystalline and atomically thin insulating barrier sandwiched between 2D vdW layered materials, since tunneling spectroscopy applied to the heterostructure provides a powerful tool to probe the density of states (DOS) of the materials and vertical transport across the vdW interface [42,92]. In particular, the high crystallinity provided by both tunneling materials and also the tunneling insulator offers a unique chance to investigate the intrinsic momentum-space tunneling selection of the tunneling electrons without dissipation of crystallographic momentum due to random scattering at the interfaces during the tunneling process. For example, precisely aligned two graphene layers separated by a hexagonal boron nitride barrier layer made it possible to detect and manipulate energy-, momentum-, and chirality-conserved tunneling of Dirac fermions in graphene [45-47]. On the other hand, topological insulators of $(Bi, Sb)_2(Te, Se)_3$ compound have

vdW layered structures with topologically non-trivial surface states which provide exciting opportunities to discover novel quantum phenomena occurring at the interface between topologically dissimilar atomic layers [13,14]. In this regard, it would be highly attractive to build a topologically unique heterostructures by bringing two TIs into close proximity with each other across only a few atomic barriers and to explore resonant tunneling conditions of helical Dirac fermions in the system through tunneling spectroscopy.

Here, we present the fabrication and measurement of vertical tunnel junctions in which two epitaxially aligned TIs are separated by a-few-atom-thick hBN tunnel barrier (Figure 5.1). The double-sided MBE growth of Sb_2Te_3 and Bi_2Se_3 on and under the suspended ultrathin hBN layers is demonstrated. High-resolution transmission electron microscopy revealed an atomically abrupt and epitaxial interface formation between the hBN substrate and top- and bottom-TIs. We performed magneto-tunneling spectroscopy of Sb_2Te_3/hBN/Bi_2Se_3 (*p*-TI/hBN/*n*-TI) and Bi_2Se_3/hBN/Bi_2Se_3 (*n*-TI/hBN/*n*-TI) junctions under in-plane and out-of-plane magnetic fields to investigate energy-momentum-spin conserved resonant tunneling between the topological surface states (TSSs).

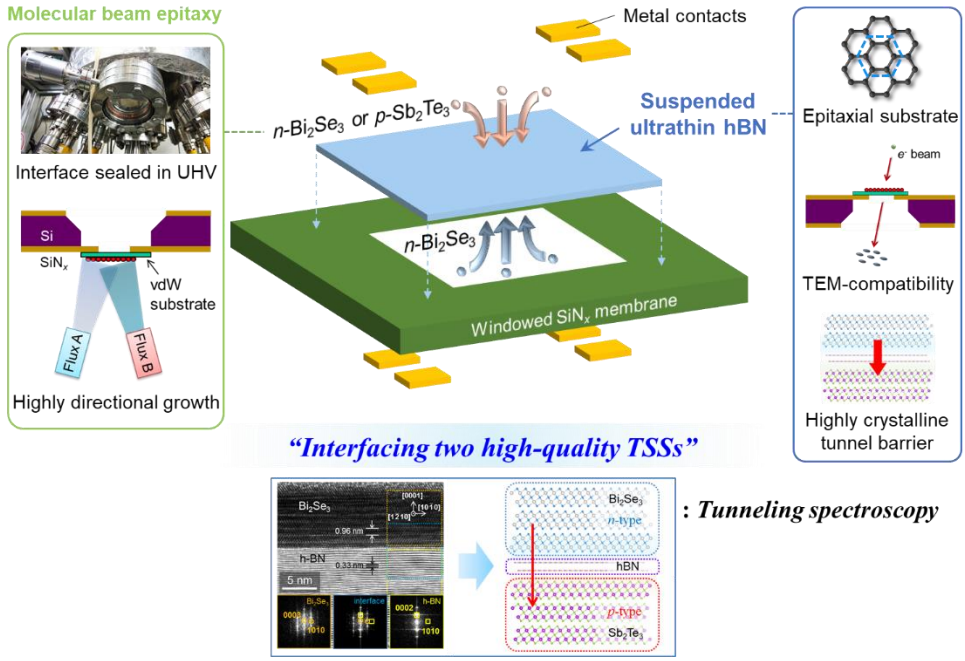

Figure 5.1 Schematic diagram illustrating the approach of this research.

5.2 Double-Sided MBE Growth of Topological Insulator Thin Films on Top and Bottom Surfaces of Suspended hBN

The basic approach for growing TI thins films on both surfaces of suspended hBN is schematically illustrated in Figure 5.2 together with AFM topographic images taken on the top surface of the suspended ultrathin (2 monolayers; MLs) hBN at each step of the double-sided MBE growth of Bi_2Se_3. Ultrathin hBN layers were transferred using micromanipulation to pre-patterned sub-micrometer holes in SiN_x membranes to expose both surfaces (see Section 3.2 for the detailed preparation steps). Subsequently, Bi_2Se_3 or Sb_2Te_3 were grown on both sides of the suspended hBN using MBE, naturally forming vertical tunnel junctions whose interfaces were sealed under UHV. First, Bi_2Se_3 thin films were grown on the bottom side by loading the sample upside-down to the substrate holder of MBE. We used the two-step growth process developed for high-quality Bi_2Se_3 thin film growth on hBN, which is described in detail in the previous chapter. The top surface of the sample remains intact after the bottom side growth, as shown in Figure 5.2(b), preserving atomically flat terraces of hBN. It is attributed to highly directional molecular fluxes of precursors which hardly undergo scattering events during the MBE growth in UHV conditions. After growing the Bi_2Se_3 thin film on the bottom side of the hBN layers, the substrate was inverted *ex-situ* and loaded back to the MBE chamber so that the top side of hBN faces molecular fluxes this time. Then, another round of two-step MBE growth was

carried out to grow Bi_2Se_3 thin films on top of the hBN/Bi_2Se_3 heterostructure, using the same growth parameters as the bottom side growth except for the omission of the pre-growth heat cleaning process in order to protect the hBN/Bi_2Se_3. The resulting Bi_2Se_3/hBN/Bi_2Se_3 suspended double-sided heterostructure exhibited atomically smooth and hexagonally aligned triangular terraces with 1 QL step heights of Bi_2Se_3 as shown in Figure 5.2(c).

Besides the Bi_2Se_3/hBN/Bi_2Se_3 heterostructures, we also prepared Sb_2Te_3/hBN/Bi_2Se_3 heterostructures simply by adopting the Sb_2Te_3 thin film growth parameters (see Section 4.6.1) for the top side growth. The structural and electrical properties of those two types of double-sided vdW heterostructures will be compared in detail in the following sections.

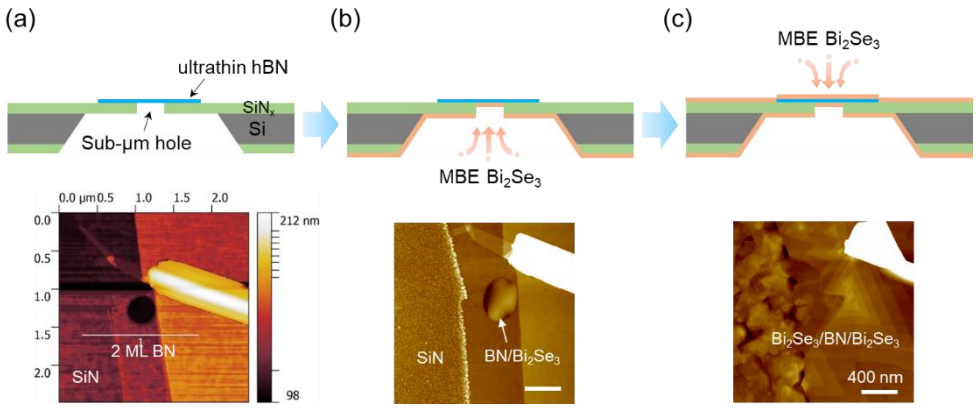

Figure 5.2 Schematic diagrams and corresponding AFM topographic images taken after each step: (a) as-suspended hBN, (b) MBE growth of TI films on the bottom side, (c) MBE growth of TI films on the top side.

5.3 Microstructural Properties of TI/hBN/TI Epitaxial vdW Heterostructures

The microstructural properties of the Bi_2Se_3/hBN/Bi_2Se_3 double-sided heterostructures were investigated by HR-TEM. Bright field cross-sectional TEM image in Figure 5.3(a) shows Bi_2Se_3 thin films separated by a very thin hBN layer in the middle, which appears as a brighter thin line in the image sandwiched by darker slabs, sitting on a ~100 nm diameter hole made in the SiN_x membrane window. It is worth mentioning that the Bi_2Se_3 film grown on the bottom side of hBN extends beyond the boundary of the hole made in the SiN_x membrane, probably due to the diffusion of adatoms through the interface between hBN and SiN_x and the lateral growth mode preferred over the vertical growth mode. Therefore, although the same growth parameters were employed for the film growths on both sides, the thickness of the film on the bottom (8 QL) is found to be about half of that on the top side (15 QL).

The interface of Bi_2Se_3/hBN/Bi_2Se_3 was analyzed in detail with HR-TEM. The HR-TEM image in Figure 5.3(b), which corresponds to the region in Figure 5.3(a) marked by the blue square, clearly shows atomically clean, abrupt, and vdW-layered interfaces between top Bi_2Se_3, bilayer hBN, and the bottom Bi_2Se_3. As in the Bi_2Se_3/hBN single-sided heterostructure investigated in the previous chapter, the lattice spacings between adjacent planes, measured to be 0.96 and 0.33 nm in the Bi_2Se_3 thin film and the hBN

layer, respectively, agreed well with the known values of bulk materials [16,32,55]. It is notable that the Bi_2Se_3 film on the bottom side of hBN has uniformly crystalline structures up to the interface with hBN. It indicates that the bilayer hBN has provided excellent protection to the Bi_2Se_3 from the environments during the *ex-situ* sample flip. The HR-TEM image also exhibits the similar crystal qualities of the top and the bottom Bi_2Se_3 films, indicating the second round of MBE growth has not damaged the crystal structure of the pre-grown bottom Bi_2Se_3 film. FFT patterns on the right panel of Figure 5.3(b), taken on the regions marked by boxes with the corresponding colors, show the epitaxial relationship of $(10\bar{1}0)[0001]_{Bi_2Se_3} \parallel (10\bar{1}0)[0001]_{hBN}$ for both sides, and support the absence of crystalline phases other than Bi_2Se_3 and hBN across the interface. We further examined other regions of the Bi_2Se_3/hBN/Bi_2Se_3 interfaces. Figure 5.3(c) displays a uniform interface quality over the extent of 55 nm, which is a considerable portion of the junction diameter.

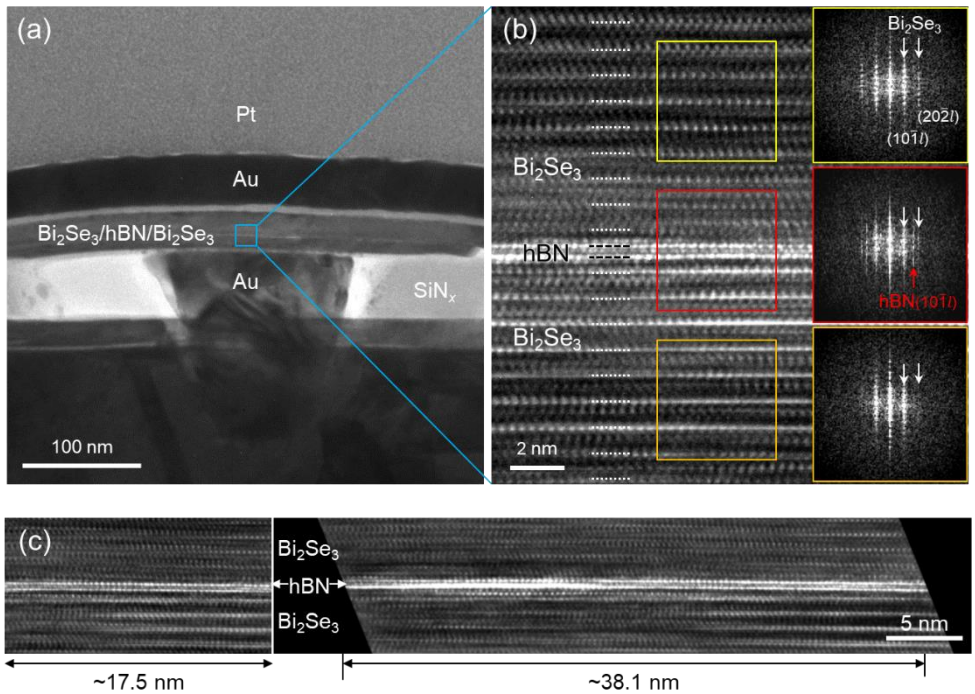

Figure 5.3 Cross-sectional TEM images of Bi_2Se_3/hBN/Bi_2Se_3 suspended epitaxial vdW heterostructures. (a) Low magnification image showing the device structure explicitly. (b) High-resolution lattice image clearly displaying atomically sharp interface. Right panels are FFT of the regions marked by colored boxes in the main figure. (c) More examples of the high-resolution images of the heterointerface.

In addition to the Bi_2Se_3/hBN/Bi_2Se_3 heterostructures, we investigated the Sb_2Te_3/hBN/Bi_2Se_3 heterostructures using cross-sectional HR-TEM and STEM. The HR-TEM image in Figure 5.4(a) displays clean and sharp interfacial structures of Sb_2Te_3/2 ML hBN/Bi_2Se_3 very similar to the Bi_2Se_3/hBN/Bi_2Se_3 case. As the chemical composition of the films on the top and the bottom sides are completely different in this case, we carried out chemical compositional analysis using STEM equipped with EDS as shown in Figures 5.4(b)–(d). The STEM image (Figure 5.4(b)), the corresponding STEM–EDS mapping of each element (Figure 5.4(d)), and the STEM image overlapped with the EDS map (Figure 5.4(c)) display the spatial distribution of Sb, Te, Bi, and Se. Signals from Sb and Te were observed only above the hBN layer while Bi and Se were detected only below the hBN layer, revealing the clear spatial separation of Sb_2Te_3 and Bi_2Se_3 across the hBN barrier thanks to the highly directional nature of the MBE growth and the excellent chemical stability of hBN atomic layers. All the microstructural features described above indicate that Sb_2Te_3 and Bi_2Se_3 thin films grown on the top and bottom sides of the suspended hBN are of high structural quality.

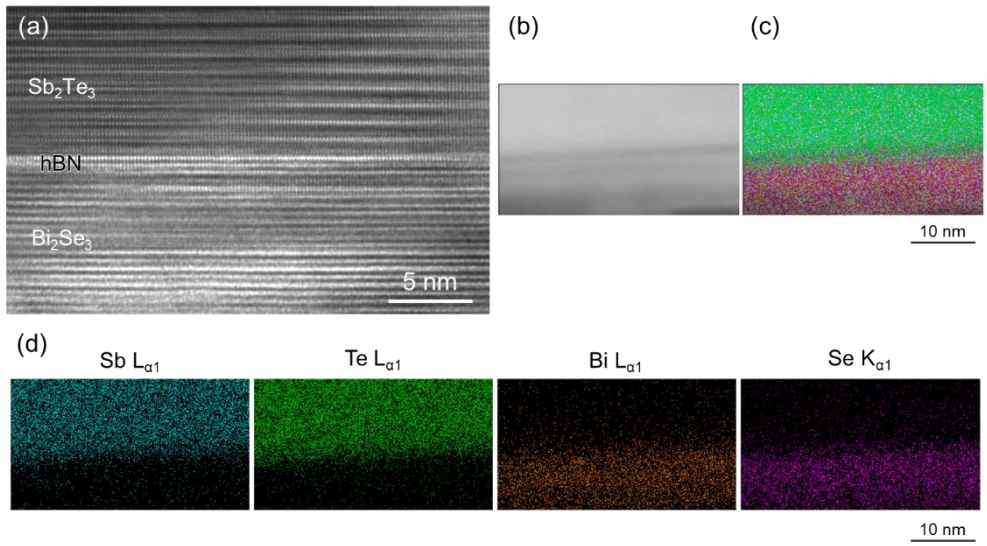

Figure 5.4 (a) Cross-sectional TEM images of Sb_2Te_3/hBN/Bi_2Se_3 suspended epitaxial vdW heterostructures. (b) STEM and (c) STEM image overlapped with EDS map. (d) Distribution maps of individual elements.

5.4 Magneto-Tunneling Spectroscopy of TI/hBN/TI Junctions

Electron tunneling properties between two epitaxially aligned TIs separated by a few atomic layers thick hBN barrier were investigated by fabricating electrical contacts to the suspended TI/hBN/TI heterostructures and measuring their current–voltage (*I*–*V*) characteristics and differential conductance (d*I*/d*V*) under in-plane and out-of-plane magnetic fields. Vertical tunneling devices with two-probe geometry were fabricated by e-beam lithography and plasma etching with Ti/Au electrodes (see Section 3.4.2 for detailed device fabrication steps). Typical junction size was nominally 200 – 300 nm in diameter defined by the circular hole made in the SiN_x membrane. The thickness of hBN tunnel barriers was chosen to be 3 or 4 MLs as they gave us comfortable currents and current densities at the range of bias voltages of interest. If thinner hBN was utilized, the current density was too high that the junction got burnt easily, while thicker hBN resulted in too low tunneling currents and noisier signals. Here, we prepared and compared the two types of tunneling junctions, Bi_2Se_3/hBN/Bi_2Se_3 and Sb_2Te_3/hBN/Bi_2Se_3, which naturally form *n*-TI/hBN/*n*-TI and *p*-TI/hBN/*n*-TI junctions, respectively, for a comprehensive study of the physics of resonant tunneling between TSSs. We note that we can hardly tune the chemical potential of TSSs at the TI/hBN/TI interface using conventional gate electrodes deposited on top or bottom of the junction due to the short electric field screening length of Bi_2Se_3 and Sb_2Te_3 [69,70].

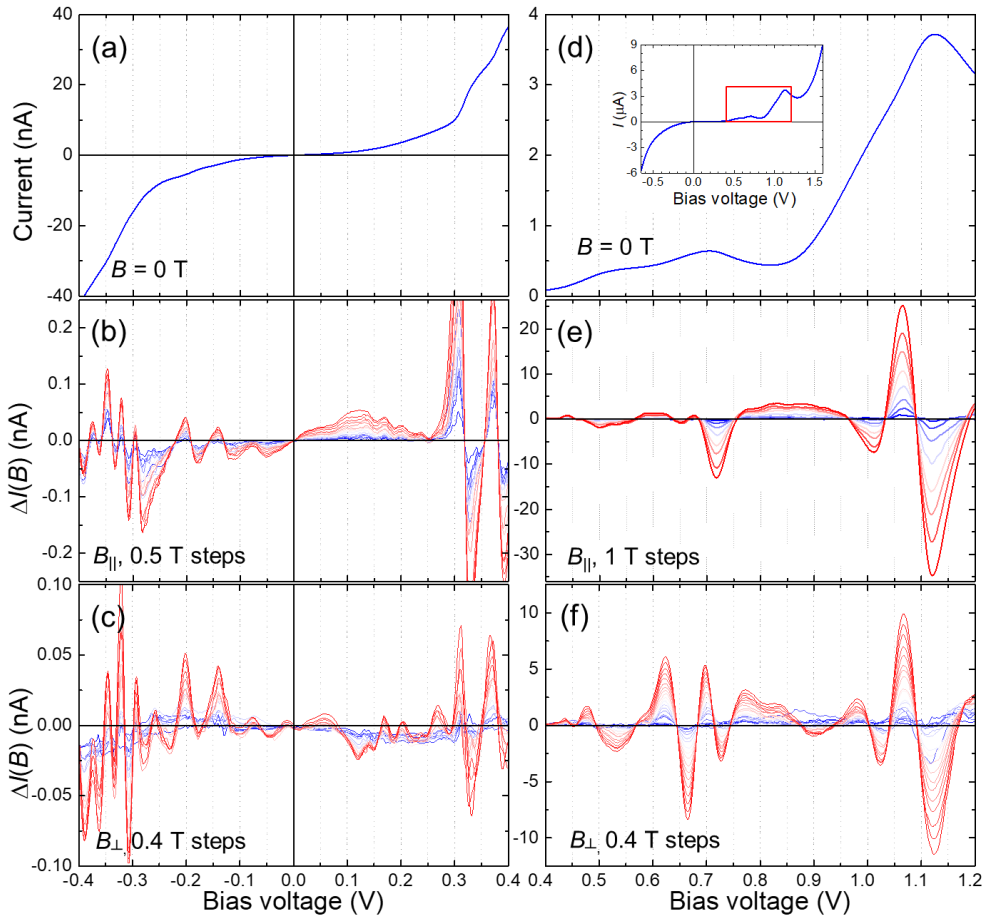

Figure 5.5 Magneto-tunneling properties of (a)–(c) Bi_2Se_3/4 ML hBN/Bi_2Se_3 and (d)–(f) Sb_2Te_3/3 ML hBN/Bi_2Se_3 devices measured at 1.5 K. (a) and (d) *I*–*V* characteristics at $B = 0$. Bias voltage range indexed by the red box in the inset of (d) is plotted in the main panel. Change in the current $\Delta I(B) = I(B) - I(B = 0)$ under (b) and (c) in-plane and (e) and (f) out-of-plane magnetic fields from 0 T (blue) to 8 T (red) with increments written in each panel.

Figures 5.5(a) and (d) show the *I*–*V* characteristics of Bi_2Se_3/4 ML hBN/Bi_2Se_3 and Sb_2Te_3/3 ML hBN/Bi_2Se_3 junctions, respectively, measured at 1.5 K and zero magnetic field. The Bi_2Se_3/hBN/Bi_2Se_3 device exhibited symmetric behaviors for both positive and negative bias voltages, and the Sb_2Te_3/hBN/Bi_2Se_3 device showed an asymmetric diode-like *I*–*V* curve (see the inset of Figure 5.5(d) for the full range of data). Given that the bias voltage *V* was applied to the top electrode (Sb_2Te_3 for the latter), these observations support the formation of *n*–*n* and *p*–*n* tunneling junctions for the former and the latter cases, respectively. In the Bi_2Se_3/hBN/Bi_2Se_3 device, the absolute value of current slowly increases until $|V| = 0.2$ V after which it rapidly increases with small plateaus, presumably due to the participation of topologically trivial quantum well states or bulk states in the tunneling process at higher bias voltages [23,93,94]. On the other hand, in the positive bias regions of the Sb_2Te_3/hBN/Bi_2Se_3 device, there exist two small peaks at a low bias followed by a weak negative differential resistance (NDR) and a large peak followed by a strong NDR at higher bias. The smaller features at lower bias voltages around 0.72 V, located in the middle of the current shoot-ups in both positive and negative directions, can be attributed to the resonant tunneling between the two TSSs, while the latter at higher bias around 1.13 V with a high amplitude is most likely due to the quantum well states or bulk states [95,96].

To understand the tunneling processes in the junctions in detail, we applied magnetic field parallel (in-plane) and perpendicular (out-of-plane) to the TI/hBN/TI layers. The filed-modulated components of the tunneling current, $\Delta I(B) = I(B) - I(B = 0)$, are plotted in Figures 5.5(b), (c), (e), and (f) to clearly display the effect of magnetic fields. For both Bi_2Se_3/hBN/Bi_2Se_3 and Sb_2Te_3/hBN/Bi_2Se_3 junctions, oscillatory spectral features at high bias voltages of $V < -0.15$ V and 0.2 V < V for the former and 1.0 V < V for the latter appear both in the in-plane and the out-of-plane magnetic field data with very similar peak positions and field dependencies. We attribute these high-bias features to the bulk states based on their insensitiveness to the field direction, which is a typical 3D nature [72,77], and their peak positions at relatively high bias voltages. These observations further support the zero-field data that the tunneling between two TSSs is expected to take place at the bias smaller than those bias voltage ranges.

In contrast to those high-bias features, the tunneling currents of the Bi_2Se_3/hBN/Bi_2Se_3 (Sb_2Te_3/hBN/Bi_2Se_3) device at bias voltages around 0.12 V (0.72 V) show dissimilar behavior depending on the direction of the field; the currents are enhanced (suppressed) in the presence of high in-plane magnetic fields, while they exhibit oscillatory spectra in the vicinity of the corresponding bias voltages under out-of-plane fields. A magnetic field applied perpendicular to the TI/hBN/TI interfaces leads to the formation of Landau levels in the interfacial TSSs, which can be proved by the observation

of oscillatory peaks developing against the out-of-plane magnetic field and bias voltages in the tunneling conductance [42,46,61,97]. On the other hand, the in-plane magnetic field — perpendicular to the direction of the tunneling current — affects the momentum conservation conditions of tunneling electrons, which has the opposite effects for the two different types of topological tunnel junctions, as discussed in detail in later sections.

The tunneling processes in the momentum space for *n*-TI/hBN/*n*-TI and *p*-TI/hBN/*n*-TI junctions are illustrated in Figure 5.6. Since the top TSSs of the bottom TI and the bottom TSSs of the top TI, the two TSSs interfaced to each other across the hBN tunnel barrier, have opposite surface normal directions, they have opposite spin helicities as depicted by red and blue arrows. Therefore, even if both energy and momentum of the two TSSs can be matched by the alignment of the two Dirac points at a certain bias V (Figure 5.6(a)), electrons cannot tunnel directly between the two TSSs due to their opposite spin orientations. The energy-momentum-spin conserved tunneling conditions only exist at the intersection of the upper Dirac cone of one TI and the lower Dirac cone of the other (Figure 5.6(b)). The electron tunneling at this situation, accordingly, cannot be observed when the Fermi levels of the two TIs both lie in the upper Dirac cones as in the case of *n*-Bi_2Se_3/hBN/*n*-Bi_2Se_3, while it can be achieved in *p*-Sb_2Te_3/hBN/*n*-Bi_2Se_3 at a finite positive bias voltage (applied to Sb_2Te_3) even though the Fermi velocities of Sb_2Te_3 and Bi_2Se_3 are not the same. We note that the tunneling scenario in our system

is inherently immune to a crystallographic orientation mismatch not only because the top and the bottom TIs are epitaxially grown, but also the Dirac points of Sb_2Te_3 and Bi_2Se_3 are located at the Γ point whose crystal momentum is zero [15]. It is in sharp contrast to graphene/hBN/graphene vertical tunneling transistors where the resonant tunneling conditions are extremely sensitive to any small misalignment between the two graphene layers formed during the stacking process as the Dirac points of graphene lie at *K* and *K*' points [45-47].

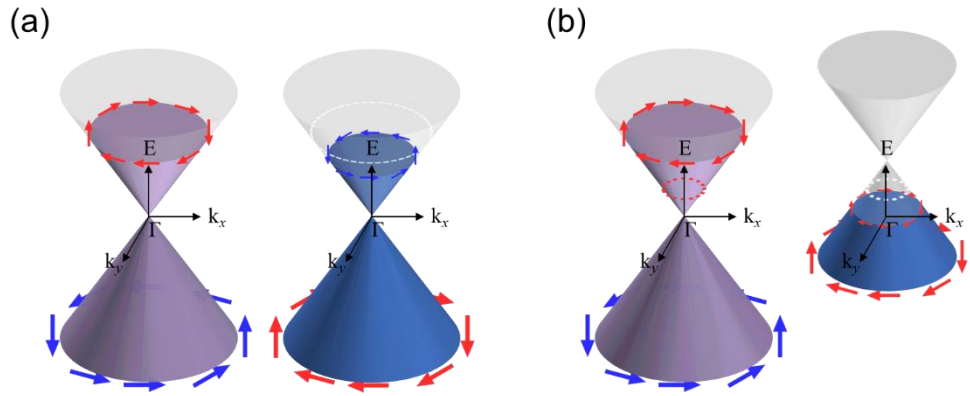

Figure 5.6 Energy-momentum-spin conserved tunneling conditions for (a) *n*-TI/hBN/*n*-TI and (b) *p*-TI/hBN/*n*-TI junctions. The spin helicities, indicated by the red and blue arrows, of the top TSS of the bottom TI (left, purple) and the bottom TSS of the top TI (right, blue) are opposite due to their opposite surface normal directions. Note that, although the two Dirac bands are illustrated alongside each other for clarity, all Dirac points are located at the *Γ* point, which is the zero-crystal momentum point.

An applied in-plane magnetic field alters the picture by adding additional in-plane momentum to the tunneling electrons due to the action of the Lorentz force [98,99] and distorting the Dirac cones of TSSs due to the Zeeman effect [100]. The tunnel currents of *p*-TI/hBN/*n*-TI junctions in the energy-momentum-spin conserving conditions at $B = 0$ get therefore suppressed under the presence of an in-plane magnetic field, which is in good agreement with the observed decrease in the current around $V = 0.72$ V for the Sb_2Te_3/hBN/Bi_2Se_3 device (Figure 5.5(e)). On the other hand, in *n*-TI/hBN/*n*-TI junctions, the Zeeman effect acting on the two upper Dirac cones with the opposite spin helicities brings one set of the occupied/unoccupied states with the same energy and spin direction closer together in the momentum space as shown in Figure 5.7 [100]. At the same time, the tunneling electrons gain in-plane momentum boosts by the Lorentz force pointing to the same direction hence the tunnel currents in *n*-TI/hBN/*n*-TI junctions can be enhanced by the in-plane field. The modulation, however, should be subtle since the momentum gain of the electrons is calculated to be 1.6×10^{-3} Å^{-1} for a 1.3 nm-thick tunnel barrier with $B_{||} = 8$ T, and the Zeeman spin-splitting of TSSs at $B_{||} = 8$ T is in the order of 10^0 meV [101,102], which are 1–2 orders of magnitude smaller than the Fermi wave vector and the Fermi energy with respect to the Dirac point of *n*-Bi_2Se_3 [75,103]. Hence, up to $B_{||} = 8$ T, only slight and broad enhancement of the tunnel current around $V = 0.12$ V could be observed in the Bi_2Se_3/hBN/Bi_2Se_3 device rather than resonance peaks.

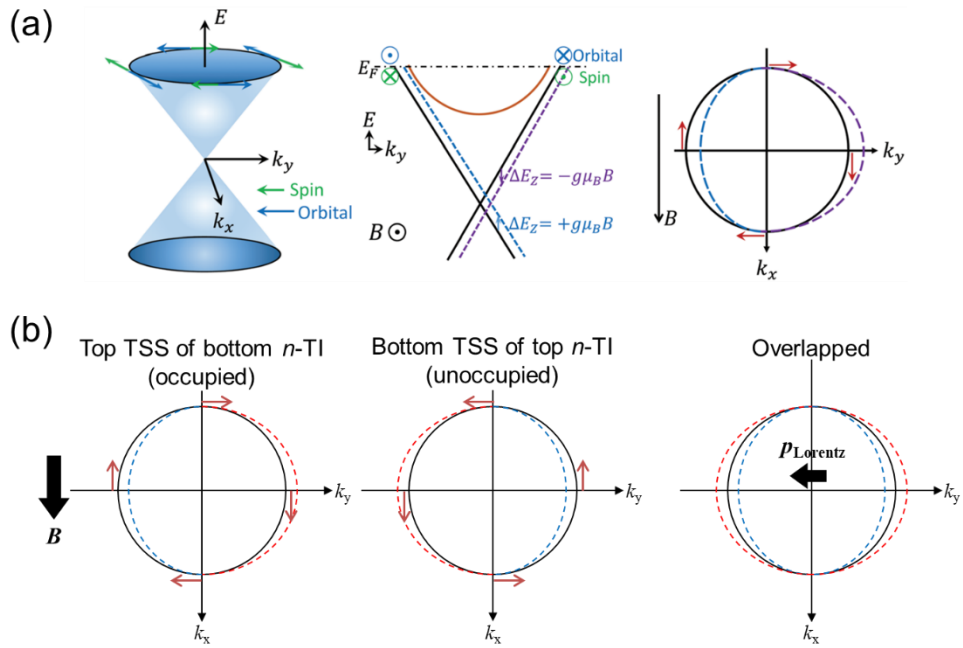

Figure 5.7 (a) Schematic illustration showing how the Zeeman effect distorts the Dirac cone, due to the in-plan spin texture of the TSS, in the presence of an in-plane magnetic field, adapted from Ref. [100]. (b) Zeeman effect acting on two *n*-type TIs (two upper Dirac cones). One set of the top and bottom TSSs get closer to each other in the momentum space. The direction of the Lorentz force acting on the tunneling electrons are depicted together.

In the presence of an out-of-plane magnetic field, the electronic states in TSSs are collected or bunched into discrete LLs. As a result of bunching, the tunneling current gets enhanced (suppressed) when LLs in the two TIs are aligned (misaligned) in energy. In particular, the formation of LLs allows us to resolve resonant tunneling between TSSs with the conservation of electron energy, momentum, and helicity through the increase in DOS at the intersection of the two Dirac cones in *p*-TI/hBN/*n*-TI junctions. Figure 5.8 shows $dI/dV(B = 0)$ of the Sb_2Te_3/hBN/Bi_2Se_3 device and its field-modulated component, $\Delta dI/dV(B) = dI/dV(B) - dI/dV(B = 0)$ at different magnetic fields B varying from 0 to 8 T with 0.4 T steps. Sets of oscillatory peaks and dips are clearly observed, with their energy spacings are in the same range with those observed in tunneling spectroscopy on *p*-Sb_2Te_3/*n*-InP junctions [61] and scanning tunneling microscopy of TIs [95,104], and thereby can potentially be attributed to the resonance between LLs developed in the two TIs. Meanwhile, in the *n*-Bi_2Se_3/hBN/*n*-Bi_2Se_3 device, the resonant tunneling under an out-of-plane magnetic field is less pronounced because of the suppressed transition between the bands with the opposite helicities and the unoccupancy of only high-index LLs (data not shown).

Here, however, the differential conductance in our device does not be converted directly into the DOS of one TSS or a simple product of the two since the two layers involved in the tunneling process both possess nontrivial DOS, unlike in a conventional tunneling spectroscopy with metallic probes

or scanning tunneling microscopy where the DOS of the probe or tip can be assumed as a constant. Moreover, the Fermi levels of the two TI layers are modulated upon a change in the bias voltage due to the capacitive charging, and the LLs of the two TIs evolve as a function of $B_{\perp}$ simultaneously but with different magnitudes due to the different Fermi velocities. Consequently, the resonant tunneling conductance spectra displayed in Figure 5.8 exhibit behaviors distinct from the energy and magnetic field dependence of LLs in TSSs, and care is needed for quantitative interpretation, which remains for future studies. A theoretical model reflecting the unique band structure of TIs and device characteristics may be a good help accounting for our data.

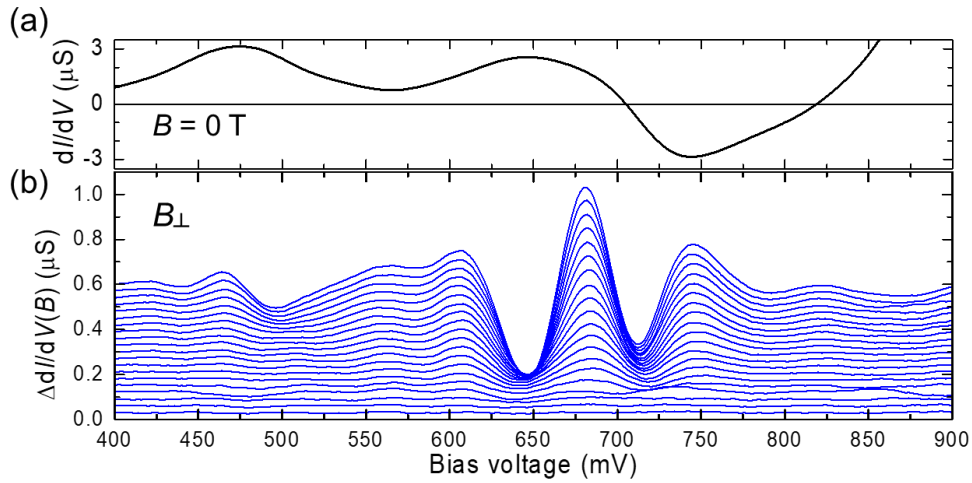

Figure 5.8 Differential conductance of the Sb_2Te_3/hBN/Bi_2Se_3 device in the presence of an out-of-plane magnetic field. (a) dI/dV(B = 0). (b) ΔdI/dV(B) = dI/dV(B) – dI/dV(B = 0) at different magnetic fields B varying from 0 to 8 T with 0.4 T steps.

5.5 Summary

We have demonstrated, by the integration of micromanipulation technique for the preparation of mesoscopic vdW device templates and MBE growth methods, vertical vdW tunnel junctions where two epitaxially aligned TIs are separated by a-few-atom-thick hBN tunnel barriers. The cross-sectional TEM investigation unambiguously revealed the heteroepitaxial relationship between the top TI, the hBN barrier, and the bottom TI and their atomically sharp and clean interfaces. Two different types of TI materials with distinct chemical compositions could also be interfaced across the ultrathin hBN barrier without chemical intermixing, allowing us to systematically investigate the selection rules for tunneling between TSSs. Tunneling spectroscopy of Sb_2Te_3/hBN/Bi_2Se_3 devices in direct comparison with Bi_2Se_3/hBN/Bi_2Se_3 devices under in-plane and out-of-plane magnetic fields showed that the helical spin texture of the TSS can play an important role in the resonant tunneling conditions, and thus it should be considered in designing TI-based vertical devices. We believe the results presented in this work paved a new way to investigate intrinsic momentum-space tunneling selection of electrons in the TSSs. Moreover, our technique can provide a versatile platform for the development of novel topological devices and, more generally, new opportunities to explore physical properties emerging at the atomically engineered commensurate heterointerfaces between various vdW layered materials.

6 Conclusions and Outlook

6.1 Concluding Remarks

In this dissertation, I have explored lateral and vertical topological electronic transport properties occurring at the atomically engineered vdW heterostructures based on TIs and hBN. To achieve such systems of high-quality, specially designed mesoscopic templates were developed; exfoliated single crystals of vdW materials were suspended using micromanipulation to the pre-made holes in the SiN_x membrane window TEM chips. Thanks to the high crystal quality, electron transparency, and mechanical strength of vdW layers, the templates were compatible with MBE growth and subsequent TEM analysis and nanofabrication processes.

I aimed for a rigorous vdW MBE by utilizing a cleaved surface of single crystal hBN, an ideal insulating vdW substrate with an atomically flat and chemically inert surface, to prepare TI materials which have a reduced defect density and high-quality vdW-interfacial electronic states. The challenges in the growth due to the weak epitaxial interactions with the substrate could be overcome by developing the two-step MBE growth. Furthermore, the mesoscopic vdW templates compatible with both MBE growth and TEM observation were especially useful to address the problem in the probing of epitaxial growth on a small sized (~10^1 μm) vdW crystals,

in which a conventional RHEED is inapplicable. By these means, it was demonstrated that high-quality Bi_2Se_3 thin films could be heteroepitaxially grown on hBN substrates with uniform and smooth surfaces and atomically sharp interfaces. The formation of high-quality TSSs at the Bi_2Se_3/hBN interface with a low carrier density and high mobility was shown by thorough electronic transport characterizations including gate- and angle-dependent magnetoresistance and Hall resistance studies, temperature- and gate-dependent weak anti-localization and Shubnikov-de Haas oscillation analyses. The growth and characterization scheme could be extended to various combinations of TI/vdW heterostructures such as Bi_2Te_3 and Sb_2Te_3 on hBN and graphene, Bi_2Se_3/WSe_2, and Bi_2Se_3/α-$RuCl_3$.

Suspension of atomically thin layers of hBN provided not only a single crystalline substrate for the heteroepitaxial growth of TI films both on and under the hBN but also the direct electrical accessibility to the interfacial electronic states by means of tunneling spectroscopy. Combined with the double-sided MBE growth, the TI/hBN/TI vertical vdW heterostructures have been realized where the two TI materials are heteroepitaxially aligned with atomically abrupt and clean interfaces with the hBN in the middle of them. Thanks to the chemical robustness of hBN atomic layers and the highly directional molecular fluxes during the MBE growth, the interfaces sealed under UHV remained intact during the integration of electrically and chemically dissimilar TI films on both sides of hBN. Vertical tunneling

devices based on the systems were fabricated to investigate the electron tunneling between the two vdW-interfacial TSSs across the a-few-atom-thick hBN, a highly crystalline and atomically planar tunnel barrier. Tunneling spectroscopy of Sb_2Te_3/hBN/Bi_2Se_3 (*p*-TI/hBN/*n*-TI) and Bi_2Se_3/hBN/Bi_2Se_3 (*n*-TI/hBN/*n*-TI) junctions under in-plane and out-of-plane magnetic fields enabled us to resolve the energy, momentum, and helical properties of the electrons tunneling between TSSs.

6.2 Suggestions for Future Works

The material systems developed in this dissertation offer attractive opportunities for investigation of a number of interesting physical phenomena, especially in terms of bringing *p*- and *n*-type TIs into close proximity beyond the hybridization limit of a single TI slab [23,95,105,106]. For example, lateral transport along the heterostructure can be employed for studying the Coulomb drag between the two TSSs [107]. From an optimistic perspective, the system can be used for building topological exciton states [108,109] and for the all-electrical control of the spin-polarized currents [110]. Meanwhile, if we shift our attention to thermal transport, our system can be utilized to investigate quantum thermoelectric effect across the vdW interfaces of topological *p*–*n* junctions [111]. Still, for the experimental realization of these intriguing proposals and their ultimate device applications, further

improvements in material quality and atomic layer-by-layer controllability of thicknesses should be preceded.

More generally, the mesoscopic vdW template developed here, which gives access to both sides of it, will serve as a versatile platform for the controlled vdW heteroepitaxial growth of various layered heterostructures that can be used for investigation of novel quantum electronic states and development of tunneling devices and functional nanodevices based on them. One such example is Josephson devices based on superconductor (SC; e.g. 2H-$NbSe_2$)/hBN or graphene/SC epitaxial vdW heterostructures. Considering the environmental sensitiveness of many vdW materials including TIs, SCs, and ferromagnets, development of experimental apparatus which integrates all of the sample preparation, material growth, structural characterization, device fabrication, and measurement in an inert condition or, desirably, in UHV will be an important task in the exploration of the systems. Lastly, as the device size was limited by the size of the highest quality single crystal available, the preparation of high-quality vdW materials in a large area by metalorganic vapor phase epitaxy (MOVPE) or MBE will be a big step forward to the realization of novel quantum electronic devices.

Appendix:
Structural and Electrical Characterizations of Bi_2Se_3 Heteroepitaxially Grown on α-$RuCl_3$

A.1 Introduction

Van der Waals heterostructures composed of various 2D layered materials are versatile platforms to explore a wide variety of interesting physical properties and device applications as the crystals held together by weak vdW forces allow us to assemble the constituents with atomic precision [1,6,7]. Topological insulators of $(Bi, Sb)_2(Te, Se)_3$ family, having vdW layered structures, have become one of the most attractive ingredients in the vdW heterostructures since they host exotic physics which have potential applications in next-generation spintronics and quantum computation [13,14]. The interplay between TIs and various classes of vdW materials ranging from graphene and hBN to 2D layered ferromagnets and superconductors have been intensively investigated through the fabrication of heterostructures with TIs, which serves as breeding grounds for novel states of matter [61,71,112-116]. Quantum spin liquids (QSLs) have also been recently brought into focus as a new topological class of material owing to their fractional fermionic excitations [117,118]. However, TI/QSL heterostructure, a stage where the two different electronic states can compete, coexist, and collaborate, has

remained experimentally unexplored yet. In this Letter, we report on the heteroepitaxial growth of Bi_2Se_3 — one of the most widely studied TIs — on α-$RuCl_3$ layers using MBE and their structural and electrical characteristics. Here, α-$RuCl_3$ is of particular interest not only because it is one of the most promising candidates for QSL experimentally suggested so far [119-123], but also because of its vdW layered structure with hexagonal in-plane lattice symmetry, the favorable crystal structure for the fabrication of vdW heterostructures with Bi_2Se_3 by means of heteroepitaxy [16,124].

A.2 Heteroepitaxial Growth of Bi_2Se_3 Thin Films on α-$RuCl_3$ using MBE

Heteroepitaxial growth is one of the most promising approaches to prepare uniform materials with well-defined structural properties. We employed an UHV-MBE system to grow high-quality Bi_2Se_3 thin films heteroepitaxially on the α-$RuCl_3$ single crystal surface. The α-$RuCl_3$ layers were prepared on SiO_2/Si substrates by mechanical exfoliation of α-$RuCl_3$ bulk single crystals *in-situ* in high vacuum. The typical lateral size of α-$RuCl_3$ crystallites ranged from several to a few tens of micrometers while the thickness was in a range of several tens of nanometers. Before Bi_2Se_3 growth, a gentle thermal cleaning was carried out at 350°C for 15 min in UHV. High purity Bi (99.999%) and Se (99.9999%) were co-evaporated by standard

Knudsen cells. The growth was performed under a high Bi to Se beam flux ratio of 1:17, and the growth rate was ~0.3 QL/min. The pressure of the MBE chamber was maintained at low 10^{-10} Torr during the growth.

We adopted the two-step growth method previously developed on hBN crystals, which enabled us to increase nucleation density on the vdW substrate without texturing of the film [32]. We first deposited the initial 2–3 QLs of Bi_2Se_3 at a low temperature of 180°C. The substrate temperature was then slowly elevated up with a rate of 5°C/min. under Se flux. At a desired higher growth temperature, the ultrathin film was annealed for 30 min, and the rest of the growth took place. The thickness of Bi_2Se_3 films investigated in this Letter is 20 QL unless otherwise mentioned.

The surface morphologies of Bi_2Se_3 thin films grown on α-$RuCl_3$ were characterized by AFM. Figures A.1(a)–(c) display AFM topography images of the films grown at different 2nd step growth temperatures. They show triangular crystal facets and terrace structures of Bi_2Se_3. The film grown at a 2nd step temperature of 300°C (Figure A.1(a)) exhibits a surface decorated with faint facets and sub-100 nm terraces. The root-mean-square (RMS) roughness value for the 2×2 μm^2 area was measured to be 0.98 nm. Elevating the 2nd step temperature to 330°C resulted in a smoother surface with the RMS roughness value of 0.59 nm (Figure A.1(b)). The crystallographic facets are also more evident, and the terraces are larger in Figure A.1(b) than in Figure A.1(a). At an even higher 2nd step temperature of 350°C (Figure A.1(c)), the

Bi_2Se_3 domains were not merged with the result that Bi_2Se_3 nanoplatelets were grown. The line profile in Figure A.1(c) displays a height step of ~20 QL between isolated Bi_2Se_3 nanoplatelets. Based on the observed growth behavior, we chose 350^{o}C as the optimal 2nd step growth temperature, which yields thin films with a uniform and flat surface morphology. The lateral size of the atomically smooth terrace, in this case, reaches several hundreds of nanometers (see the line profile in Figure A.1(b)). Meanwhile, it is smaller by a factor of 2–4 than that of Bi_2Se_3 grown on hBN at similar conditions [32], presumably due to differences in lattice constant mismatches and interactions at the interface.

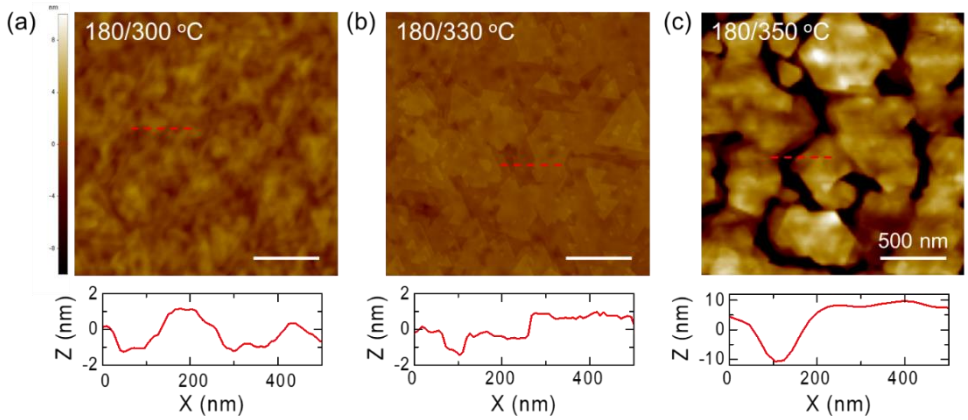

Figure A.1 AFM topography images of 20 QL Bi_2Se_3 thin films grown on α-$RuCl_3$ at different 2nd step temperatures of (a) 300°C, (b) 330°C, and (c) 350°C. Lower panels show line height profiles along the red dashed lines. Height profile in (b) clearly displays 1 QL steps of Bi_2Se_3.

A.3 Structural Characterizations of Bi_2Se_3/α-$RuCl_3$ Heterostructures

The structural characteristics of Bi_2Se_3 grown on α-$RuCl_3$ were investigated by AFM and plan-view and cross-sectional TEM. For plan-view TEM sampling, as-grown Bi_2Se_3/α-$RuCl_3$ layers were transferred onto TEM grids by PMMA spin coating followed by wet chemical etching of the sacrificial SiO_2 layer in SiO_2/Si substrates. Subsequently, the PMMA support layer was removed by acetone bath, and the sample was rinsed with IPA. Cross-sectional TEM specimen was prepared by FIB milling and low-energy focused Ar ion milling.

We investigated the heteroepitaxial relationship of Bi_2Se_3 and α-$RuCl_3$ using plan-view SAED. Figure A.2(a) is a typical SAED obtained with an aperture size of 4.1 μm. It exhibits a set of hexagonally symmetric bright spots and another hexagonal set of broadened spots accompanied by faint arc backgrounds. Based on the lattice parameter analysis, the former and the latter correspond to the single crystalline α-$RuCl_3$ substrate and the aligned Bi_2Se_3 nanocrystallites grown on top of it, respectively. As for the statistical distribution of the in-plane alignment of Bi_2Se_3 domains, the standard deviation of the SAED intensity profile of $Bi_2Se_3\{11\bar{2}0\}$ was estimated to be narrower than ±1.8° (Figure A.2(b)). The most preferential orientation of $Bi_2Se_3\{11\bar{2}0\}$ aligned parallel to α-$RuCl_3\{10\bar{1}0\}$, marked by the red arrow and the green circle in Figure A.2(a), respectively. The dispersed distribution

of the $Bi_2Se_3\{11\bar{2}0\}$ suggests deviation from the perfect epitaxial relationship, indicating the weekly bound attraction of the vdW epitaxial Bi_2Se_3/α-$RuCl_3$ heterointerface.

High-resolution TEM observation revealed the microstructural properties of the Bi_2Se_3/α-$RuCl_3$ heterostructure. Plan-view HR-TEM image in Figure A.2(c) shows clear periodic triangular patterns with a periodicity of ~1.2 nm because of the large lattice mismatch between Bi_2Se_3 and α-$RuCl_3$. These interference patterns, the Moiré fringes, have a periodicity corresponds to the double diffractions between Bi_2Se_3 $\{11\bar{2}0\}$ and α-$RuCl_3$ $\{30\bar{3}0\}$ planes — the strongest diffraction peaks of each layer (see Figure A.2(a)) — marked by the dotted blue circle in Figure A.2(a). To distinguish the lattice of each layer from this overlapped image, we reconstructed the separate lattice images through inverse FFT processing, using the two strongest sets of diffractions. The resulting image, shown in the lower left (right) inset in Figure A.3(c), reveals a lattice spacing of 0.21 (0.17) nm, agreeing well with the spacing of the $\{11\bar{2}0\}$ ($\{30\bar{3}0\}$) planes of Bi_2Se_3 (α-$RuCl_3$) which corresponds to $a_{Bi_2Se_3}/2$ ($\sqrt{3}a_{\alpha\text{-}RuCl_3}/6$) [16,124].

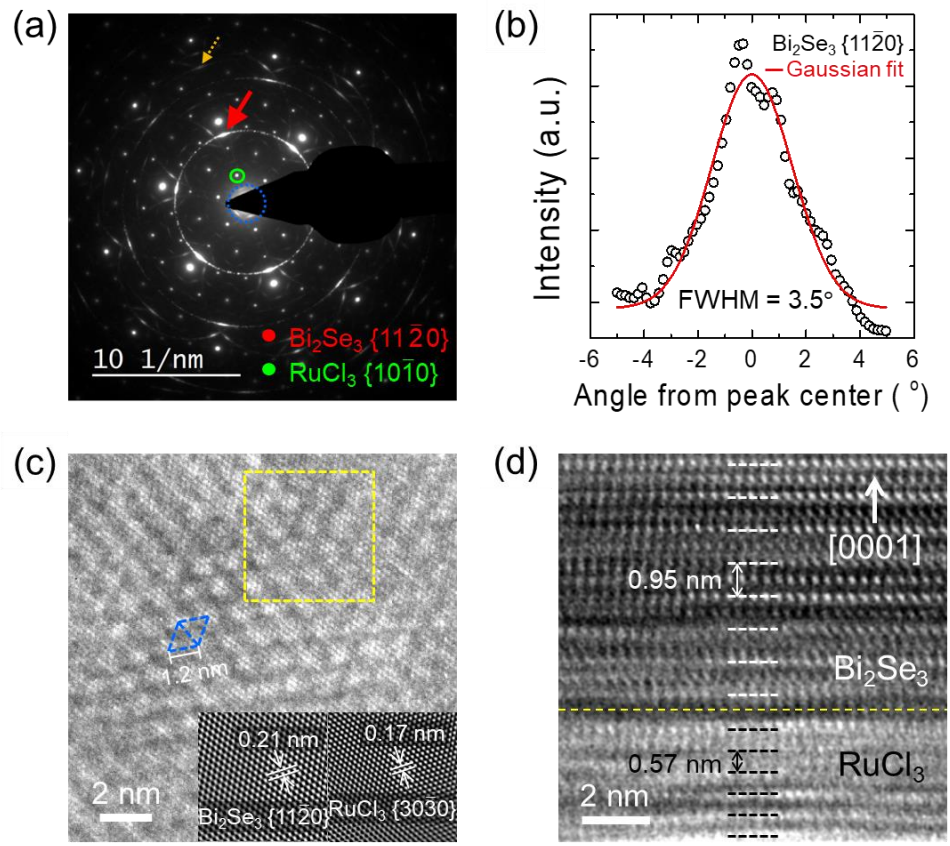

Figure A.2 Microstructural properties of Bi_2Se_3/α-$RuCl_3$ investigated by TEM. (a) SAED pattern obtained with an aperture size of 4.1 μm. (b) Intensity profile of the Bi_2Se_3 $\{11\bar{2}0\}$ diffraction and its Gaussian fit exhibiting the full width at half maximum of 3.5°. (c) Plan-view HR-TEM image of Bi_2Se_3/α-$RuCl_3$. Moiré fringes, marked by blue triangles, are clearly observed. Lower left (right) inset shows Fourier-filtered image reconstructed from Bi_2Se_3 $\{11\bar{2}0\}$ (α-$RuCl_3$ $\{30\bar{3}0\}$) set of the FFT patterns, corresponding to the area marked by the yellow square in the main figure. (d) Cross-sectional HR-TEM image of the Bi_2Se_3/α-$RuCl_3$ heterointerface taken along Bi_2Se_3 $[11\bar{2}0]$ direction. An average background subtraction filter was applied in (d) to remove noise.

Out-of-plane lattices structures of the Bi_2Se_3/α-$RuCl_3$ were examined using cross-sectional HR-TEM, as shown in Figure A.2(d). The heterointerface is unambiguously distinguished as marked by a yellow dashed line, and the vertically stacked layered structures of Bi_2Se_3 and α-$RuCl_3$ are also clearly observed. The lattice spacings between adjacent planes in Bi_2Se_3 and α-$RuCl_3$, indicated by parallel white and black dashed lines, were measured to be 0.95 and 0.57 nm, which agree well with reported *d*-spacings of Bi_2Se_3 (0003) [16] and α-$RuCl_3$ (0003) [124], respectively. The image also exhibits that the Bi_2Se_3 film is of high crystallinity from the first layer, displaying an atomically sharp interface with the underlying α-$RuCl_3$ layers. No extended crystal defects such as threading dislocations were observed at the interface. We also note, however, that α-$RuCl_3$ is extremely fragile against high-energy processes such as ion milling for cross-sectional sampling. We found that α-$RuCl_3$ is easily amorphized by the electron beam irradiation during HR imaging, making further extended and detailed cross-sectional analysis challenging.

Based on our TEM observations, we simulated a ball-and-stick lattice model to illustrate the atomic configuration of the epitaxial Bi_2Se_3/α-$RuCl_3$ heterostructure [48]. As both crystals are composed of planar layers vertically stacked through weak vdW interactions [16,124], the in-plane structures of the single layer components which form the interface are displayed (Figures A.3(a) and (b)). For the observed heteroepitaxial relationship, the in-plane

lattice periodicities of Bi_2Se_3 and α-$RuCl_3$ along $[1\bar{2}10]_{Bi_2Se_3} \parallel [1\bar{1}00]_{\alpha\text{-}RuCl_3}$ — $a_{Bi_2Se_3}$ and $\sqrt{3}a_{\alpha\text{-}RuCl_3}$, respectively — have a significant mismatch of –60% as shown in Figure A.3(c). Meanwhile, they fit almost perfectly to a small integer ratio of 2:5 with a misfit smaller than 0.1%. It is also in good agreement with the plan-view TEM observations; as marked by the orange dotted arrow in the SAED (Figure A.2(a)), a faint arc pattern originated from Bi_2Se_3 $\{22\bar{4}0\}$ is overlapped on the α-$RuCl_3$ $\{50\bar{5}0\}$ diffraction spot. Therefore, these observations strongly suggest the formation of a (5×5)–$Bi_2Se_3/(2\sqrt{3} \times 2\sqrt{3})$ $R30°$–α-$RuCl_3$ commensurate supercell which is displayed as red dotted lines in Figure A.3(c). Meanwhile, due to the unique atomic configuration of the two lattices, regular triangular Moiré patterns with a periodicity of 12.0 nm are also clearly displayed (blue dotted lines in Figure A.3(c)). This result is in close agreement with the plan-view TEM observation shown in Figure A.2(c).

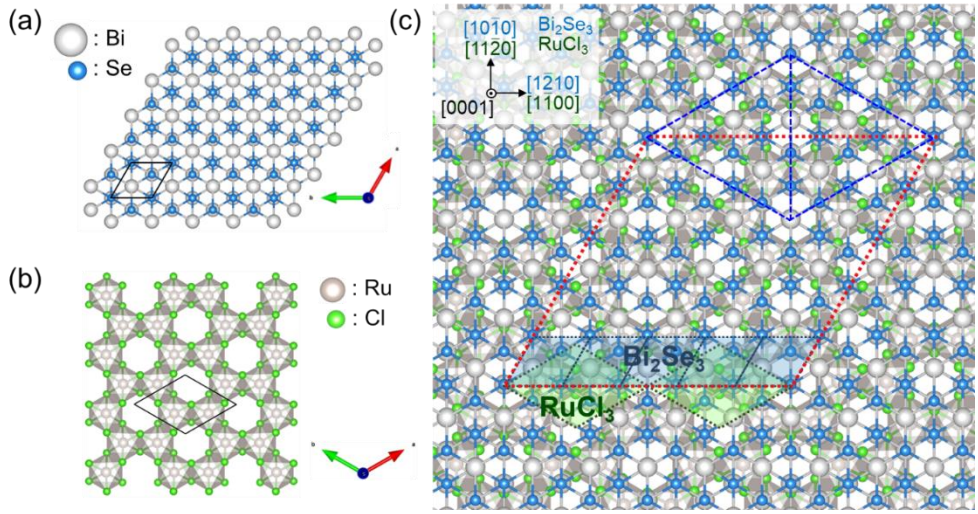

Figure A.3 Ball-and-stick model of (a) Bi_2Se_3 and (b) α-$RuCl_3$. Primitive unit cells are indicated by solid lines. (c) Epitaxial Bi_2Se_3/α-$RuCl_3$ heterostructure. The (5 × 5)–Bi_2Se_3/(2$\sqrt{3}$ × 2$\sqrt{3}$) *R*30°–α-$RuCl_3$ supercell (red dotted line), Moiré patterns (blue dotted line), and primitive unit cells of Bi_2Se_3 (blue shaded area) and α-$RuCl_3$ (green shaded area) are indicated.

Our atomic structural analysis above indicates that the two lattices spontaneously form the large-scale periodicity, whose area is an order of magnitude larger than that of unit cells, despite the substantial lattice mismatch between unit cells.The similar interfacial alignment was reported in Bi_2Se_3/hBN [32] and ZnO/hBN [50] heteroepitaxial systems where two dissimilar hexagonal lattices with large lattice mismatch are bound by vdW-type interactions. However, the 30°-rotated alignment of $[1\bar{2}10]_{Bi_2Se_3} \parallel [1\bar{1}00]_{\alpha\text{-}RuCl_3}$ is distinctly different from the parallel (0°) alignments of $[1\bar{1}00]_{Bi_2Se_3\ (ZnO)} \parallel [1\bar{1}00]_{hBN}$. Since α-$RuCl_3$, Ru^{3+} atoms in the edge-sharing $RuCl_6$ octahedra form a honeycomb network analogous to the hBN lattice (Figure A.3(b)) [55,124], the difference in the epitaxial relationship between Bi_2Se_3/α-$RuCl_3$ and Bi_2Se_3/hBN can be correlated with the commensurate (incommensurate) nature of the supercell for the former (latter) case.

A.4 Electrical Characterizations of Bi_2Se_3 Thin Films on α-$RuCl_3$ Layers

Electrical transport measurements were performed either on Hall bar or van der Pauw devices fabricated by following steps. For the first step, an array of Cr/Au 5/50 nm microdots were deposited by e-beam evaporation through stencil masks for the formation of ohmic contacts. Then HSQ layer with PMMA as a sacrificial layer was spun coated, and a negative-tone e-beam lithography was followed to pattern the HSQ layer into the desired device geometry. The PMMA layer was etched by oxygen plasma, and then the unwanted Bi_2Se_3 films were etched using Ar plasma. The PMMA and HSQ mask was removed by acetone. The second round of e-beam lithography and a subsequent e-beam evaporation of Cr/Pd/Au 5/20/125 nm were used to put down bonding pads and interconnection lines to the 1st contacts. Finally, the sample was capped by the PMMA layer while bonding pads were opened by another round of e-beam lithography. The magnetotransport measurements were carried out in a Quantum Design physical property measurement system by low-frequency AC lock-in technique with an excitation current of 500 nA.

Electrical properties of the Bi_2Se_3/α-$RuCl_3$ heterostructure were investigated by magnetotransport measurements. Figure A.4(a) shows magnetoresistance ratio (MR; $R_{xx}(B)/R_{xx}(B = 0\ \mathrm{T})$) under out-of-plane and in-plane field configurations. The out-of-plane MR exhibits positive

magnetoresistance which can potentially be assigned to the weak antilocalization in TIs [52,69,125,126]. The in-plane MR does not exhibit significant variation under high in-plane magnetic fields up to 14 T, where the transition of α-$RuCl_3$ into the QSL state might take place [127-129]. The Hall resistance $R_{xy}(B)$ measured under perpendicular magnetic fields at various temperatures exhibits linear field dependence with negative slopes (data not shown), indicating the dominance of single *n*-type conduction channel in our device. Figure A.4(b) shows the temperature dependence of sheet carrier concentration and mobility calculated from the magnetotransport data. Carrier concentration does not decrease much when the temperature is reduced, indicating full ionization of donors in the film even at low temperatures [54,130]. The very weak dependence of the mobility below T ~30 K suggests that the dominant scattering is originated from static disorders such as the Se vacancy or grain boundaries in the Bi_2Se_3 film [17,131]. Considering the relatively high carrier density [69] and that α-$RuCl_3$ alone exhibits insulating temperature-dependent resistance behavior [132,133], we attribute the dominant conduction channel to the bulk states and/or impurity bands in Bi_2Se_3. The low mobility and high carrier density of Bi_2Se_3 grown on α-$RuCl_3$, in comparison with Bi_2Se_3/hBN, can presumably be owing to its smaller terrace sizes and larger deviation in the in-plane alignment of Bi_2Se_3 grains [32].

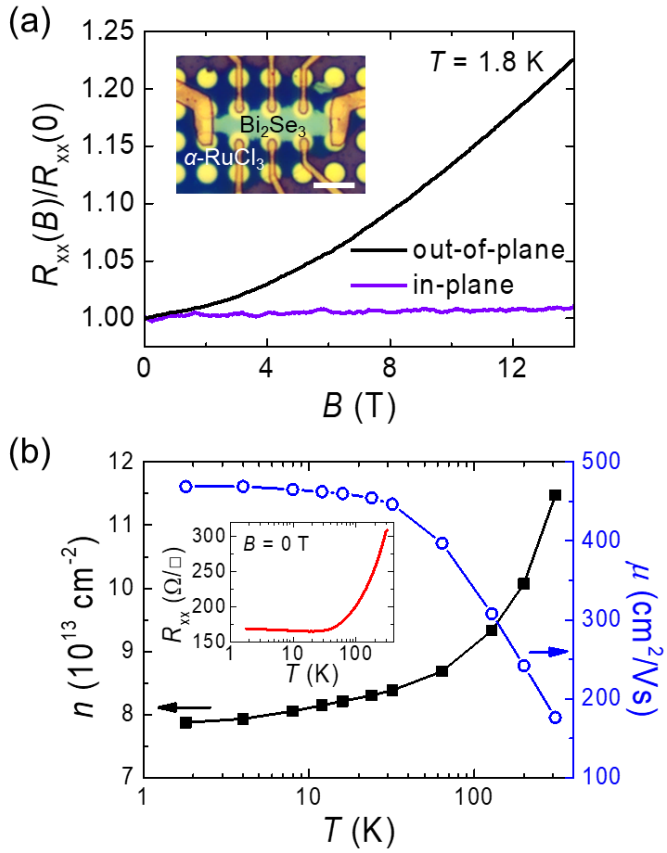

Figure A.4 Electrical transport properties of Bi_2Se_3/α-$RuCl_3$. (a) Magnetoresistance ratio under out-of-plane and in-plane magnetic field configurations at 1.8 K. Inset: Optical image of a typical Hall bar device. Scale bar: 5 μm (b) Temperature dependence of the carrier density and mobility calculated by the Hall measurement under out-of-plane fields. Inset: Temperature dependence of the resistance of Bi_2Se_3/α-$RuCl_3$ at zero magnetic field.

A.5 Summary

We have demonstrated the heteroepitaxial growth of Bi_2Se_3 thin films on α-$RuCl_3$ layers. Uniform films were prepared through optimization of the two-step MBE process. The AFM results revealed the film's atomically smooth surface morphology with the size of terraces exceeding hundreds of nanometers. We found, using TEM investigation, an epitaxial relationship of $[1\bar{2}10](0001)_{Bi_2Se_3} \parallel [1\bar{1}00](0001)_{\alpha\text{-}RuCl_3}$ with the statistical in-plane orientation distribution of ±1.8° despite a lattice mismatch of –60%, which is attributed to the weak van der Waals interaction on the interface. The most preferred orientation corresponds to the (5×5)–Bi_2Se_3/$(2\sqrt{3} \times 2\sqrt{3})$ $R30°$–α-$RuCl_3$ heteroepitaxial commensurate supercells. Magnetotransport measurement showed a dominance of *n*-type carriers, likely originated from impurity states in Bi_2Se_3, with a mobility of 470 cm^2/Vs and a density of 7.8×10^{13} cm^{-2} at 1.8 K.

List of Abbreviations

1D	One-Dimensional
2D	Two-Dimensional
2DEG	Two-Dimensional Electron Gas
3D	Three-Dimensional
AFM	Atomic Force Microscopy
ARPES	Angle-Resolved Photoemission Spectroscopy
BF	Bright Field
BOE	Buffered Oxide Etch
CAD	Computer-Aided Design
CF	ConFlat
CVD	Chemical Vapor Deposition
DI	Deionized
DOS	Density Of States
e-beam	Electron Beam
EDS	Energy Dispersive X-Ray Spectroscopy
EG	Epitaxial Graphene
FE-SEM	Field-Emission Scanning Electron Microscopy
FFT	Fast Fourier Transform
FIB	Focused Ion Beam

HAADF-STEM	High-Angle Annular Dark-Field Scanning Transmission Electron Microscopy
hBN	Hexagonal Boron Nitride
HLN	Hikami-Larkin-Nagaoka
HR	High-Resolution
HR-TEM	High-Resolution Transmission Electron Microscopy
HSQ	Hydrogen Silsesquioxane
I.D.	Inside Diameter
IPA	Isopropyl Alcohol
I–V	Current–Voltage
LL	Landau Level
MBE	Molecular Beam Epitaxy
MIBK	Methyl Isobutyl Ketone
MIF	Metal Ion Free
ML	Monolayer
MOVPE	Metalorganic Vapor Phase Epitaxy
NCRIF	National Center for Inter-university Research Facilities
NDR	Negative Differential Resistance
NPGS	Nanometer Pattern Generation System
O.D.	Outside Diameter
OFHC	Oxygen Free High Conductivity
PC	Polycarbonate

PCL	Polycaprolactone
PDMS	Polydimethylsiloxane
PMMA	Poly(Methyl Methacrylate)
PPC	Polypropylene Carbonate
PPMS	Physical Property Measurement System
PVA	Poly(Vinyl Alcohol)
QCM	Quartz Crystal Microbalance
QHE	Quantum Hall Effect
QL	Quintuple Layer
QSL	Quantum Spin Liquid
RHEED	Reflection High-Energy Electron Diffraction
RIE	Reactive Ion Etching
RMS	Root-Mean-Square
SAED	Selected-Area Electron Diffraction
SC	Superconductor
SCR	Silicon Controlled Rectifier
SdH	Shubnikov-de Haas
SEM	Scanning Electron Microscopy
SOC	Spin-Orbit Coupling
STEM	Scanning Transmission Electron Microscopy
STM	Scanning Tunneling Microscopy
STS	Scanning Tunneling Spectroscopy

TEM	Transmission Microscopy
THF	Tetrahydrofuran
TI	Topological Insulator
TMAH	Tetramethylammonium Hydroxide
TMD	Transition Metal Dichalcogenide
TSS	Topological Surface State
UHV	Ultra-High Vacuum
UHV-MBE	Ultra-High Vacuum Molecular Beam Epitaxy
vdW	van der Waals
WAL	Weak Anti-Localization

Bibliography

[1] P. Ajayan, P. Kim, and K. Banerjee, Phys. Today **69**, 38 (2016).

[2] S. Z. Butler *et al.*, ACS Nano **7**, 2898 (2013).

[3] Q. H. Wang, K. Kalantar-Zadeh, A. Kis, J. N. Coleman, and M. S. Strano, Nat. Nanotechnol. **7**, 699 (2012).

[4] Y. Saito, T. Nojima, and Y. Iwasa, Nat. Rev. Mater. **2**, 16094 (2016).

[5] L. Kou, Y. Ma, Z. Sun, T. Heine, and C. Chen, J. Phys. Chem. Lett. **8**, 1905 (2017).

[6] A. K. Geim and I. V. Grigorieva, Nature **499**, 419 (2013).

[7] K. S. Novoselov, A. Mishchenko, A. Carvalho, and A. H. Castr o Neto, Science **353**, aac9439 (2016).

[8] Y. Tokura, M. Kawasaki, and N. Nagaosa, Nat. Phys. **13**, 1056 (2017).

[9] K. He and Q.-K. Xue, Natl. Sci. Rev. **6**, 202 (2018).

[10] R. Frisenda, E. Navarro-Moratalla, P. Gant, D. Pérez De Lara, P. Jarillo-Herrero, R. V. Gorbachev, and A. Castellanos-Gomez, C hem. Soc. Rev. **47**, 53 (2018).

[11] J. Yu, J. Li, W. Zhang, and H. Chang, Chem. Sci. **6**, 6705 (20 15).

[12] F. D. M. Haldane, Rev. Mod. Phys. **89**, 040502 (2017).

[13] M. Z. Hasan and C. L. Kane, Rev. Mod. Phys. **82**, 3045 (2010).

[14] X.-L. Qi and S.-C. Zhang, Rev. Mod. Phys. **83**, 1057 (2011).

[15] H. Zhang, C.-X. Liu, X.-L. Qi, X. Dai, Z. Fang, and S.-C. Zha ng, Nat. Phys. **5**, 438 (2009).

[16] S. Nakajima, J. Phys. Chem. Solids **24**, 479 (1963).

[17] Y. Liu, Y. Li, S. Rajput, D. Gilks, L. Lari, P. Galindo, M. Wei nert, V. Lazarov, and L. Li, Nat. Phys. **10**, 294 (2014).

[18] M. Brahlek, N. Koirala, M. Salehi, N. Bansal, and S. Oh, Phys. Rev. Lett. **113**, 026801 (2014).

[19] N. Koirala *et al.*, Nano Lett. **15**, 8245 (2015).

[20] A. Koma, Thin Solid Films **216**, 72 (1992).

[21] P. Gehring, B. F. Gao, M. Burghard, and K. Kern, Nano Lett. **1 2**, 5137 (2012).

[22] M. Henini, *Molecular beam epitaxy: from research to mass prod uction* (Newnes, 2012).

[23] K. He *et al.*, Nat. Phys. **6**, 584 (2010).

[24] C.-L. Song *et al.*, Appl. Phys. Lett. **97**, 143118 (2010).

[25] Y. Liu, M. Weinert, and L. Li, Phys. Rev. Lett. **108**, 115501 (2 012).

[26] K. V. Emtsev *et al.*, Nat. Mater. **8**, 203 (2009).

[27] H. Kuramochi, S. Odaka, K. Morita, S. Tanaka, H. Miyazaki, M. V. Lee, S. L. Li, H. Hiura, and K. Tsukagoshi, AIP Adv. **2**, 0 12115 (2012).

[28] M. Salehi, H. Shapourian, I. T. Rosen, M. G. Han, J. Moon, P. Shibayev, D. Jain, D. Goldhaber-Gordon, and S. Oh, Adv. Mate r., e1901091 (2019).

[29] K. Wang *et al.*, Appl. Phys. Lett. **103** (2013).

[30] C. Zhang, X. Yuan, K. Wang, Z. G. Chen, B. Cao, W. Wang, Y. Liu, J. Zou, and F. Xiu, Adv. Mater. **26**, 7110 (2014).

[31] W. H. Chae, J. D. Cain, E. D. Hanson, A. A. Murthy, and V. P. Dravid, Appl. Phys. Lett. **111**, 143106 (2017).

[32] J. Y. Park *et al.*, 2D Mater. **3**, 035029 (2016).

[33] C. R. Dean *et al.*, Nat. Nanotechnol. **5**, 722 (2010).

[34] C.-H. Lee *et al.*, Adv. Mater. **26**, 2812 (2014).

[35] X. Cui *et al.*, Nat. Nanotechnol. **10**, 534 (2015).

[36] D. R. Hickey *et al.*, arXiv:1808.03719 [cond-mat.mtrl-sci] (201

8).

[37] K. Watanabe, T. Taniguchi, and H. Kanda, Nat. Mater. **3**, 404 (2004).

[38] A. Pakdel, Y. Bando, and D. Golberg, Chem. Soc. Rev. **43**, 934 (2014).

[39] L. Wang *et al.*, Science **342**, 614 (2013).

[40] G.-H. Lee, Y.-J. Yu, C. Lee, C. Dean, K. L. Shepard, P. Kim, and J. Hone, Appl. Phys. Lett. **99** (2011).

[41] L. Britnell *et al.*, Nano Lett. **12**, 1707 (2012).

[42] S. Jung *et al.*, Nano Lett. **17**, 206 (2017).

[43] L. Britnell *et al.*, Science **335**, 947 (2012).

[44] L. Britnell, R. V. Gorbachev, A. K. Geim, L. A. Ponomarenko, A. Mishchenko, M. T. Greenaway, T. M. Fromhold, K. S. Novo selov, and L. Eaves, Nat. Commun. **4**, 1794 (2013).

[45] A. Mishchenko *et al.*, Nat. Nanotechnol. **9**, 808 (2014).

[46] M. T. Greenaway *et al.*, Nat. Phys. **11**, 1057 (2015).

[47] J. R. Wallbank *et al.*, Science **353**, 575 (2016).

[48] K. Momma and F. Izumi, J. Appl. Cryst. **44**, 1272 (2011).

[49] J. Jo, H. Yoo, S. I. Park, J. B. Park, S. Yoon, M. Kim, and G. -C. Yi, Adv. Mater. **26**, 2011 (2014).

[50] H. Oh, Y. J. Hong, K.-S. Kim, S. Yoon, H. Baek, S.-H. Kang, Y.-K. Kwon, M. Kim, and G.-C. Yi, NPG Asia Mater. **6**, e145 (2014).

[51] Y. Xia *et al.*, Nat. Phys. **5**, 398 (2009).

[52] J. G. Checkelsky, Y. S. Hor, R. J. Cava, and N. P. Ong, Phys. Rev. Lett. **106**, 196801 (2011).

[53] D. Kim, S. Cho, N. P. Butch, P. Syers, K. Kirshenbaum, S. Ad am, J. Paglione, and M. S. Fuhrer, Nat. Phys. **8**, 459 (2012).

[54] H. D. Li *et al.*, New J. Phys. **12**, 103038 (2010).

[55] R. S. Pease, Nature **165**, 722 (1950).

[56] L. He *et al.*, J. Appl. Phys. **109**, 103702 (2011).

[57] A. Richardella, D. M. Zhang, J. S. Lee, A. Koser, D. W. Rench, A. L. Yeats, B. B. Buckley, D. D. Awschalom, and N. Samart h, Appl. Phys. Lett. **97**, 262104 (2010).

[58] S. Schreyeck *et al.*, Appl. Phys. Lett. **102**, 041914 (2013).

[59] G. Zhang, H. Qin, J. Chen, X. He, L. Lu, Y. Li, and K. Wu, Adv. Funct. Mater. **21**, 2351 (2011).

[60] A. A. Taskin, S. Sasaki, K. Segawa, and Y. Ando, Adv. Mater. **24**, 5581 (2012).

[61] R. Yoshimi, A. Tsukazaki, K. Kikutake, J. G. Checkelsky, K. S. Takahashi, M. Kawasaki, and Y. Tokura, Nat. Mater. **13**, 253 (2014).

[62] K.-H. Jin and S.-H. Jhi, Phys. Rev. B **87**, 075442 (2013).

[63] L. Kou, B. Yan, F. Hu, S. C. Wu, T. O. Wehling, C. Felser, C. Chen, and T. Frauenheim, Nano Lett. **13**, 6251 (2013).

[64] J. Zhang, C. Triola, and E. Rossi, Phys. Rev. Lett. **112**, 096802 (2014).

[65] W. Dang, H. Peng, H. Li, P. Wang, and Z. Liu, Nano Lett. **10**, 2870 (2010).

[66] F. A. Ponce, J. S. Major, W. E. Plano, and D. F. Welch, Appl. Phys. Lett. **65**, 2302 (1994).

[67] N. Grandjean, J. Massies, P. Vennéguès, M. Laügt, and M. Lero ux, Appl. Phys. Lett. **70**, 643 (1997).

[68] N. W. Ashcroft and N. D. Mermin, *Solid State Physics* (Holt, R inehart and Winston, New York, 1976).

[69] M. Brahlek, N. Koirala, N. Bansal, and S. Oh, Solid State Com mun. **215-216**, 54 (2015).

[70] W. Richter, H. Köhler, and C. R. Becker, phys. stat. sol. (b) **84**, 619 (1977).

[71] L. D. Alegria, H. Ji, N. Yao, J. J. Clarke, R. J. Cava, and J. R.

Petta, Appl. Phys. Lett. **105**, 053512 (2014).

[72] J. Lee, J. Park, J.-H. Lee, J. S. Kim, and H.-J. Lee, Phys. Rev. B **86**, 245321 (2012).

[73] Y. Xu *et al.*, Nat. Phys. **10**, 956 (2014).

[74] N. Bansal, Y. S. Kim, M. Brahlek, E. Edrey, and S. Oh, Phys. Rev. Lett. **109**, 116804 (2012).

[75] L. He *et al.*, Nano Lett. **12**, 1486 (2012).

[76] D. Kong *et al.*, ACS Nano **5**, 4698 (2011).

[77] J. J. Cha, D. Kong, S. S. Hong, J. G. Analytis, K. Lai, and Y. Cui, Nano Lett. **12**, 1107 (2012).

[78] S. Hikami, A. I. Larkin, and Y. Nagaoka, Prog. Theor. Phys. **63**, 707 (1980).

[79] Y. Zhang, Y. W. Tan, H. L. Stormer, and P. Kim, Nature **438**, 201 (2005).

[80] A. A. Taskin and Y. Ando, Phys. Rev. B **84**, 035301 (2011).

[81] L. Hongchao, L. Shiguang, Y. Ya, H. Hongtao, and W. Jiannon g, 2D Mater. **2**, 045002 (2015).

[82] D. Shoenberg, *Magnetic oscillations in metals* (Cambridge univer sity press, 2009).

[83] Y. S. Kim *et al.*, Phys. Rev. B **84**, 073109 (2011).

[84] A. Kandala, A. Richardella, D. Zhang, T. C. Flanagan, and N. S amarth, Nano Lett. **13**, 2471 (2013).

[85] S. Matsuo *et al.*, Phys. Rev. B **85**, 075440 (2012).

[86] A. A. Taskin, S. Sasaki, K. Segawa, and Y. Ando, Phys. Rev. Lett. **109**, 066803 (2012).

[87] J. Zhang *et al.*, Nat. Commun. **2**, 574 (2011).

[88] D. Kong *et al.*, Nat. Nanotechnol. **6**, 705 (2011).

[89] C.-Z. Chang *et al.*, Science **340**, 167 (2013).

[90] A. Kuc, N. Zibouche, and T. Heine, Phys. Rev. B **83**, 245213 (2011).

[91] W. S. Yun, S. W. Han, S. C. Hong, I. G. Kim, and J. D. Lee, Phys. Rev. B **85**, 033305 (2012).

[92] D. R. Klein *et al.*, Science **360**, 1218 (2018).

[93] Y. Liu, Y. Y. Li, D. Gilks, V. K. Lazarov, M. Weinert, and L. Li, Phys. Rev. Lett. **110** (2013).

[94] H. Steinberg, L. A. Orona, V. Fatemi, J. D. Sanchez-Yamagishi, K. Watanabe, T. Taniguchi, and P. Jarillo-Herrero, Phys. Rev. B **92** (2015).

[95] Y. Jiang *et al.*, Phys. Rev. Lett. **108**, 016401 (2012).

[96] S. Zhu *et al.*, Sci. Rep. **5**, 13213 (2015).

[97] L. Zhang, Y. Yan, H. C. Wu, D. Yu, and Z. M. Liao, ACS Na no **10**, 3816 (2016).

[98] R. K. Hayden, D. K. Maude, L. Eaves, E. C. Valadares, M. He nini, F. W. Sheard, O. H. Hughes, J. C. Portal, and L. Cury, P hys. Rev. Lett. **66**, 1749 (1991).

[99] V. I. Fal'ko and S. V. Meshkov, Semicond. Sci. Technol. **6**, 196 (1991).

[100] L.-X. Wang, Y. Yan, L. Zhang, Z.-M. Liao, H.-C. Wu, and D.-P. Yu, Nanoscale **7**, 16687 (2015).

[101] Z. Zhang *et al.*, Phys. Rev. B **92**, 235402 (2015).

[102] Y.-S. Fu, T. Hanaguri, K. Igarashi, M. Kawamura, M. S. Bahra my, and T. Sasagawa, Nat. Commun. **7**, 10829 (2016).

[103] M. Bianchi, D. Guan, S. Bao, J. Mi, B. B. Iversen, P. D. C. Ki ng, and P. Hofmann, Nat. Commun. **1**, 128 (2010).

[104] P. Cheng *et al.*, Phys. Rev. Lett. **105**, 076801 (2010).

[105] H. Jin, J. Im, J.-H. Song, and A. J. Freeman, Phys. Rev. B **85** (2012).

[106] Y. Y. Li *et al.*, Adv. Mater. **22**, 4002 (2010).

[107] X. Liu *et al.*, Phys. Rev. Lett. **119**, 056802 (2017).

[108] B. Seradjeh, J. E. Moore, and M. Franz, Phys. Rev. Lett. **103**, 066402 (2009).

[109] X. Liu, K. Watanabe, T. Taniguchi, B. I. Halperin, and P. Kim, Nat. Phys. **13**, 746 (2017).

[110] O. V. Yazyev, J. E. Moore, and S. G. Louie, Phys. Rev. Lett. **105**, 266806 (2010).

[111] Y. Xu, Z. Gan, and S.-C. Zhang, Phys. Rev. Lett. **112**, 226801 (2014).

[112] F. Katmis *et al.*, Nature **533**, 513 (2016).

[113] H. Wang *et al.*, Phys. Rev. Lett. **117**, 076601 (2016).

[114] M.-X. Wang *et al.*, Science **336**, 52 (2012).

[115] Q. L. He *et al.*, Science **357**, 294 (2017).

[116] H.-H. Sun and J.-F. Jia, npg Quantum Mater. **2**, 34 (2017).

[117] A. Kitaev, Ann. Phys. **321**, 2 (2006).

[118] L. Savary and L. Balents, Rep. Prog. Phys. **80**, 016502 (2017).

[119] K. W. Plumb, J. P. Clancy, L. J. Sandilands, V. V. Shankar, Y. F. Hu, K. S. Burch, H.-Y. Kee, and Y.-J. Kim, Phys. Rev. B **90**, 041112 (2014).

[120] A. Banerjee *et al.*, Nat. Mater. **15**, 733 (2016).

[121] D. Weber, L. M. Schoop, V. Duppel, J. M. Lippmann, J. Nuss, and B. V. Lotsch, Nano Lett. **16**, 3578 (2016).

[122] M. Ziatdinov *et al.*, Nat. Commun. **7**, 13774 (2016).

[123] R. D. Johnson *et al.*, Phys. Rev. B **92**, 235119 (2015).

[124] E. V. Stroganov and K. V. Ovchinnikov, Vestnik. Leningrad. Un iv., Ser. Fiz. i Khim. Ser. Fiz. i Khim. **12**, 152 (1957).

[125] J. Chen *et al.*, Phys. Rev. Lett. **105**, 176602 (2010).

[126] J. Tian, C. Chang, H. Cao, K. He, X. Ma, Q. Xue, and Y. P.

Chen, Sci. Rep. **4**, 4859 (2014).

[127] I. A. Leahy, C. A. Pocs, P. E. Siegfried, D. Graf, S. H. Do, K. -Y. Choi, B. Normand, and M. Lee, Phys. Rev. Lett. **118**, 1872 03 (2017).

[128] S. H. Baek, S. H. Do, K. Y. Choi, Y. S. Kwon, A. U. B. Wolt er, S. Nishimoto, J. van den Brink, and B. Büchner, Phys. Rev. Lett. **119**, 037201 (2017).

[129] J. A. Sears, Y. Zhao, Z. Xu, J. W. Lynn, and Y.-J. Kim, Phys. Rev. B **95**, 180411 (2017).

[130] J. Son, K. Banerjee, M. Brahlek, N. Koirala, S.-K. Lee, J.-H. A hn, S. Oh, and H. Yang, Appl. Phys. Lett. **103**, 213114 (2013).

[131] C. Mann, D. West, I. Miotkowski, Y. P. Chen, S. Zhang, and C. -K. Shih, Nat. Commun. **4**, 2277 (2013).

[132] A. Little *et al.*, Phys. Rev. Lett. **119**, 227201 (2017).

[133] S. Mashhadi, D. Weber, L. M. Schoop, A. Schulz, B. V. Lotsch, M. Burghard, and K. Kern, Nano Lett. **18**, 3203 (2018).

Abstract in Korean (국문초록)

최근 반데르발스 물질군에 위상절연체(topological insulator; TI)라는 새로운 전자 구조를 띠는 물질이 포함됨에 따라, 반데르발스 이종구조에 대한 연구가 더욱 활기를 띠고 있다. 고품질의 위상학적 반데르발스 이종구조를 제조하기 위해서는 결함 밀도를 낮추고 계면을 원자수준으로 제어하는 것이 필수적이다. 그러나 지금까지 이에 대한 많은 연구가 있었음에도, 고도로 제어된 환경에서의 소재 성장, 새로운 특성 분석 기법, 소자제조 공정에 대한 연구가 여전히 필요한 실정이다.

본 학위논문에서는 분자빔에피택시(molecular beam epitaxy; MBE) 성장법에 반데르발스 물질 핸들링 기법, 투과전자현미경(transmission electron microscopy; TEM) 구조 분석, 나노소자 제작공정을 조합한 새로운 방법론을 제안하여, 고품질 위상절연체 기반의 원자 단위로 제어된 반데르발스 이종구조 제작에 활용하였다. 이러한 접근법을 통해, 위상절연체와 육방정계 질화붕소(hexagonal boron nitride; hBN) 간 고품질 이종에피택시 반데르발스 계면에서 일어나는 수평 및 수직 방향의 전자 수송 특성을 분석하였다.

먼저, 본 논문에서는 MBE법을 이용한 hBN 위의 고품질 위상절연체 Bi_2Se_3 박막 성장과 이의 구조적 및 전기적 특성을 논한다. 특히, 여기서 개발한 MBE 성장기법은 TEM과 호환성을 가지므로, 성장된 필름의 구조적 특성에 대한 빠른 피드백이 용이해진다. 다음으로는 hBN 위에 높은 균일성 및 결정성을 갖는 Bi_2Se_3 박막의 성장법을 제안하였다. 고분해능 TEM 연구를 통해, Bi_2Se_3 와 hBN 사이에 원자 수준으로 깨끗한 계면이 형성되며, 두 물질 간 에피택시 관계가 형성됨을 보였다. 또한, Bi_2Se_3/hBN 이종구조의 전자 수송 특성 분석을 통하여 Bi_2Se_3/hBN 계면에서 높은 전하이동도를 갖는 위상학적 상태가 형성됨을 보였다. 더 나아가, 앞서 제시한 성장 및 특성 분석법이 또다른 위상절연체/반데르발스물질 이종구조 조합에도 다양하게 확대 적용될 수 있음을 설명하였다.

이어지는 연구에서는 TI와 hBN을 이용한 수직 방향 반데르발스 터널 접합의 제작 및 측정을 다룬다. 원자 수준으로 얇은 두께의 hBN을 현수(suspension)시킨 뒤 이 윗면과 아랫면에 위상절연체를 각각 이종에피택시 성장함으로써 TI/hBN/TI 구조를 제조하였다. 또한 이 경우 hBN의 얇은 두께로 인해 계면의 전자 상태에 직접적 전기적 접근이 가능해진다. 본 논문은 두 종류의 TI/hBN/TI 에피택시 이종구조에 대한 터널링 분광법을 실시하여, 터널링 전자의 에너지, 운동량, 스핀 나선성 보존 조건을 분석하였다.

주요어: 분자빔 에피택시, 반데르발스 이종구조, 위상절연체, 질화붕소, 전자 수송 특성, 터널링 분광법

학 번: 2012-20363